SYNTHESIS, CHARACTERIZATION AND DETEMPLATION OF THERMALLY UNSTABLE 3-D METAL-SUBSTITUTED ALUMINOPHOSPHATES

by

Daphne Sigrid Belén-Cordero

A dissertation submitted in partial fulfillment of the requirements for the degree of

DOCTOR of PHILOSOPHY
in
CHEMICAL ENGINEERING
UNIVERSITY OF PUERTO RICO
MAYAGÜEZ CAMPUS
2009

Approved by:

_____	_____
Arturo J. Hernández-Maldonado, PhD President, Graduate Committee	Date
_____	_____
Nelson Cardona Martínez, PhD Member, Graduate Committee	Date
_____	_____
María Martínez Iñesta, PhD Member, Graduate Committee	Date
_____	_____
David Suleiman Rosado, PhD Member, Graduate Committee	Date
_____	_____
David Suleiman Rosado, PhD Chairperson of the Department	Date
_____	_____
Luis Rivera Montalvo, PhD Graduate School Representative	Date

DEDICATED

to my parents Sigrid and José A.
and to my beloved daughter Anjali

PREFACE AND ACKNOWLEDGEMENTS

The work presented in this dissertation is composed of two main parts. The first part encompasses the SBE synthesis procedure and characterization for the Co-, Mg-, and Mn-SBE variants to further understand the detemplation process as well as the optimum conditions for the template removal that were determined via thermal gravimetric (TGA), *in situ* high temperature XRD and simultaneous DSC-XRD. In addition, several spectroscopic techniques (e.g., UV-*vis*, XPS, EPR, NMR) were employed to demonstrate the substitution of the metal ions and to elucidate the coordination nature of the metal atoms incorporated. In order to evaluate the material hydrophilicity, water vapor adsorption on the detemplated Mg-SBE was also investigated. The second part of this dissertation focuses in other approaches to remove the structure-directing agent from the inorganic framework such as ion exchange, solvent extraction, and mild oxidative calcination. Other area under discussion is a preliminary attempt for the growth of CNTs within the SBE framework.

First and foremost I ought to proffer my thanks, obedience and gratitude to our God, for his guidance and help, for all the times that I ask and receive, for all the times that I seek and I find, for all the doors opened. I would like to extend my special thanks to my beloved daughter, Anjali, for her love, for her patience for all the times that she was separated from me, for all the time that I failed to spend with her. I am truly fortunate and indebted to my parents, for their continuous support, special blessings, and all efforts made for taking care of my most precious treasure while I was performing my experiments towards my research work.

I wish to express my deepest respect, profound gratitude, and great appreciation to Dr. Shreekant N. Deshpande (R.I.P.) and Dr. César Reyes for their valuable guidance, inspiration, utmost help, encouragement and advice. I am grateful to my advisor, Dr. Arturo J. Hernández Maldonado, for his guidance, help, continuous support and valuable discussions, which made possible the successful completion of this work. Also, I would like to show gratitude to the members of my graduate committee Dr. Nelson Cardona Matínez, Dr. David Suleiman Rosado and Dr. María Martínez Iñesta. I extend my special thanks to my colleagues in the NSSAL group Milton Rivera and Andrea Cabanzo. Special thanks also to my classmates in the PhD Program Adriana Herrera, Carola Barrera, and Yeira Padilla.

I cannot forget to thank Dr. Juan López-Garriga for his assistance, for providing me with the opportunity of being a Graduate Teaching Fellow in the GUEST K-12 Program, for the experience gained, skills developed towards educational excellence and the responsibilities that it implied. As a member of the Science on Wheels Educational Center (SonWEC) I had the opportunity to exchange knowledge in science and mathematics with K-12 teachers and students, which provided me a mechanism for learning effective teaching. Now, I feel more confident of my presence in the classroom and became more interested in inspiring students' curiosity and their desire for scientific understanding. Programs like these make the difference and are key contributors that can potentially help to assist teachers in the science, mathematics and

technology fields for instilling and motivating their students to become part of the university community and why not, the scientific community.

ABSTRACT

The extent of the detemplation process in Me-SBE (Me = Co^{2+}, Mg^{2+} and Mn^{2+}) aluminophosphates was investigated. Hydrothermal synthesis conditions were optimized to obtain materials with minimal phase impurities. SEM analysis of the Mg- and Mn-SBE as-synthesized samples revealed square-plates with truncated corners morphology, grown in aggregated fashion, and contrasting with the hexagonal-plate like morphology of Co-SBE. Treatment in an oxidative atmosphere and vacuum, respectively, was used to study the removal of the structure-directing agent (SDA; 1,9-diaminononane). Calcination in air or nitrogen results in a *"non-porous"* framework as evidenced by low sorption capacity. Cautious detemplation in vacuum using an evacuation rate of 10 mm Hg/s and a temperature of 648 K resulted in surface areas of ca. 700, 500 and 130 m^2/g for Mg-, Co- and Mn-SBE, respectively. TGA and *in situ* high temperature XRD analyses indicate the frameworks for all the SBE variants experienced collapsing upon treatment in helium at temperatures above 700 K and subsequently formed an aluminophosphate dense phase (i.e., trydimite). *In situ* XRD-DSC data showed that the SBE frameworks experience breathing modes related to specific endothermic and exothermic scenarios during air treatment. Decomposition and elimination of the organic template during vacuum treatments was verified by FT-IR spectroscopy. XPS spectra revealed that most of the Co atoms in vacuum treated samples are in a tetrahedral coordination while the Mn atoms exhibited diverse coordination states and plausible formation of extra-framework species as corroborated by UV-*vis*, EPR, and MAS-NMR spectroscopy. ^{27}Al MAS-NMR spectra for vacuum detemplated Mg-SBE samples prior to and after dehydration confirmed the reversible formation of aluminum octahedral sites. However, this did not affect the porous nature of

detemplated Mg-SBE samples as these are capable of adsorbing 19 water molecules per super cage at 298 K. Detemplation of SBE materials using alternative methods such as ion exchange, solvent extraction, and UV-O_3 treatments were also explored but not accomplished. Attempted carbon nanotubes (CNTs) synthesis by pyrolysis of the organic template within the channels of SBE framework was performed. The process itself appears to be very dependent on the exact experimental conditions and requires further investigation.

Keywords: metal-substituted aluminophosphates (MeAPOs); SBE (UCSB-8); organic templates; structure-directing agents (SDAs); Hoffman degradation/elimination; nanoporous sorbents.

RESUMEN

El proceso remoción de la plantilla orgánica en Me-SBE (Me = Co^{2+}, Mg^{2+} y Mn^{2+}) fue investigada. Además, las condiciones de la síntesis hidrotérmica fueron optimizadas para obtener materiales con un mínimo de impurezas. El análisis de las imágenes del microscopio electrónico de rastreo (SEM) de las muestras de Mg- y Mn-SBE según sintetizada reveló que esos materiales poseen morfología de placas cuadradas con esquinas truncadas que crecen de forma agregada y que está en contraste con la morfología de placas hexagonales observada en Co-SBE. El tratamiento en un ambiente oxidante y en vacío, respectivamente, se utilizó para estudiar la eliminación del agente director de estructura o plantilla orgánica (i.e., 1,9-diaminononano). Tratamientos en aire resultaron en un material no poroso, según lo demuestra la baja capacidad de adsorción. La platilla orgánica fue removida cuidadosamente utilizando tratamientos térmicos en vacío a una razón de evacuación baja (i.e., 10 mm Hg/s) y una temperatura de 648 K. Esto resultó en áreas de superficie de aproximadamente 700, 500 y 130 m^2/g para Mg-, Co- y Mn-SBE, respectivamente. El análisis termogravimétrico (TGA) y de difracción de rayos-X (XRD) *in situ* a altas temperaturas indican que por encima de 700 K todas las variantes de SBE colapsaron durante el tratamiento en helio y posteriormente se formó una fase densa de aluminofosfatos (i.e., tridimita). Datos *in situ* de XRD-DSC demostraron que la estructura de SBE experimenta modos de respiración relacionados con determinados escenarios endotérmicos y exotérmicos durante el tratamiento en aire. La descomposición y posterior eliminación de la plantilla orgánica durante el tratamiento en vacío fueron verificados por espectroscopia de infrarrojo (FT-IR). Los espectros de XPS revelaron que la mayoría de los átomos de cobalto en las muestras tratadas en vacío preservaban la coordinación tetraédrica mientras que los átomos

de Mn presentaban diversos estados de coordinación. Los resultados de espectroscopia UV-*vis*, EPR y NMR corroboran este último resultado. Además, confirman la formación de especies de Mn fuera de la estructura. El espectro de ^{27}Al MAS-NMR de Mg-SBE, antes y después de la deshidratación, confirmó la formación reversible de centros de aluminio con coordinación octaédrica. Sin embargo, esto no afecta a la naturaleza porosa de las muestras de Mg-SBE ya que son capaces de absorber 19 moléculas de agua por caja a 298 K. En general, esto representa el primer paso en el desarrollo de las características únicas que poseen tanto de catalizadores como de adsorbentes en materiales con alta concentración de metales como lo es SBE. Además, métodos alternos a la calcinación a altas temperaturas tales como intercambio iónico, extracción por solvente y tratamientos con luz ultra-violeta (UV) y ozono (O_3) fueron examinados. Aún así, la remoción de la plantilla utilizando cualesquiera de estos métodos no fue alcanzada. Se intentó la síntesis de nanotubos de carbón mediante la pirólisis de la plantilla orgánica dentro de los canales de la estructura de SBE. El proceso aparenta ser bastante dependiente de las condiciones experimentales y requiere investigación adicional.

LIST OF PUBLICATIONS, CONFERENCES AND POSTER SESSIONS

PUBLICATIONS

- Belén-Cordero, D.S; Méndez-González, S.; Hernández-Maldonado, A.J., SBE-Type Cobalt Aluminophosphate Nanoporous Materials: Degradation of the Structure-Directing Agent. *Micropor. Mesopor. Mat.* **2008**, 109(1-3), 287.
- Belén-Cordero, D.S.; Kim, C.; Hwang, S. and Hernández-Maldonado, A.J., SBE-Type Metal-Substituted Aluminophosphates: Detemplation and Coordination Chemistry, *J. Phys.Chem. C (ACS Publications), in press.*

ORAL PRESENTATIONS

- Belén-Cordero, D.S. and Hernández-Maldonado, A.J., "Synthesis and Characterization of SBE-Type Metal Aluminophosphates (Me = Co and Mg)", 2008 Spring ACS National Meeting, New Orleans, LA. (**April 2008**)
- Belén-Cordero, D.S. and Hernández-Maldonado, A.J., "Cobalt Aluminophosphate Nanoporous Sorbents: Hofmann Degradation of the Structure-Directing Agent and Post-Synthesis Treatments", InQu/ACS Advances in Chemical Sciences and Engineering in Puerto Rico, Dorado, PR. (**November 2006**)
- Belén-Cordero, D.S. and Hernández-Maldonado, A.J., "Removal of the Structure-Directing Agent from a Thermally Unstable Metal-Substituted Aluminophosphate", AIChE National Meeting, Cincinnati, OH. (**November 2005**)

POSTER PRESENTATIONS

- Belén-Cordero, D.S. and Hernández-Maldonado, A.J., "SBE Type Cobalt Aluminophosphate Nanoporous Materials", Puerto Rico-EPSCoR Annual Conference, Río Grande, PR. (**May 2007**)
- Belén-Cordero, D.S. and Hernández-Maldonado, A.J., "Cobalt Aluminophosphate Nanoporous Sorbents", NSF GK-12 Annual Meeting, Arlington, VA. (**March 2007**)
- Belén-Cordero, D.S. and Hernández-Maldonado, A.J., "Cobalt Aluminophosphate Nanoporous Sorbents: Hoffman Degradation of the Structure Directing Agent and Post-Synthesis Treatment", PR-LSAMP: 2nd Transdisciplinary Research Conference, Mayagüez, PR. (May 2006)
- Belén-Cordero, D.S. and Hernández-Maldonado, A.J., "Removal of the Organic Template from a Thermally Unstable Metal-Substituted Aluminophosphate Nanoporous Sorbent", 12th ChemE Symposium, Mayagüez, PR. (**October 2005**)
- Belén-Cordero, D.S. and Hernández-Maldonado, A.J., "Removal of the Structure-Directing Agent (SDA) from a Thermally Unstable Cobalt-Substituted Aluminophosphate", PR-LSAMP 1st Transdisciplinary Research Conference, San Juan, PR. (**December 2004**)

TABLE OF CONTENTS

TABLE OF CONTENTS *CONTINUED*

TABLE OF CONTENTS *CONTINUED*

TABLE OF CONTENTS *CONTINUED*

TABLE OF CONTENTS *CONTINUED*

TABLE OF CONTENTS *CONTINUED*

LIST OF FIGURES

Page

LIST OF FIGURES *CONTINUED*

Page

LIST OF FIGURES *CONTINUED*

Page

LIST OF FIGURES *CONTINUED*

Page

LIST OF TABLES

Page

CHAPTER 1

INTRODUCTION TO ZEOLITIC MATERIALS

1.1 History of Zeolites

The history of zeolites began in 1756 when Baron Alex F. Cronstedt, a Swedish mineralogist, heated up a piece of volcanic rock that released large amounts of steam.[1-3] This was the discovery of the first natural zeolite, stilbite (STI). The term *"zeolite"* is derived from the Greek words *zein* (ζειυ) meaning "to boil" and *lithos* (λιθος) meaning "stone".

Zeolites may occur naturally as minerals, but others are synthetic. Natural zeolites can be found all over the world. Around 1940, the synthesis of zeolites began to interest scientists and by 1948, Union Carbide (Figure 1.1) lead the way to the synthetic molecular sieve zeolite business, initiating studies on adsorption for purification, separation and catalysis.[4-7] Since that time, over a hundred types of zeolites have been synthesized and patented.[8]

Figure 1.1. Images of the first articles published by Union Carbide that lead the way to the synthetic molecular sieve zeolite business.[4, 5, 7]

Zeolites are typically synthesized under moderate temperatures and pressures and an alkaline pH to form a complex network of T-bonds that results in a micro-scale pore system. Two types of the synthetic methods commonly used are hydrothermal sol-gel synthesis and high-pressure hydrothermal synthesis. Other methods are confined space, dry-gel, microwave and ultrasonic synthesis.[2]

There are a number of different ways by which zeolites can be modified. Incorporating metal cations other than aluminum and/or silicon to the reaction gel can modify the final framework properties of the zeolite[9, 10] to impart unique properties to the surface. Also, zeolite frameworks can be chemically modified after synthesis to increase the hydrophobic nature of the zeolite (e.g., dealumination, removal of framework aluminum by chemical agents or thermal dehydroxylation).[11]

1.2 Zeolitic Materials and Molecular Sieves

Zeolites are inorganic porous materials with open-framework structures and the interaction of the void surface with guest species makes them suitable for adsorption, catalysis, and transport phenomena processes among others. Szostak[2] describes them as:

> *"a crystalline aluminosilicate with a framework based on a extensive three-dimensional network of oxygen ions. Situated within the tetrahedral sites formed by the oxygen can be either a Si^{4+} or an Al^{3+} ion."*

but the term *"zeolite"* now is generalized and includes most of the types of molecular sieves (Table 1.1). Traditional zeolitic materials comprise centers of silicon, and aluminum within

their framework and cations, water and/or other molecules within their pores and channels.[2, 6] Unit cells of aluminosilicates follow the general formula, $M^{n+}_{x/n}$ $[(AlO_2^-)_x(SiO_2)_y]_zH_2O$, where M^{n+} is the cation, which balances the negative charge brought about by the presence of AlO_2^- (aluminum tetrahedra).[12] The cations, generally alkali or alkaline earth metals (e.g., Na^+, K^+, etc.), are loosely bound to the surface and can be easily exchanged.

Table 1.1. Differences between molecular sieves and zeolites.[2]

Molecular Sieves	**Zeolite**
Porous structure	Microporous crystalline structure
Variable elemental composition	Aluminosilicate framework
Framework cation coordination variable	Tetrahedral coordination
Variable framework charge	Anionic framework

1.3 General Properties and Some Applications of Zeolites

Most commercially available zeolites are exploited based on their properties for adsorption, ion exchange, and/or catalysis applications. The accessibility through the pore system may depend on the size of the guest molecules, known as the molecular sieve effect. Thus, these materials recognize and discriminate molecules with kinetic diameters greater than the pore window diameter, separating and excluding molecules by size and shapes, acting like a strainer.

Zeolites are useful as desiccants due to their capacity to adsorb water that can be removed upon heating. Their use was also explored for quickly clotting severe bleeding under the

brand name *"QuikClot"* or *"Hemosorb"*.[13] In addition, the pore size of zeolites may be varied slightly by ion exchange, making them useful as *"molecular sieves"* due to the positioning of smaller or specific cations in certain positions. It should be mentioned that after metals cations are incorporated into the framework, zeolites could serve as oxidation or reduction catalysts. Moreover, zeolites can also act as shape-selective catalysts due to the size and shape of a particular pore system.

The presence of excess of phosphorous in effluents discharged to natural bodies is known to be responsible for algal bloom and eutrophication of lakes and ponds,[14] interfering with coagulation and contributing to lime soda softening. Because of the harmful effects, effluent discharge standards to natural bodies are continuously upgraded by EPA.[15] Therefore, the removal of phosphorus is necessary, not only to prevent eutrophication but also to maintain the required water quality. Zeolites' largest outlet is in the laundry detergent market replacing harmful phosphate builders from powder detergents, now prohibited in many parts of the world because of water pollution risk. In 1998, the use of synthetic zeolite in detergents worldwide was estimated in 1.04 anhydrous metric tons per year.[16] Unlike phosphates, zeolites will not damage bodies of water.

1.4 Templated Synthesis of Zeolites

Natural zeolites have not gained the commercial importance of synthetic zeolites due to unavailability upon demand, dissimilarity in composition (i.e., purity), crystal and pore

system size (i.e., pore diameter). Hydrothermal synthesis methods have been employed to synthesize numerous materials by using structure directing agents (SDAs) that provide better control of zeolite crystallization. The concentration of transition metal atoms in the frameworks can be dramatically increased and controlled by varying the charge and geometry of structure directing amines as reported by Feng et al.[17] This is the most common method for preparing zeolites in which a viscous aqueous gel consisting of aluminum and other T-atom (i.e., metal atoms occupying tetrahedral positions) sources crystallize at an autogenous pressure at temperatures between 373 K and 523 K.

The zeolites final structure is a product of the synthesis conditions and the post-synthetic treatment. Current methods for zeolite synthesis involve the use of organic molecules as their SDA. Organic SDAs are often added to guide the self-assembly of the zeolite in a desired direction.[18, 19] After the synthesis is completed, a combustion step at high temperatures, and usually in an oxidative environment (i.e., calcination), is required to remove these SDAs from the zeolite framework. Fundamental steps in this process are:[20]

1. Assembly of T-atoms surrounding the SDA molecules with specific interactions that will undergo the zeolite formation conditions.
2. Formation of the zeolite by trapping the SDA inside the framework, which will give the form to the structure (e.g., pores, cavities and channels).
3. Removal of the SDA components or detemplation without destroying the framework and preserving the intrinsic properties.

The removal of the organic moieties after synthesis is essential to release the void space that is necessary for adsorption of guest molecules, allow ion exchange and/or modify the surface while conserving the framework integrity. The charge distribution, size and geometric shape of the organic template is critical for the structure direction.[17] Moreover, one SDA can give rise to several different structures depending on other parameters related to the synthesis such as oxide composition, temperature, time, reagent type and pH.[2, 18] Furthermore, different SDAs can yield the same structure. As an example, SBE could be synthesized using linear alkyldiamines, such as 1,9-diaminononane (DAN) in combination with a co-solvent, or using polyether diamines such as 1,13-diamino-4,7,10-trioxatridecane (TTD).[17, 21]

The role of the SDA molecules during the crystallization is sometimes ambiguous and continues to be a topic of discussion in the literature. As previously mentioned, a zeolite is formed after the metal atoms surround the SDA molecules to start forming the sub-units, which finally determine the pore topology or the given structure. At some instances it stabilizes the zeolite micropores precluding its collapse acting as space fillers. Due to its functionality, amines, which are bases, can be used to enhance the solubility or to increase pH. In the case of SBE-type materials' synthesis,[17, 21] dipropylamine (DPA) is probably used for both, to increase the solubility of 1,9-diaminononane and to reach an alkaline pH.

Valyocsik and Rollmann examined the effect of the size of the SDAs as well as the pH range in the crystallization and related it to the adsorption properties of the final structure.[18] Lok et al. reviewed several zeolite syntheses and studied the role of the organic template in the

synthesis of molecular sieves.[22] Most literature sources indicate that the presence of such species influences the formation of a particular topology. Other authors have performed similar studies confirming the dual role of the SDAs molecules (i.e., space fillers or directing agents).[23-27] When metals are isomorphously substituted within the zeolitic framework (e.g., Mn and Co) in the Al sites, a net negative charge is generated and amine cations are confined to balance the charge of the structure.[26]

1.5 Aluminophosphates

Nowadays, a great effort has been made in the search of new microporous crystalline materials with properties that would impact a diverse range of industries. Among them, members of the aluminophosphates ($AlPO_4$-*n*) family of molecular sieves comprise a great variety of structures. Aluminophosphates are molecular sieves comprising corners sharing AlO_4 and PO_4 tetrahedra.[2, 6, 12] Instead of Si^{4+} ions other element, P^{5+}, is present within the framework. Aluminophosphates commonly have frameworks with only 1-D access to the channel system and due to its nature, the charge of the structure is neutral (i.e., do not have extra-framework metal cations). Before the synthesis of VPI-5, zeolitic materials had pore sizes below 10 Å. In 1987, Davis et al. synthesized the aluminophosphate VPI-5 (Figure 1.2), which is an 18-ring microporous material (pore diameter = 13 Å).[28] This was the first of a series of ultra-large pore zeolite-like materials. Three years later, in 1990, Dessau et al. prepared the first 14-ring zeo-type material, $AlPO_4$-8.[29] The isomorphous substitution of

AlPO-*n* materials with transition metals ions generates negative charge sites, which should be compensated from any positive charge available during synthesis.[9]

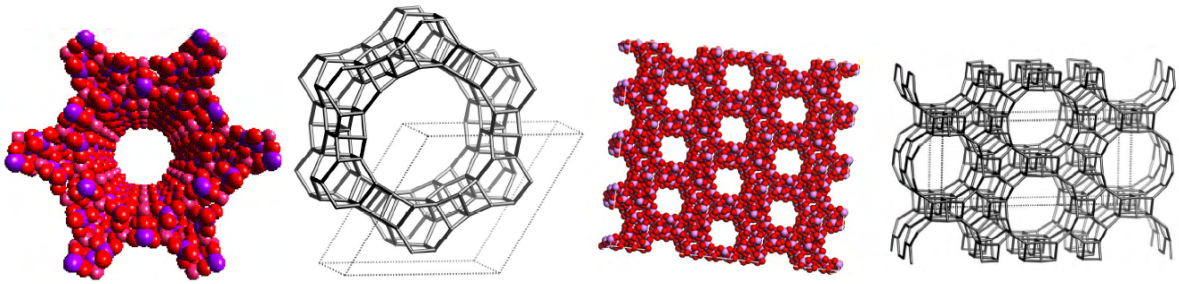

Figure 1.2. Large-pore zeolitic materials: VPI-5 (left) and $AlPO_4$-8 (right).[20, 29]

1.5.1 Synthesis of Aluminophosphates

Aluminophosphates are synthesized hydrothermally at 373–523 K.[30, 31] Their synthesis involves the use of an aqueous mixture containing an aluminum source, a phosphate source and an amine or an ammonium salt (R) acting as the SDA.[2, 12] The aluminum source is generally aluminum isopropoxide or pseudoboehmite, while *o*-phosphoric acid is the most frequently phosphorus source used. Typical reaction gels have molar compositions as $xR:A1_2O_3:(1\pm2)P_2O_5:yH_20$, where R is an amine and/or a quaternary ammonium salt.[30] For the synthesis of silicoaluminophosphates (SAPO), metal aluminophosphates (MeAPO or MAPO) and metal silicoaluminophosphates (MAPSO), a silica source and/or a solution of the metal salt (e.g., an acetate, carbonate or sulphate) are introduced into the reactive mixture. Some aluminophosphates (e.g., chabazite-like (CHA) $AlPO_4$-34) require the presence of fluoride ions in the reaction mixture instead of using organic templates.[32]

1.5.2 Isomorphous Substitution of Aluminophosphates and Cobalt-Substituted Aluminophosphates (CoAPOs)

For its use in applications such as catalysis, zeolites may be modified by incorporating in the framework other metal cation centers rather than aluminum and silicon. Net negative charges are introduced then into the network by isomorphous substitution (defined as *"the replacement of an element in the crystalline framework by another element with similar cation radius and coordination requirements")* of phosphorus and/or aluminum ions in the framework.[6] The isomorphous substitution of AlPO-*n* heteroatoms such as aluminum with divalent metals (e.g., Co) generates net negative charge sites in the framework.[33-35]

Several cobalt-substituted AlPOs[9, 32-53] have been synthesized and characterized, but the chemical coordination nature of the isomorphous substitution of cobalt atoms is certainly not known, although diffuse reflectance UV–*vis* spectroscopy seems to be appropriate to reveal the local geometry of the cobalt sites.[53-55] Spectral changes caused by post-synthesis treatments of CoAPOs, such as the intensity change of the absorption bands characteristic of electronic transition (i.e., $^4A_2 \rightarrow {}^4T_1$) in the blue spectral region, enables estimation of the relative concentration of the tetrahedral cobalt centers.[55] Šponer et al. suggested that the apparent concentration of the divalent centers increases at temperatures above 670 K as well as after the adsorption of water and small amine molecules.[54] It was interpreted in terms of a reduction of the Co(III) centers formed during the course of calcination process. Borges et al. concluded that perhaps the reversible oxidation of most of the framework Co(II) to Co(III) is

responsible for the spectral changes that occurred after calcination and further reduction.[55] Their results also indicate that a small but a significant part of the cobalt suffers irreversible modifications such as the irreversible oxidation and formation of extra-framework cobalt species. Therefore, a change in the oxidation state or coordination of the transition metal maybe the reason why most crystalline structures incorporating cobalt T-atoms collapse after calcination at high temperatures.

1.5.3 Large-Pore Structures and Microporous Materials: SBE-Type Structure

More than a dozen of large-pore zeo-type structures have been synthesized and identified by Stucky and co-workers[17, 21] in three different topologies (i.e., SBS, SBE, SBT). SBE or UCSB-8 has a tetragonal unit cell (Table 1.2). It has an unusual large cage built from 64 T-atoms and connected by an orthogonal channel system with 12-ring and 8-ring apertures, in 2-D and 1-D, respectively. These supercages (Figure 1.3) measure 20 Å by 20 Å by 15 Å, which are quite large when compared to faujasite (FAU) cages that are of spherical type with a 13 Å pore diameter). SBE has the following composition $|(C_9H_{24}N_2^{2+})_{16}|$ $[Al_{32}Co_{32}P_{64}O_{256}]$, where $C_9H_{24}N_2$ (protonated 1,9-diaminononane (DAN)) is the SDA used for its synthesis and is balancing the net negative charge of the framework due to the isomorphous substitution of the metal ion atoms in the aluminum sites.

Table 1.2. Summary of available crystallographic data for SBE.[17, 21]

Name	Structural formula	Space group	a(Å)	b (Å)	c (Å)	R(F)	$2Q_{max}$ (deg)	M-O (Å)
SBE	$Co_xAl_{1-x}PO_4$	*P4/nnc*	19.065	19.065	27.594	9.85	44	1.810

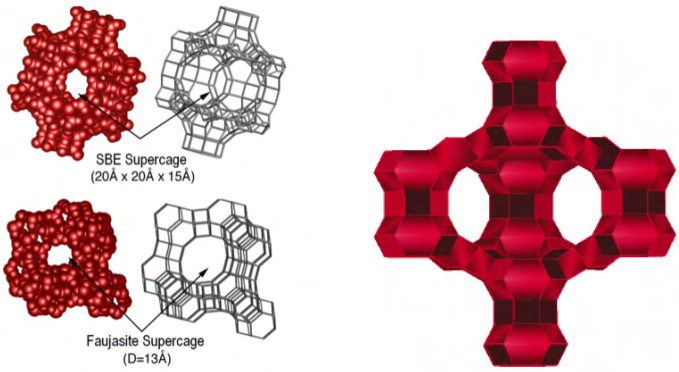

Figure 1.3. SBE supercage and FAU supercage (left). Cross-sectional view of the 64 T-atom cage surrounded by *ocn* cages and double 8-ring units in SBE (right).

1.5.4 Literature Review about SBE Materials

The SBE synthesis procedure was attempted for the first time in 1997 by Bu et al.[17, 21] They revealed the creation of large-pore materials in three different topologies with aluminum (or gallium), cobalt (or manganese, magnesium, or zinc), and phosphorus as the T-atoms. The large cages that builds them are interconnected by a multidimensional 12-ring and makes these types of zeolite structures unique. The main limitation of the Bu et al. synthesis recipe is that it produces multiple phases of large crystals.[21]

In addition, this group has published only two articles on these materials and none of them is related to the removal of the SDA. Feng explored the use of these open framework materials for applications beyond traditional catalytic or adsorptive areas due to the luminescent

phenomenon observed in open-framework oxides.[56] The development of less-expensive and non-toxic luminescent materials for lighting and display technology was suggested as a substitute to replace the use of inorganic phosphors, which usually involves managing metal activators that can be expensive and/or toxic.

Recently, a group from Israel lead by Danielle Golfarb,[57-59] considered these materials only to study the structural features of Mn(II) incorporated into Mn-UCSB-10Mg and Mn-UCSB-6Mg. They combined multifrequency continuous wave electron paramagnetic resonance (CW-EPR) with W-band electron nuclear double resonance (ENDOR) spectroscopy to analyze the properties of the samples.

1.6 Methods for the Removal of the Structure-Directing Agent

When organic templates are used for the synthesis and in order to make the material useful for any application, a traditional calcination process is often used to make the micropores of the zeolite accessible. The following subsections will briefly discuss traditional and non-traditional SDA removal or detemplation strategies.

1.6.1 Traditional Calcination

During the calcination process, samples are subjected to an oxidative atmosphere (i.e., air or oxygen) and temperatures in the range of 723 – 973 K.[60] Sometimes, this process of template decomposition generates cracks within the crystals due to structural stresses that influence the sorbent performance. Studies of zeolite silicalite-1 evidenced that increasing the

heating rate increases the rate of weight loss on template decomposition and had a significant effect in the final properties of the samples.[61] Evidently, materials with large amounts of transition metals are not suitable candidates for oxidative detemplation.

1.6.2 Mild Oxidation of SDA

Novel methods to eliminate the SDAs from materials with poor structural stability have been proposed. One method that is expanding its popularity is the ozone treatment at mild conditions.[62, 63] In 2004, Leung et al. investigated the effectiveness of low-temperature ozone treatment for organic template removal from MFI zeolite membranes.[63] Zeolite membranes and even zeolite single crystals prepared by calcination often suffer from crack formation.[62, 63] Low-temperature detemplation by ozone prevented the formation of defects and cracks after heating treatment and enabled the removal of SDAs from the zeolite at a low temperature. Because ozone is known to decompose rapidly at temperatures higher than 373K, Heng et al. suggested that it was improbable that ozone is the main oxidizer.[63] Hence, they propose that the radical species formed during the thermal decomposition of ozone were responsible for the removal of the organic templates from the zeolite.

Meretei et al. compared template removal agents such as ozone, NO_2 and NO. They showed that ozone was the most active at low temperatures (i.e., 423 K), and the treatment was less destructive than burning off the template in oxygen.[64] The heating treatments with oxidizing NO_2 and NO also resulted in template removal at relatively low temperatures (i.e., 573 – 623

K) with smaller structure deterioration. Low temperature operation, shorter processing time, and cost reduction are some of the advantages of using this treatment in contrast to the traditional calcination method. Other authors have studied the exposure to UV-ozone and determined pore characteristics of mesoporous thin films prior and after the treatments.[65-68] As stated by Clark et al.[65] and Li et al.,[67] this method provided an efficient pathway for the removal of the template at low temperatures conserving the materials' stability and properties while the exposure to the traditional detemplation technique resulted in pitting, roughening, and sometimes the loss of substrate functionality.

Microwave irradiation and two-step calcination methods proposed by He et al., also seems to be more favorable than conventional calcination.[69] Due to its poor stability and easily fragile structures, zeolite β and MCM-41 were taken as examples to illustrate the advantages of these methods. They reported that these alternate methods have beneficial effects on both the structural order and surface acidity. In two-step calcination, materials were first calcined at a low temperature and then calcined at high temperature by using two heating ramps. In the microwave irradiation process, instead of a conventional heat source following initial calcination at low temperature, microwaves were used as the heat source. Their results showed that these methods were beneficial not only to the crystal structure, but also to the surface acidity of zeolite βand that the use of the two-step calcination is superior because it is more suitable and reproducible. Tian et al. proposed the microwave digestion method as an

alternate pathway to remove the organic SDA from siliceous materials and produce inorganic frameworks with higher surface areas and lower structural damages.[70]

1.6.3 Ion-Exchange

Ion exchange is emerging as a new method to remove SDAs from porous materials. Charge, size and hydration energy influence the exchange behavior.[71] Also, the preferred location of the ions in the cages can be determined. It is expected that as ion exchange proceeds, all sites with the protonated amine that is coordinated to the metal atoms will be exchanged. Also, the strongest cation-framework interaction and the affinity sequence for the ions selected can be determined. Concerning the type of ion exchange, single and mixed ion exchange mechanisms can be performed by one simple equilibration in a batch stage using a high solution-volume/zeolite-mass ratio. Ion exchange experiments may be carried out using chloride salts due to their good solubility in aqueous environment. Moreover, chloride is a small anion and may have a low influence in the diffusion process of the in-going cations towards the exchange sites.[72] The removal will occur preferentially depending on the coordination of the protonated SDA. Still there is a great deal of work needed to understand the mechanism involved in exchanging large protonated molecules within zeolite frameworks. In 1998, Natarajan et al. revealed the removal of the SDA from a 3-D open framework tin (II) phosphate by the ion exchange technique that crystal structure collapsed after its removal by calcination in an oxygen atmosphere.[73]

1.6.4 Solvent Extraction

A widely employed method of separation is solvent extraction. In its simplest form, extraction results from the distribution of a component in a miscible solvent. When choosing a solvent system for an extraction, some general principles that should be kept in mind are that the solvents must not react chemically with the components of the mixture, and that the solvent must be readily removed from the mixture following extraction. The solvent extraction technique was patented in 1992 by Whitehurst as a method for recovering organic templates from porous M41S materials.[74] Jones et al. reported the removal of the SDA by solvent extraction at low and high temperatures by using acetic acid as the solvent from silicates (e.g., BEA and MFI topology).[75] They revealed that the removal of the template by extraction was dependent on the size and the interaction of the SDA molecules with the framework. Zhao et al. also removed the template from MCM-41 molecular sieves by solvent extraction using chloric acid in diethyl ether solvent.[76] When the templates were removed by solvent extraction, the observed XRD pattern was similar to the case where the calcination method was used.

Aluminosilicate mesoporous molecular sieves (Al-MMS) prepared at room temperature using hexadecylamine as template were subjected to template extraction prior to calcination.[77] Extraction in ethanol alone removes only that part of the template (i.e., in neutral form), which is not associated with framework Al while the presence of a cation (Na^+ or NH_4^+) ensures total template removal. In this case, the solvent extraction method was coupled with an ion exchange process.

Organic bases that are insoluble in water may be separated by extraction with dilute hydrochloric acid.[78] These bases, like amines, are soluble in acid due to the formation of the amine salt (R–$\mathbf{NH_2}$ + HCl → R–$\mathbf{NH_3Cl}$). After the reaction, the amine may be recovered from the aqueous solution by treatment of the amine salt with a base such as sodium hydroxide (R–$\mathbf{NH_3Cl}$+ NaOH → R–$\mathbf{NH_{2(s)}}$ + $NaCl_{(aq)}$). This is another route that can be used to guide the removal of the organic template by the solvent extraction technique if there were non-protonated amines present. Alcohols, especially sterically hindered ones, do not react under the conditions of amide formation, and they can be used as solvents for amines, which are not soluble in less polar solvents.[79]

Patarin compiled a series of methods for removing organic templates in which the techniques mentioned above were included, along with extraction with supercritical CO_2, ether cleavage by an acid to partly remove the triblock copolymer template (Pluronic P123), and solvent extraction.[80] Accordingly, there are diverse techniques by which the removal of the template can be achieved; especially in cases where the poor stability of the material precludes the use of conventional removal methods.

1.6.5 Cleavage of C-N and C-C bonds

If organic SDAs molecules like amines could react by either pathway such that they undergo reaction mechanisms to cleave C-C or C-N bonds, it would be possible to reduce its kinetic diameter and therefore, accelerate their release during detemplation. This approach will promote the removal of the organic template from the framework without diffusion

problems. Yang et al. developed novel methods to generate materials with two types of pores (i.e., micro- and mesopores) in SBA-15 by using a "step-by-step" template removal using sulfuric acid to decompose the SDA via ether cleavage.[81] Residual template molecules in the walls were totally removed along with the recovery of the micropores by calcination at low temperatures (i.e., 473 K) to prevent the silica matrix from shrinking.

Yang et al. also removed triblock copolymer templates from SBA-15 by means of coupling the process of crystallization and hydrothermal oxidation with H_2O_2.[82] SBA-15 materials exposed to the hydrothermal treatment had higher specific surface areas, in addition to displaying more uniform particle sizes and higher density of silanol groups.

Additionally, boron tribromide (BBr_3) can undergo a series of reactions that can promote the cleavage of C–N bonds for the removal of amino protecting groups. Therefore, it could be used to cleave C–N bonds of amines under mild reaction conditions. Paliakov and Strekowski reported that the treatment of benzylamino substituted quinolines with BBr_3 (Figure 1.4) yielded the corresponding amino or hydroxyl substituted derivative in high yield by selective demethylation, using short reaction times.[83]

Chandrasekhar et al. stated that selective cleavage of C–C bonds can be accomplished by using polymethylhydroxyloxane(PHMS)-$ZnCl_2$/$Pd(PPh_3)_4$ (Figure 1.5).[84] In this study, a few allyl amines were exposed to (PHMS), $ZnCl_2$ and $Pd(PPh_3)_4$ to yield the corresponding amines by the cleavage of the allyl group.

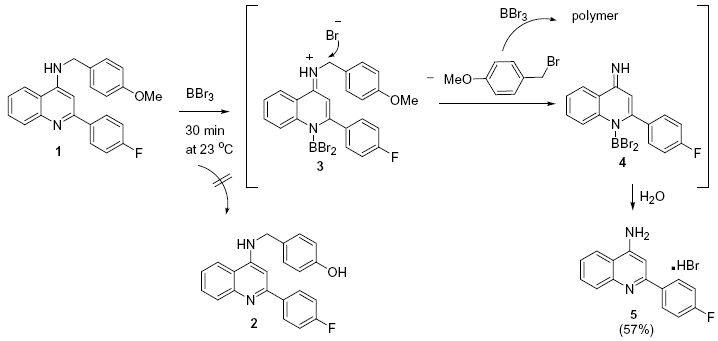

Figure 1.4. Scheme of the reaction pathway of the attempted removal of a methyl group from N-methoxybenzyl substituted quinolin-4-amine(**1**).[83]

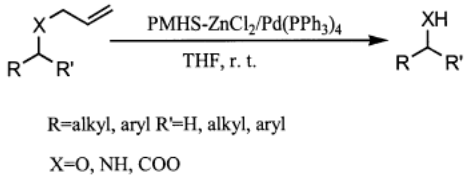

R=alkyl, aryl R'=H, alkyl, aryl

X=O, NH, COO

Figure 1.5. Scheme of the reaction pathway for the allyl deprotection of amines by cleavage of C-C bonds.[84]

1.7 Molecular Modeling: Interaction of the SDA in SBE Frameworks

Computer simulation techniques involve ways to make easier and feasible modeling studies to mimic the behavior of real molecular systems.[85] Molecular modeling relies on quantum mechanics and the use of parameterized analytical expressions through either experimental observation or quantum calculations, to evaluate the interaction energies for a given structure or configuration. A variety of modeling scenarios are used to estimate the potential energy forces on the atoms to obtain optimized configurations for molecules and/or periodic systems such as polymers and zeolites.

Many computational methods have been used to model the interaction of the SDA molecules with zeolite frameworks in an effort to investigate the role of the organic moieties, its location, preferred conformation (i.e., coordination) and ability to direct the synthesis.[27, 86-88] The ability to determine the role of the template in the zeolite synthesis is fundamental for the development of novel materials. Moreover, electrostatic interactions of the organic template with the framework and the dependence in the geometry and chain length have a remarkable effect in the final topology adopted by the material during the synthesis.[27, 89] The characterization of the materials in combination with computer simulation would strongly help to elucidate how the template molecules act, evaluate the potential properties of the systems and allow comparison of estimated values with experimental data. This is a key step to predict and anticipate the behavior of zeolitic systems.

1.8 Motivation

During the last decades large-pore volume molecular sieves have become interesting from the catalytic[89] point of view because of their *"molecular sieve effect"* and their use as shape selective catalysts. The petroleum industry uses them to increase the octane rating of gasoline, a mixture that contains molecules of various sizes.[90, 91] For pharmaceutical and agrochemical industries, chiral purity is of crucial importance due to the vast different biological activity of the enantiomers produced.[92] The process of generating pure enantiomers from racemates would involve either physical separation of a racemic mixture or the use of homogenous chiral catalysts. An ideal catalyst must generate heterogeneity but preserve stereospecificity due to the large amounts of reactants (i.e., racemic mixture) that

are discarded by the use of the physical separation methods. Using a homogeneous catalyst implies that the products, reactants and the catalyst are all in the same phase, which gives rise to separation problems and catalyst recovery.

Incorporation of metal ions into aluminophosphate (AlPO-*n*) molecular sieves frameworks provides specific properties that could produce potential materials candidates for both catalytic and adsorption applications.[9, 10] Metal aluminophosphates (MeAPOs) are of particular interest for the design of new materials functional for a series of heterogeneously catalyzed reactions in environmental catalysis[9, 37, 38] such as oxidation of NO_x and CO, and acid-catalyzed reactions such as methanol-to-olefins.[93]

During the late 1990s, Stucky and co-workers reported the synthesis of more than a dozen porous zeo-type structures with large cages and a Me/Al ratio close to unity.[17, 21] The SBE topology, which has an unusually large cage and a typical unit cell composition of $|(C_9H_{24}N_2{}^{2+})_{16}|\ [Al_{32}Me_{32}P_{64}O_{256}]$, has a low thermal stability due to the high concentration of metal ions and the SDA used for its synthesis, 1,9-diaminononane, is known to be balancing the net negative charge of the framework that resulted from the isomorphous substitution. Bu et al. reported that the specific template-framework species interaction is between a primary ammonium cation and an oxygen anion coordinated to tetrahedrally coordinated atoms.[17] Metals incorporated in the sites of the Al^{3+} of SBE include Co^{2+}, Mg^{2+} and Mn^{2+}.

Although SBE-type materials promise unique properties (Table 1.3) for adsorption and catalysis applications, the potential could only be achieved after removal of the SDA while preserving the framework integrity. In other words, maintaining the material microporosity via detemplation.

Table 1.3. Comparison between properties of SBE and FAU materials.

	SBE*	**FAU**
Pore Diameter (nm)	**12** 0.72 x 0.74 **8** 0.4 x 0.4	0.74
Pore Volume (cm^3/g)	0.34	0.34[94]
Surface Area (m^2/g)	1233	898[95]
Volume of Cage ($Å^3$)	3141.59	1150.35[8]
Unit Cell Volume ($Å^3$)	9320.78	14428.77[8]

Conventional methods for removing organic templates from molecular sieves involve the use of air at high temperatures to break down and desorb the template via Hoffman elimination and the spontaneous ionization through the formation of Brønsted acid sites.[96, 97] Preliminary tests done to remove the SDA from SBE frameworks via calcination process damaged the framework and the structure collapse as evidenced by X-Ray Diffraction (XRD) patterns and a low sorption capacity. The crystalline structure of SBE collapsed after calcination above 673 K (i.e., irreversible modifications of the metal center in the framework and the irreversible oxidation and formation of extra-framework species) as a consequence of a change in its coordination.

*Estimated the mathematic approach using surface area and volume of an ellipsoid and crystallographic data.

However, access to these SBE outstanding properties requires the complete or partial removal of the SDA using techniques capable of overcoming the structure's low stability due to the metal-coordination chemistry or metastability. The detemplation process and coordination chemistry of the organic template in SBE materials requires without doubt more study and is the focus of this dissertation.

1.9 Objectives

1.9.1 General Objective

The principal aim of this work is the removal of the SDA from a thermally unstable metal-aluminophosphates (i.e., SBE-type structures) to be used in the future as nanoporous sorbents for diverse applications such as environmental catalysis, desulfurization processes, or as templates for the growth of other nanostructures.

1.9.2 Specific Objectives

- In house synthesis of **single-phase powder** crystals of SBE type frameworks via hydrothermal paths.
    - Templating via organic structure directing agents (SDAs) using a linear alkyldiamine (i.e., 1,9-diaminononane) as the organic template.
    - Isomorphous substitution of cobalt, magnesium or manganese.
- Characterization of the materials:

- X-Ray Diffraction (XRD) was used to verify the purity of the SBE phase, Scanning Electron Microscopy (SEM) to elucidate the morphology of SBE crystals, Energy Dispersive X-Ray analysis (EDX) to determine the composition of SBE and Transmission Electron Microscopy (TEM) to investigate the porous structure of Mn-SBE frameworks.
- Porosimetry tests were performed to determine the surface area and pore size, FT-IR spectroscopy to test for the presence or absence of organic moieties within the SBE framework, *in situ* high temperature XRD and X-Ray diffraction-Differential Scanning Calorimetry (XRD-DSC) analyses to investigate the thermal stability of the materials.
- Thermal gravimetric (TG) analyses were used to study the thermal stability of the material and the structure-directing agent (SDA) desorption or elimination process.
- Elucidate of chemical environment or coordination chemistry of the metal atoms X-ray Photoelectron (XPS), UV-*vis*, Electron Paramagnetic Resonance (EPR) and Solid-State Magic Angle Spinning-Nuclear Magnetic Resonance (MAS-NMR) spectroscopic methods were employed.

- Use of non-traditional methods for the removal of the structure-directing agent such as solvent extraction, ion exchange, coupled solvent extraction and ion exchange, mild oxidative calcination, non-thermal calcination.
- Model interactions between the template and the framework.

- Study the effect of post-synthesis treatments for the removal of the SDA and pH in the properties of SBE-type materials (e.g., surface area, crystallinity, etc.).
- Correlate and analyze the synthesis and post-synthesis modification variables/conditions to fully understand the materials' final adsorption properties.

LITERATURE CITED

[1] Davis, M. E.; Lobo, R. F. Zeolite and Molecular Sieve Synthesis. *Chem. Mater.* **1992**, *4*(4), 756-768.

[2] Szostak, R. *Molecular Sieves: Principles of Synthesis and Identification*. Blackie Academic and Professional, Thomson Science: New York, 1998.

[3] Moore, J. H.; Spencer, N. D., Zeolites. In *Encyclopedia of Chemical Physics and Physical Chemistry*, Moore, J. H.; Spencer, N. D., Eds. Institute of Physics 2001; Vol. 1-3, p 2814.

[4] Milton, R. M.; Breck, D. W. Crystalline Zeolites. I. The Properties of a New Synthetic Zeolite, Type A. *J. Am. Chem. Soc.* **1956**, *78*, 5963-5972.

[5] Reed, T. B.; Breck, D. W. Crystalline Zeolites. II. Crystal Structure of Synthetic Zeolite, Type A. *J. Am. Chem. Soc.* **1956**, *78*, 5972-5977.

[6] Breck, D. W. *Zeolite Molecular Sieves*. Wiley: New York, 1973.

[7] Milton, R. M. Molecular Sieves Adsorbents. 2,882,243 1959.

[8] Baerlocher, C.; McCusker, L. B., Database of Zeolite Structures. In International Zeolite Association Synthesis Commission: 2007.

[9] Hartmann, M.; Kevan, L. Transition-Metal Ions in Aluminophosphate and Silicoaluminophosphate Molecular Sieves: Location, Interaction with Adsorbates and Catalytic Properties. *Chem. Rev.* **1999**, *99*(3), 635-663.

[10] Weckhuysen, B. M.; Rao, R. R.; Martens, J. A.; Schoonheydt, R. A. Transition Metal Ions in Microporous Crystalline Aluminophosphates: Isomorphous Substitution. *Eur. J. Inorg. Chem.* **1999**, *1999*(4), 565-577.

[11] Beyer, H. K., Dealumination Techniques for Zeolites. In *Molecular Sieves - Science and Technology*, Springer Berlin / Heidelberg: 2001; Vol. 3, pp 204-255.

[12] Szostak, R., Synthesis of Molecular Sieve Phosphates In *Molecular Sieves - Science and Technology*, Springer Berlin / Heidelberg: 1998; Vol. 1, pp 157-185.

[13] Alam, H. B.; Chen, Z.; Jaskille, A.; Ireneo, R.; Querol, L. C.; Koustova, E.; Inocencio, R.; Conran, R.; Seufert, A.; Ariaban, N.; Toruno, K.; Rhee, P. Application of a Zeolite Hemostatic Agent Achieves 100% Survival in a Lethal Model of Complex Groin Injury in Swine. *J. Traum.* **2004**, *56*, 974-983.

[14] Roy, P. K. Nanofiltration as a Tertiary Treatment for Phosphate Removal from Water. Asian Institute of Technology, Bangkok, Thailand, 1995.

[15] Johnson, M. T.; Marcus, B. *Competitive Implications of the Environment Regulation: In the Laundry Detergent Industry*; USA Environmental Protection Agency: June 1996, 1996; p 23.

[16] Litke, D. W. *Review of Phosphorus Control Measures in the United States and Their Effects on Water Quality*; US Geological Survey: 1999.

[17] Bu, X. H.; Feng, P. Y.; Stucky, G. D. Large-Cage Zeolite Structures with Multidimensional 12-Ring Channels. *Science* **1997**, *278*(5346), 2080-2085.

[18] Valyocsik, E. W.; Rollmann, L. D. Diamines as Templates in Zeolite Crystallization. *Zeolites* **1985**, *5*, 123-125.

[19] De Bord, J.; Haushalter, R. D.; Robert, C.; Zubieta, J. The First Organically Templated Layered Cobalt Phosphates: Hydrothermal Syntheses and Crystal Structures of $[H_3N(CH_2)_3NH_3]_{0.5}[Co(PO_4)]\cdot H_2O$ and $[H_3N(CH_2)_4NH_3]_{0.5}[Co(PO_4)]$. *J. Solid State Chem.* **1996**, *125*, 270-273.

[20] Davis, M. E.; Saldarriaga, C.; Montes, C.; Garces, J.; Crowder, C. A Molecular-Sieve with 18-Membered Rings. *Nature* **1988**, *331*(6158), 698-699.

[21] Feng, P. Y. Synthesis and Characterization of Transition Metal Phosphate-Based Novel Framework Materials. Doctoral Dissertation, University of California, Santa Barbara, 1998.

[22] Lok, B. M.; Cannan, T. R.; Messina, C. A. The Role of Organic Molecules in Molecular Sieve Synthesis. *Zeolites* **1983**, *3*, 282-291.

[23] Rollmann, L. D.; Schlenker, J. L.; Lawton, S. L.; Kennedy, C. L.; Kennedy, G. J.; Doren, D. J. On the Role of Small Amines in Zeolite Synthesis. *J. Phys. Chem. B* **1999**, *103*, 7175-7183.

[24] Rollmann, L. D.; Schlenker, J. L.; Kennedy, C. L.; Kennedy, G. J.; Doren, D. J. On the Role of Small Amines in Zeolite Synthesis. 2. *J. Phys. Chem. B* **2000**, *104*, 721-726.

[25] Vaidhyanathan, R.; Natarajan, S.; Rao, C. N. R. Unusual Dual Role of the Organic Amine in an Open-Framework Structure. *J. Mater. Chem.* **1999**, *9*, 2789-2793.

[26] Mali, G.; Meden, A.; Ristić, A.; Tušar, N. N.; Kaučič, V. Interaction of Dipropylamine Template Molecules with the Framework of As-Synthesized $AlPO_4$-31. *J. Phys. Chem. B* **2002**, *106*(1), 63-69.

[27] Sastre, G.; Leiva, S.; Sabater, M. J.; Gimenez, I.; Rey, F.; Susana Valencia; Corma, A. Computational and Experimental Approach to the Role of Structure-Directing Agents in the Synthesis of Zeolites: The Case of Cyclohexyl Alkyl Pyrrolidinium Salts in the Synthesis of ß, EU-1, ZSM-11, and ZSM-12 Zeolites. *J. Phys. Chem. B* **2003**, *107*, 5432-5440.

[28] Davis, M. E.; Montes, C.; Hathaway, P. E.; Arhancet, J. P.; Hasha, D. L.; Garces, J. M. Physicochemical Properties of VPI-5. *J. Am. Chem. Soc.* **1989**, *111*(11), 3919-3924.

[29] Dessau, R. M.; Schlenker, J. L.; Higgins, J. B. Framework Topology of $AlPO_4$-8: The 1st 14-Ring Molecular-Sieve. *Zeolites* **1990**, *10*(6), 522-524.

[30] Wilson, S. T.; Lok, B. M.; Messina, C. A.; Cannan, T. R.; Flanigen, E. M. Aluminophosphate Molecular Sieves: A New Class of Microporous Crystalline Inorganic Solids. *J. Am. Chem. Soc.* **1982**, *104*, 1146-1147.

[31] Wilson, S. T.; Lok, B. M.; Flanigen, E. M. Crystalline Metallophosphate Compositions. 4,310,440, 1982.

[32] Tuel, A.; Caldarelli, S.; Meden, A.; McCusker, L. B.; Baerlocher, C.; Ristić, A.; Rajić, N.; Mali, G.; Kaučič, V. NMR Characterization and Rietveld Refinement of the Structure of Rehydrated $AlPO_4$-34. *J. Phys. Chem. B* **2000**, *104*, 5697-5705.

[33] Canesson, L.; Tuel, A. Synthesis and Characterization of CoAPO(4)-39 Molecular Sieves. *Zeolites* **1997**, *18*(4), 260-268.

[34] Chen, J. S.; Sankar, G.; Thomas, J. M.; Xu, R. R.; Greaves, G. N.; Waller, D. Cobalt-Substituted Aluminophosphate Molecular-Sieves - X-Ray Absorption, Infrared Spectroscopic, and Catalytic Studies. *Chem. Mater.* **1992**, *4*(6), 1373-1379.

[35] Thomas, J. M.; Greaves, G. N.; Sankar, G.; Wright, P. A.; Chen, J. S.; Dent, A. J.; Marchese, L. On the Nature of the Active-Site in a CoAPO-18 Solid Acid Catalyst. *Angew. Chem. Int. Edit.* **1994**, *33*(18), 1871-1873.

[36] Silva, A. O. S.; Souza, M. J. B.; Araujo, A. S. Hydrothermal Synthesis and Thermal Characterization of Niobium-Aluminophosphate with AEL Structure. *Int. J. Inorg. Mater.* **2001**, *3*(6), 461-466.

[37] Pastore, H. O.; Coluccia, S.; Marchese, L. Porous Aluminophosphates: From Molecular Sieves to Designed Acid Catalysts. *Annu. Rev. Mater. Res.* **2005**, *35*, 351-395.

[38] Gorte, R. J. What Do We Know About the Acidity of Solid Acids? *Catal. Lett.* **1999**, *62*(1), 1-13.

[39] Fan, W. B.; Schoonheydt, R. A.; Weckhuysen, B. M. Synthesis of Co-Rich CoAPO-CHA Molecular Sieves in the Presence of Ethanol and Cesium. *Chem. Commun.* **2000**, (22), 2249-2250.

[40] Fan, W. B.; Li, R. F.; Dou, T.; Tatsumi, T.; Weckhuysen, B. M. Solvent Effects in the Synthesis of CoAPO-5, -11 and -34 Molecular Sieves. *Micropor. Mesopor. Mater.* **2005**, *84*(1-3), 116-126.

[41] Batista, J.; Kaučič, V.; Rajić, N.; Stojakovic, D. On the Formation of CoAPSO-44. *Zeolites* **1992**, *12*(8), 925-928.

[42] Hill, S. J.; Williams, C. D.; Duke, C. V. A. The Synthesis of High Cobalt-Containing CoAPO-34. *Zeolites* **1996**, *17*(3), 291-296.

[43] Duke, C. V. A.; Hill, S. J.; Williams, C. D. Synthesis of MnAPO-20 and CoAPO-20 Using Tetrahedral Metal Species. *J. Chem. Soc., Chem. Commun.* **1994**, (22), 2633-2633.

[44] Singh, P. S.; Shaikh, R. A.; Bandyopadhyay, R.; Rao, B. S. Synthesis of CoVPI-5 with Bifunctional Catalytic Activity. *J. Chem. Soc., Chem. Commun.* **1995**, (22), 2255-2256.

[45] Ahn, S.; Chon, H. The Influence of Metal Ions on the Synthesis of MeAPO-5 (Me = Co, Mg) in the Presence of Acetate Ions. *Micropor. Mater.* **1997**, *8*(3-4), 113-121.

[46] Meusinger, J.; Vinek, H.; Lercher, J. A. Cracking of N-Hexane and N-Butane over SAPO-5, MgAPO-5 and CoAPO-5. *J. Mol. Catal.* **1994**, *87*(2-3), 263-274.

[47] Marchese, L.; Chen, J. S.; Thomas, J. M.; Coluccia, S.; Zecchina, A. Bronsted, Lewis, and Redox Centers on CoAPO-18 Catalysts: 1. Vibrational-Modes of Adsorbed Water. *J. Phys. Chem.* **1994**, *98*(50), 13350-13356.

[48] Montes, C.; Davis, M. E.; Murray, B.; Narayana, M. Isolated Redox Centers within Microporous Environments: 1. Cobalt-Containing Aluminophosphate Molecular-Sieve 5. *J. Phys. Chem.* **1990**, *94*(16), 6425-6430.

[49] Prakash, A. M.; Hartmann, M.; Kevan, L. Synthesis, Characterization, and Adsorbate Interactions of CoAPO-41 and CoAPSO-41 Molecular Sieves. *J. Phys. Chem. B* **1997**, *101*(35), 6819-6826.

[50] Zhang, G. A.; Harris, T. V. X-Ray Absorption Studies of Cobalt Aluminophosphate Zeolites (CoAPO-5). *Physica B* **1995**, *209*(1-4), 697-698.

[51] Akolekar, D. Investigations on the CoAPO-36 Molecular-Sieve. *Catal. Lett.* **1994**, *28*(2-4), 249-262.

[52] Salem, A. S. H. Naphtha Desulfurization by Adsorption. *Ind. Eng. Chem. Res.* **1944**, *33*, 336-340.

[53] Wood, D. L.; Remeika, J. P. Optical Adsorption of Tetrahedra: Co^{3+} and Co^{2+} in Garnets. *J. Chem. Phys.* **1967**, *46*(9), 3595-3602.

[54] Spǒner, J.; Čejka, J.; Dědeček, J.; Wichterlová, B. Coordination and Properties of Cobalt in the Molecular Sieves CoAPO-5 and-11. *Micropor. Mesopor. Mater.* **2000**, *37*(1-2), 117-127.

[55] Borges, C.; Ribeiro, M. F.; Henriques, C.; Lourenço, J. P.; Murphy, D. M.; Louati, A.; Gabelica, Z. Structural State and Redox Behavior of Framework Co(II) in CoIST-2: A Novel Cobalt-Substituted Aluminophosphate with AEN Topology. *J. Phys. Chem. B* **2004**, *108*(24), 8344-8354.

[56] Feng, P. Y. Photoluminescence of Open-Framework Phosphates and Germanates. *Chem. Commun.* **2001**, (17), 1668-1669.

[57] Arieli, D.; Delabie, A.; Vaughan, D. E. W.; Strohmaier, K. G.; Goldfarb, D. Isomorphous Substitution of Mn(II) into Aluminophosphate Zeotypes: A Combined High-Field ENDOR and DFT Study. *J. Phys. Chem. B* **2002**, *106*, 7509-7519.

[58] Arieli, D.; Prisner, T. F.; Hertel, M.; Goldfarb, D. Resolving Mn Framework Sites in Large Cage Aluminophosphate Zeotypes by High Field EPR and ENDOR Spectroscopy. *Phys. Chem. Chem. Phys.* **2004**, *6*(1), 172-181.

[59] Goldfarb, D. High Field ENDOR as a Characterization Tool for Functional Sites in Microporous Materials. *Phys. Chem. Chem. Phys.* **2006**, *8*, 2325-2343.

[60] Zholobenko, V.; Garforth, A.; Dwyer, J. TGA-DTA Study on Calcination of Zeolitic Catalysts. *Thermochim. Acta* **1997**, *294*, 39-44.

[61] Gualtieri, M. L.; Gualtieri, A. F.; Hedlund, J. The Influence of Heating Rate on Template Removal in Silicalite-1: An In Situ HT-XRPD Study. *Micropor. Mesopor. Mater.* **2006**, *89*(1-3), 1-8.

[62] Heng, S.; Pui Sze Lau, P.; Yeung, K. L.; Djafer, M.; Schrotter, J. C. Low-Temperature Ozone Treatment for Organic Template Removal from Zeolite Membrane. *J. Membrane Sci.* **2004**, *243* 69-78.

[63] Leung, Y. L. A.; Yeung, K. L. Microfabricated ZSM-5 Zeolite Micromembranes. *Chem. Eng. Sci.* **2004**, *59*, 4809-4817.

[64] Meretei, E.; Halász, J.; Méhn, D.; Kónya, Z.; Korányi, T. I.; Nagy, J. B.; Kiricsi, I. Structural Consequences of Mild Oxidative Template Removal in the Synthesis of Modified MCM-41 Silicates. *J. Mol. Struct.* **2003**, *651-653*, 323-330.

[65] Clark, T.; Ruiz, J. D.; Fan, H.; Brinker, C. J.; Swanson, B. I.; Parikh, A. N. A New Application of UV-Ozone Treatment in the Preparation of Substrate-Supported Mesoporous Thin Films. *Chem. Mater.* **2000**, *12*, 3879-3884.

[66] Parikh, A. N.; Navrotsky, A.; Li, Q.; Yee, C. K.; Amweg, M. L.; Corma, A. Non-Thermal Calcination by Ultraviolet Irradiation in the Synthesis of Microporous Materials. *Micropor. Mesopor. Mater.* **2004**, *76*, 17-22.

[67] Li, Q.; Amweg, M. L.; Yee, C. K.; Navrotsky, A.; Parikh, A. N. Photochemical Template Removal and Spatial Patterning of Zeolite MFI Thin Films Using UV/Ozone Treatment. *Micropor. Mesopor. Mater.* **2005**, *87*, 45-51.

[68] Navrotsky, A.; Parikh, A. N. Methods for Removing Organic Compounds from Nano-Composite Materials. US6,960,327 B2, November 1,2005, 2005.

[69] He, J.; Yang, X.; Evans, D. G.; Duan, X. New Methods to Remove Organic Templates from Porous Materials. *Mater. Chem. Phys.* **2002**, *77*, 270-275.

[70] Tian, B.; Liu, X.; Yu, C.; Gao, F.; Luo, Q.; Xie, S.; Tu, B.; Zhao, D. Microwave Assisted Template Removal of Siliceous Porous Materials. *Chem. Commun.* **2002**, 1186-1187.

[71] Palmer, J. L.; Gunter, M. E. The Effects of Time, Temperature, and Concentration on Sr^{2+} Exchange in Clinoptilolite in Aqueous Solutions. *Am. Mineral.* **2001**, *86*, 431-437.

[72] Barros, M. A. S. D.; Arroyo, P. A. Thermodynamics of the Exchange Processes between K^{+}, Ca^{2+} and Cr^{3+} in Zeolite NaA. *Adsorption* **2004**, *10*, 227-235.

[73] Natarajan, S.; Eswaramoorthy, M.; Cheetham, A. K.; Rao, C. N. R. A Three-Dimensional Open-Framework Tin(II) Phosphate Exhibiting Reversible dehydration and ion-exchange properties. *Chem. Commun.* **1998**, 1561-1562.

[74] Whitehurst, D. D. Methods to Recover Organic Templates From Freshly Synthesized Molecular Sieves. 5,143,879, 1992.

[75] Jones, C. W.; Tsuji, K.; Takewaki, T.; Beck, L. W.; Davis, M. E. Tailoring Molecular Sieves Properties During SDA Removal Via Solvent Extraction. *Micropor. Mesopor. Mater.* **2001**, *48*, 57-64.

[76] Zhao, X. S.; Lu, G. Q. Modification of MCM-41 by Surface Silylation with Trimethylchlorosilane and Adsorption Study. *J. Phys. Chem. B* **1998**, *102*, 1556-1561.

[77] Mokaya, R.; Jones, C. W. The Influence of Template Extraction on the Properties of Primary Amine Templated Aluminosilicate Mesoporous Molecular Sieves. *J. Mater. Chem.* **1998**, *8*, 2819-2826.

[78] Wade, L. G. *Organic Chemistry*. 5th ed.; Prentice Hall: Walla Walla, WA, 2002; p 1296.

[79] Kazmaier, U. A Short Synthesis of Conjugated Unsaturated Amides and Esters Via Triphenylphosphine-Catalysed Isomerisation of Acetylenic Pentafluorophenyl Esters. *Chem. Commun.* **1997**, (23), 2305-2306.

[80] Patarin, J. Mild Methods for Removing Organic Templates from Inorganic Host Materials. *Angew. Chem. Int. Edit.* **2004**, *43*, 3878-3880.

[81] Yang, C. M.; Zibrowius, B.; Schmidt, W.; Schüth, F. Stepwise Removal of the Copolymer Template from Mesopores and Micropores in SBA-15. *Chem. Mater.* **2004**, *16*(15), 2918-2925.

[82] Yang, L. M.; Wang, Y. J.; Luo, G. S.; Dai, Y. Y. Simultaneous Removal of Copolymer Template from SBA-15 in the Crystallization Process. *Micropor. Mesopor. Mater.* **2005**, *81*(1-3), 107- 114.

[83] Paliakov, E.; Strekowski, L. Boron Tribromide Mediated Debenzylation of Benzylamino and Benzyloxy Groups. *Tetrahedron Lett.* **2004**, *45*, 4093-4095.

[84] Chandrasekhar, S.; Reddy, C. R.; Rao, J. Facile and Selective Cleavage of Allyl Ethers, Amines, and Esters Using Polymethylhydrosiloxane - $ZnCl_2$/$Pd(PPh_3)_4$. *Tetrahedron Lett.* **2001**, *57*, 3435-3438.

[85] Leach, A. R. *Molecular Modeling: Principles and Applications*. 2nd ed.; Pearson Prentice Hall: England, 2001; p 768.

[86] Gomez-Hortiguela, L.; Cora, F.; Catlow, R. A.; Perez-Pariente, J. Computational Study of the Structure Directing Effect of Benzylpyrrolidine and its Fluorinated Derivatives in the Synthesis of the Aluminophosphate AlPO-5. *J. Am. Chem. Soc.* **2004**, *126*, 12097-12102.

[87] Cox, P.; Casci, J. L.; Stevens, A. P. Molecular Modeling of Templated Zeolite Synthesis. *Faraday Disscuss.* **1997**, *106*, 473-487.

[88] de Vos Burchart, E.; van Koningsveld, H.; van de Graaf, B. Molecular Mechanics Studies of TBA and TPA in MEL and MFI. *Micropor. Mater.* **1997**, *8*, 215-222.

[89] Sun, P.; Jin, Q.; Wang, L.; Li, B.; Ding, D. A Study of the Templating Ability of Diquaternary Cations for the Zeolite Synthesis in Terms of Energetics. *J. Porous Mat.* **2003**, *10*, 145-150.

[90] Corma, A.; Díaz-Cabañas, M. J.; Martínez-Triguero, J.; Rey, F.; Rius, J. A Large-Cavity Zeolite with Wide Pore Windows and Potential as an Oil Refining Catalyst. *Nature* **2002**, *418*, 514-517.

[91] Quann, R. J.; Green, L. A.; Tabak, S. A.; Krambeck, F. J. Chemistry of Olefin Oligomerization over ZSM-5 Catalyst *Ind. Eng. Chem. Res.* **1988**, *27*, 565-570.

[92] Feast, S.; Bethell, D.; Bulman Page, P. C.; King, F.; Rochester, C. H.; Siddiqui, M. R. H.; Willock, D. J.; Hutchings, G. J. In *Heterogeneous Enantioselective Dehydration of Butan-2-ol*, Stud. Surf. Sci. Catal., 1996; Elsevier: 1996; pp 211-219.

[93] Chen, J.; Thomas, J. M. MAPO-18 (M=Mg, Zn, Co): A New Family of Catalysts for the Conversion of Methanol to Light Olefins. *J. Chem. Soc., Chem. Commun.* **1994** (5), 603-604.

[94] Kumar, R.; Cheng, W. C.; Rajagopalan, K.; Peters, A. W.; Basu, P. The Effect of Exchange Cations on Acidity, Activity, and Selectivity of Faujasite Cracking Catalysts. *J. Catal.* **1993**, *143*(2), 594-600.

[95] Dybowski, C.; Bansal, N.; Duncan, T. M. NMR Spectroscopy of Xenon in Confined Spaces: Clathrates, Intercalates, and Zeolites. *Annu. Rev. Phys. Chem.* **1991**, *42*, 433-464.

[96] Gorte, R. J.; White, D. Interactions of Chemical Species with Acid Sites in Zeolites. *Top. Catal.* **1997**, *4*(1-2), 57-69.

[97] Moissette, A.; Marquis, S.; Gener, I.; Bremard, C. Sorption of Anthracene, Phenanthrene and 9,10-Dimethylanthracene on Activated Acid HZSM-5 Zeolite:

Effect of Sorbate Size on Spontaneous Ionization Yield. *Phys. Chem. Chem. Phys.* **2002**, *4*(22), 5690-5696.

CHAPTER 2

SBE-TYPE COBALT ALUMINOPHOSPHATES NANOPOROUS SORBENTS: DEGRADATION OF THE STRUCTURE-DIRECTING AGENTS

2.1 Introduction

For many years now, synthetic zeolitic materials have shown properties attractive for adsorptive and catalysis applications.[1-3] Nevertheless, recent industrial chemical processing needs and environmental regulations are now pushing scientists everywhere to develop highly selective and high capacity sorbents and/or catalysts. Much of the effort is focusing on understanding the fundamentals and mechanisms behind the nanoscale-framework assembly process through templated hydrothermal paths.[1, 4-6] Many organic amines, when used as template or structure directing agents (SDAs), produce remarkable structures made up of atomic centers coordinated in such a way as to form interconnected channels and cages. By controlling specific synthesis variables, it is possible to design nanoscale-frameworks capable of allowing exclusive diffusion of certain molecules and/or increase available surface area and void volume.

SDAs are conventionally removed (i.e., detemplation) using high temperature in an oxidative atmosphere to break down and desorb the template via Hoffman elimination and the

spontaneous ionization through the formation of Brønsted acid sites.[7, 8] After the SDA is removed, it is possible to modify the composition and properties of the zeo-type materials to introduce and/or increase exposed extra-lattice species. This will enhance, for example, the adsorption capacity via specific interactions (e.g., van der Waals, electrostatic, and/or chemical). Extra-lattice species could be introduced via a number of ways including, but not limited to, liquid phase (LPIE), solid-state (SSIE), and vapor phase (VPIE) ion exchange, spontaneous monolayer dispersion and wetness impregnation.

Extensive research for the development of structures with ultra-large pore volume have produced materials like VPI-5 and $AlPO_4$-8, which have pore windows of 18- and 14-member rings, respectively.[9-11] However, both materials have frameworks with channels with the largest pore in only 1-D and do not have extra-framework metal cations because their structure charge is neutral. Nevertheless, the isomorphous substitution of AlPO-*n* heteroatoms such as aluminum with transition metals generates negative charge sites in the framework[12, 13] that must be compensated for with a positive charge from any cation available. Incorporation of a transition metal (Me = Co, Mn, Fe, Ti, Cr) into aluminophosphates frameworks is of particular interest for the design of new catalysts for a variety of heterogeneously catalyzed reactions such as oxidations of NO_x and CO, which may have potential application in environmental catalysis.[13-16] Of the divalent metals that can replace framework aluminum, cobalt has attracted considerable attention since, in addition to the Brønsted acidity resulting from incorporation. The variable oxidation state of cobalt

makes these materials good candidates for redox[13, 17-32] and hydrodesulfurization[33] applications, among many others.

Several cobalt-substituted AlPOs, or CoAPOs,[13, 17-32, 34-40] have been synthesized and characterized, but the chemical environment of the isomorphously substituted cobalt is still a topic of discussion. Diffuse reflectance UV–*vis* spectroscopy, for instance, has been used to determine the local geometry of the cobalt sites.[35-37] The technique relies in spectral changes caused by treatment of CoAPOs, which are mainly interpreted on the basis of the intensity change of the characteristic $^4A_2(F) \rightarrow {}^4T_1(P)$ electronic transition with absorption bands in the blue spectral region that enables estimation of the relative concentration of the tetrahedral cobalt centers.[35] Šponer et al.[36] suggested that the apparent concentration increase in the divalent centers at temperatures above 670 K as well as after adsorption of water and small amine molecules corresponds to the reduction of Co(III) centers formed in the course of calcination. Borges et al.[37] concluded that the reversible oxidation of most of the framework Co(II) to Co(III) is probably responsible for the spectral changes that occur after calcination and further reduction. Moreover, their results indicate that a small but a significant part of the framework cobalt suffers irreversible oxidation and the formation of extra-framework cobalt species. These cobalt coordination changes should be responsible for the structure collapsing after calcination treatments and, therefore, should be more predominant at higher Co/Al ratios. Table 2.1 shows typical Co/Al ratios observed in some metal-substituted aluminophosphates.

Table 2.1. Co/Al ratio for several metal-substituted aluminophosphates.

Framework	Co/Al ratio	Reference
CoAPO-18	< 0.04	[13]
CoAPO-5	0.17	[29]
CoAPO-44	0.33	[41]
CoAPO-46	0.35	[41]
Co-APO-50	0.60	[41]
SBS	0.83	[42, 43]
SBT	0.67 – 1.00	[42, 43]
SBE	1.00	[42, 43]

Figure 2.1 depicts SBE building units obtained via molecular visualization (i.e., Accelrys® MS Modeling Software), in both ideal single and multiple SDA filling stages (i.e., the unit cell composition). Bu et al. reported that the specific SDA-framework species interaction in SBE occurs between a primary ammonium cation and an oxygen anion coordinated to tetrahedral atoms while balancing the charge of the framework.[43]

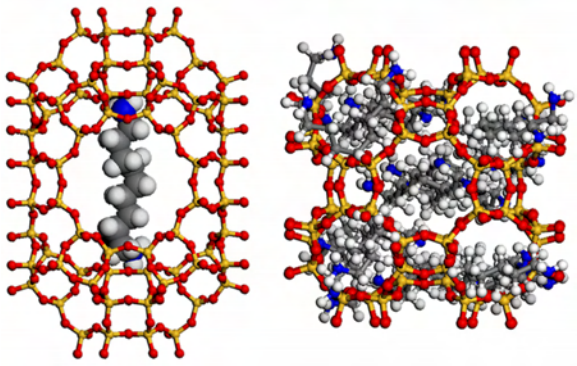

Figure 2.1. SBE supercage filled with one (left) and multiple (right) protonated SDA's. The latter case corresponds to the SBE unit cell theoretical composition. Yellow and red atoms represent metals (i.e., Al, Co or P) and oxygen, respectively. Gray, white and blue atoms represent carbon, hydrogen and nitrogen, respectively.

As potential sorbents, SBE type materials are evidently ideal for adsorption applications where both specific sorption interactions and large void volume are critical. Although the

cation exchange capacity (CEC) of “dehydrated” Co-SBE frameworks (CEC = 3.35 meq/g for Na^+) is lower than the one showcased by dehydrated zeolites such as FAU (CEC = 4.52 meq/g for Si/Al = 2.3 and Na^+), in theory the former material surpasses the latter on the amount of super cages exposed sites. Co-SBE materials should have 16 charge balancing sites per super cage compared to only a few usually found in FAU supercages.[44, 45] However, access to these Co-SBE outstanding properties requires the complete or at least partial removal of the SDA using techniques capable of overcoming the low stability of the structure due to the cobalt coordination chemistry or metastability.

The following discussion presents thermal gravimetric analysis (TGA) data that were used to verify the template decomposition path in oxidative and inert atmospheres, respectively. The as-synthesized and pre-treated Co-SBE samples were also characterized using X-Ray Diffraction (XRD), Scanning Electron Microscopy (SEM), UV-*vis*, Raman, and Fourier Transform-Infrared (FT-IR) spectroscopy, and volumetric adsorption techniques, respectively. In addition, the following discussion presents the optimized synthesis of Co-SBE powder material (instead of single crystals) via extended aging periods.

2.2 Experimental Section

2.2.1 Co-SBE Synthesis Procedure

Co-SBE samples were synthesized in house hydrothermally. Reagents used to prepare solution A were aluminum isopropoxide (98%, Aldrich), 85-wt% *o*-phosphoric acid (Aldrich), and ethylene glycol (99%, Aldrich). Solution A was stirred for 24 hours or one

week to provide different aging periods. Solution B was prepared using cobalt carbonate hydrate (Aldrich), 85-wt% *o*-phosphoric acid (Aldrich), and deionized water. Carbon dioxide evolved when *o*-phosphoric acid was slowly added to the mixture of deionized water and cobalt carbonate hydrate. Solution B was stirred at room temperature for 15 minutes. Solution A and B were mixed together and stirred at room temperature for 20 minutes until homogeneous (pH = 3.46). The organic template, 1,9-diaminononane (98%, Aldrich, solid wax, DAN) was slowly added under constant stirring for up to 20 minutes. At the mixture pH level, DAN molecules are protonated and templating starts. A co-solvent, dipropylamine (99%, Aldrich, DPA), was added dropwise until the pH of the final solution was 7.6. Final gel composition was $0.5C_9H_{24}N_2O:2.5C_6H_{16}NO:CoO:0.5Al_2O_3:P_2O_5:50H_2O$. The sol-gel solution was then transferred to a 45 mL Teflon-lined stainless-steel autoclave (Parr Instruments Co., Moline IL) and heated at 443 K for 168 hours in a forced convection oven. After synthesis, the autoclave was quenched to room temperature. Intense blue-colored crystals were recovered by standard vacuum filtration, washed with copious amounts of deionized water and ethanol and dried to 363 K overnight also in a forced convection oven. A second batch was synthesized hydrothermally following the same procedure used for the Co-SBE sample, but using only DPA as the template. Final gel composition was $2.5C_6H_{16}NO:CoO:0.5Al_2O_3:P_2O_5:50H_2O$.

2.2.2 Materials Characterization

As-synthesized and treated samples were characterized by X-Ray Powder Diffraction (XRD) and Scanning Electron Microscopy (SEM). XRD analyses were performed using a Rigaku

ULTIMA III X-Ray Diffraction cross beam optics equipment (CuK_{α}) operating at 40 *k*V and 44 *m*A. The diffraction angle *(2θ)* range was set to 3-60°. The step size and speed (step scan) were 0.04° and 2°/min, respectively.

SEM images were obtained using a JEOL JSM-5410LV instrument (UPR-Mayagüez, Biology Department). The morphologies of SBE samples were captured using an accelerating voltage of 10.0 *k*V. Samples were coated (EMS 550 Sputter Coater, UPR-Mayagüez, Biology Department) with gold to improve secondary electron emission and prevent charging. Elemental distribution of the samples was performed using a JEOL-JSM 6460LV Scanning Electron Microscope fitted with an Energy Dispersive X-ray (EDX) spectrometer (EDS, 10.0 KV, SUTW-Sapphire Detector).

2.2.3 Adsorption Isotherms and Weight Loss Profiles

Nitrogen adsorption isotherms as well as surface area measurements were performed using nitrogen at 77 K as described elsewhere.[3, 46, 47] CO_2 adsorptions isotherms were performed at 298 K. A static volumetric adsorption unit (Micromeritics ASAP 2020) was used for such analyses. Before measurements, the samples were degassed at a heating rate of 5 K/min and an evacuation rate of 50 mm Hg/s for 18 h. The specific surface occur area was determined according to the Langmuir method[1] in the relative pressure range of 0.01–0.20. Thermal Gravimetric Analysis (TGA) was performed using a TA-2950 thermobalance, varying the

[1] SBE frameworks are microporous materials and it is assumed that the N_2 adsorbed molecules fill the pores completely and that multilayer adsorption does not take place.

heating rate from 10 K/min to 30 K/min over a temperature range from ambient to 1,173 K using inert or air flow (ultra high purity grade) at 60 mL/min. All gases were pretreated using pre-sorbers (i.e., 3A Zeolites) to remove any traces of water and other contaminants. TGA was conducted to investigate the thermal behavior of the samples and the energy of desorption for the structure-directing agent elimination.

2.2.4 Desorption Activation Energies

Estimates of desorption energies for weakly and Hoffman-like bonded templates were obtained using TGA data and Redhead's equation for first-order kinetics (Equation 2.1):[48-52]

$$\frac{E_d}{RT_m^2} = \frac{A}{\beta}\exp\left(-\frac{E_d}{RT_m}\right) \qquad (2.1)$$

where T_m is the temperature at peak maximum, β is the heating rate, E_d is the activation energy, and A is a pre-exponential factor. The derivative of the TGA data was used to determine T_m.

2.2.5 UV-*vis* Absorption Spectroscopy

Absorption spectra of as-synthesized SBE and samples pre-treated in vacuum at 673 K were collected at room temperature using a Varian Cary 500 Scan UV-*vis* Spectrometer in single-beam mode. Samples were prepared in the form of KBr pellets. A background spectrum of KBr was recorded to confirm the absence of absorption bands in the region measured.

2.2.6 Raman and FT-IR Spectroscopy

Raman Spectroscopy was applied to as-synthesized and vacuum pre-treated SBE samples at 673 K. Raman spectra were collected using a micro-Raman setup (HR800, Horiba/Jobin-Yvon, Bensheim, Germany) with a focal length of 800 mm and a 40x antireflection-coated objective (LMU UVB). An excitation wavelength of 244 nm was applied using the frequency-doubled line of an Argon-ion laser (Innova 300D FReD, Coherent, Dieburg, Germany). A CCD camera equipped with an Olympus BX-41 microscope attachment detected the Raman scattering in the range of 100-3500 cm^{-1}. FT-IR in the attenuated total reflection (ATR) absorbance spectra on the as-synthesized sample and the vacuum treated samples at 673 K were recorded on a Varian 800 FT-IR SCIMITAR series spectrometer, with a resolution of 4 cm^{-1} using a signal gain of 100 scans per sample. The FTIR-ATR samples were degassed at 423 K prior to analysis and scanned in an out-of-compartment horizontal ATR accessory (PIKE MIRacle^{TM} Single Reflection ZnSe HATR) in the range of 4000-600 cm^{-1}.

2.2.7 Molecular Modeling of Template Interactions in SBE Frameworks

Theoretical calculations to optimize the structure of 1,9-diaminononane (DAN), protonated DAN molecules, and framework the cluster model were performed using *Gaussian03* software. Calculations were made using *ab-initio* Hartree-Fock and DFT methods. LANL2DZ was the basis set chosen for the organic molecules as well as for the cluster model. For atoms beyond the third row of the periodic table, which have very large nuclei, this basis set is the most used.[53] Cluster model atoms were not frozen because the

interaction with the amine is a result of its formation and not an adsorption process. Different sorbate-sorbent combination or scenarios were established to be able to compare with experimental data (i.e., desorption energy) and in an effort to determine sorbent clusters and sorbate-sorbent pairs interaction energies, relevant bond distances, and study interactions between SBE framework and the SDA.

2.3 Results and Discussion

2.3.1 Synthesis and Characterization

It was necessary to find optimized synthesis conditions for the preparation of powder crystals of Co-SBE since Bu et al. originally prepared single crystals.[43] These conditions included decreasing the reaction temperature to 443 K and increasing the aging time to one week. The presence of a crystalline SBE phase after synthesis was verified by XRD. Figure 2.2 shows the diffraction pattern of the as-synthesized Co-SBE sample as well as the refined unit cell. The latter was obtained after eliminating unknown phase or impurity peaks, also shown in Figure 2.2. The observed difference in intensity ratios is probably due to preferential orientation of the powder crystals. Nevertheless, the diffraction data is in well agreement with the simulated pattern reported by the International Zeolite Association (IZA) based on Stucky and co-workers single crystal diffraction data.[43, 54] In addition, the as-synthesized SBE samples had an intense blue color, which is characteristic of divalent cobalt in a tetrahedral environment.[17, 36-38, 55, 56] A semi-quantitative EDX analysis indicated that the as-

synthesized samples indeed have a high cobalt concentration framework typical of SBE: *Co/Al* ~ 0.85 and *(Co+Al)/P* > 0.9.

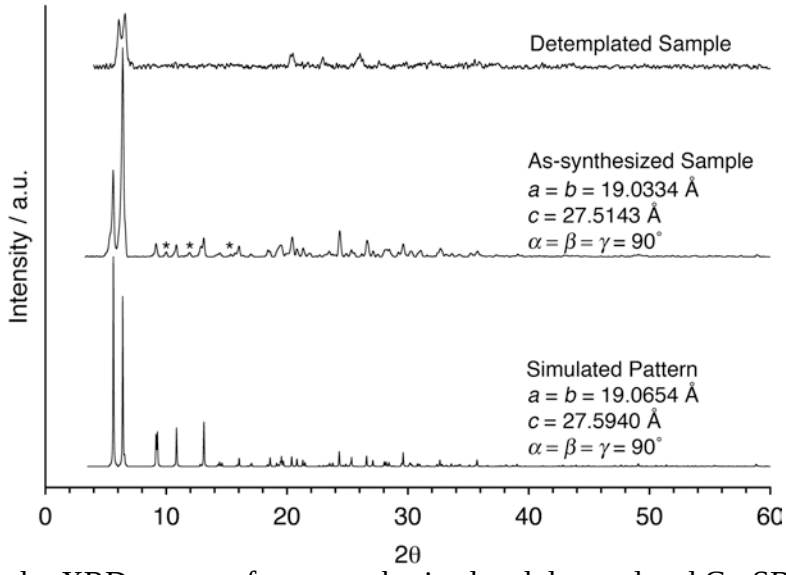

Figure 2.2. Powder XRD patterns for as-synthesized and detemplated Co-SBE, respectively. The simulated XRD pattern for SBE was obtained using the single-crystal data from Stucky and co-workers.[43, 54]

The original synthesis procedure[43] included a one day aging step, which resulted in SBE single crystals displaying square plate with truncated corners morphologies. SEM image analysis in the present study indicates that increasing the aging time to one week produces Co-SBE hexagonal plates with a crystal size of ca. 20 μm (Figure 2.3A). The evident pitting of the as-synthesized crystals could be attributed to the instability of aluminophosphates in their mother liquor.[1] The imaging test also shows the presence of small cube-like phases, which could be attributed to some sort of unknown phase and that qualitatively correlates with the "extra peaks" observed in the as-synthesized sample XRD pattern (Figure 2.2). It should be mentioned that the observed Co-SBE hexagonal plates morphology is quite similar

to the one exhibited by SBT type materials reported by Bu[43] and Goldfarb.[57] However, the SBT XRD pattern is substantially different from the one exhibited by SBE frameworks.

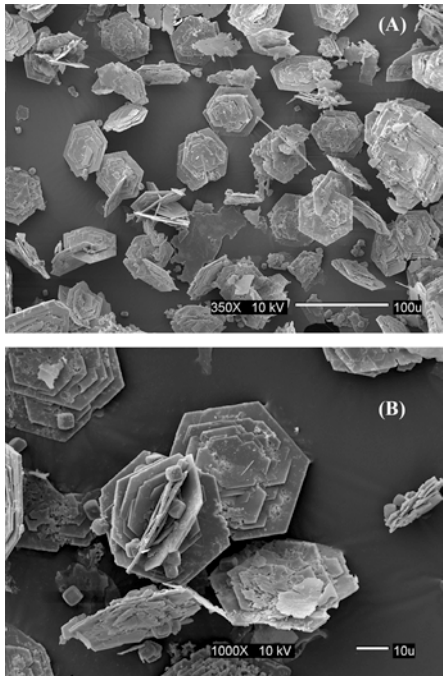

Figure 2.3. SEM for (A) as-synthesized and (B) pre-treated Co-SBE materials, respectively. Synthesis performed using extended aging of reactive gel (solution A). Detemplation performed in vacuum at 673K.

At this point of the discussion, it is necessary to also comment on the role of DPA in the templating process. Mali et al.[58] revealed the formation of dipropylammonium cations as the result of the protonation of DPA to compensate the lack of positive charges by the substitution of trivalent aluminum with divalent metals, such as cobalt and manganese in the synthesis of CoAPO-31 and MnAPO-31. In the present work, samples synthesized using only DPA as the SDA also showed a crystalline XRD pattern, but with different peak positions and intensity as compared to SBE samples (Figure 2.4). As indicated by Bu et al.,[43] DPA

only helps to increase the solubility of *protonated* DANs to levels necessary for hydrothermal templating.

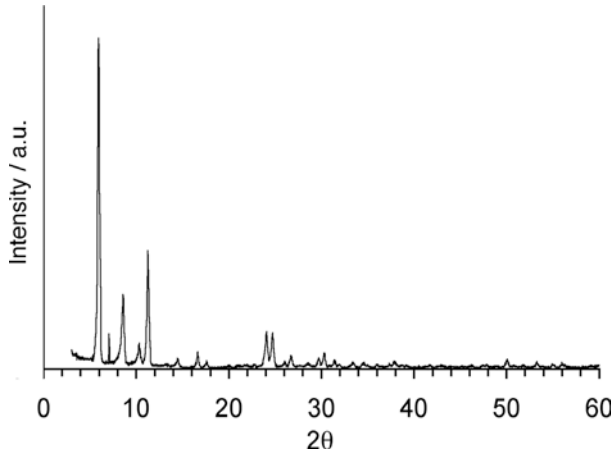

Figure 2.4. XRD pattern for sample prepared using only DPA as the structure-directing agent.

2.3.2 Treatments for SDA elimination: Calcination in oxidative and inert atmospheres

During the process of detemplation, defects or pressure-induced stresses caused by decomposition of the template from solid to gas within the zeolite framework could result in disintegration or structure collapse. When synthesized, Co-SBE shows a bright blue color. On the other hand, when calcined in air at 673 K, the sample turned black in color suggesting the extraction of metal atoms from the framework and the formation of oxides or oxyhydroxides[59, 60] or the presence of carbonaceous species that arise from thermal cracking during template decomposition. These were certainly responsible for the low surface areas (see Table 2.2) observed for Co-SBE calcined samples. In terms of the framework, the XRD

data for the samples calcined in air revealed its destruction and formation of an amorphous phase (i.e., no peaks were observed), which again correlates with the surface area results.

Table 2.2. Langmuir surface area and *t*-plot analysis results for Co-SBE samples.

Sample ID	Langmuir Surface Area (m^2/g)	*t*-Plot Micropore Area (m^2/g)	*t*-Plot External Surface Area (m^2/g)
As-synthesized SBE	7	------	------
Calcined in air	6	2	4
Calcined in nitrogen	12	3	10
Vacuum treated	318	276	43

As shown in Figure 2.5, for as-synthesized samples and samples treated in nitrogen and air at a high temperature (all degassed at 423 K prior to the adsorption tests), the adsorbed amount of nitrogen molecules at room temperature in the micropore region evidences how detrimental is an oxidative thermal treatment for the Co-SBE framework. It should be mentioned that the relative low sorption capacity of the nitrogen treated sample was probably due to water that re-adsorbed upon hydration with ambient air after the thermal treatment. It is well known that zeo-type materials require activation temperatures above 623 K for the complete removal of water molecules, including intracrystalline.[3, 46] Therefore, it was decided to couple the detemplation and degassing stages into one at 673 K under vacuum conditions. This approach resulted in higher surface areas (Table 2.2), which, as determined by a *t*-plot analysis, product from the presence of micro(nano)pores. Figure 2.6 shows nitrogen equilibrium adsorption isotherms that clearly show the presence of nanoporous channels.

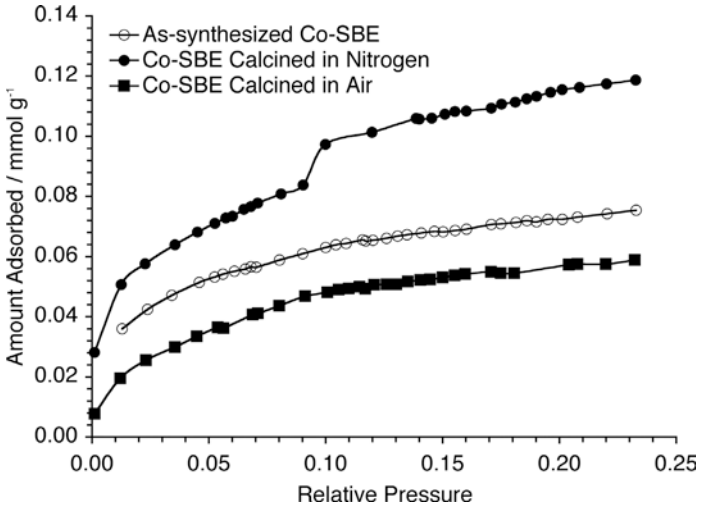

Figure 2.5. Nitrogen adsorption isotherms at 77 K for as-synthesized Co-SBE, Co-SBE calcined in air at 673K and Co-SBE calcined in nitrogen at 673K, respectively.

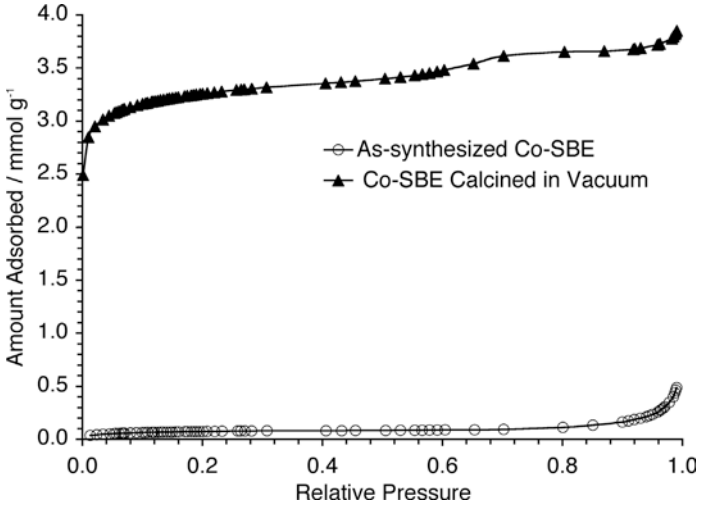

Figure 2.6. Nitrogen adsorption isotherms at 77 K for as-synthesized Co-SBE and Co-SBE pre-treated in vacuum at 673K, respectively.

The vacuum treated Co-SBE materials remained blue in color and with a crystalline appearance. Evidence that the morphology of the crystals was not greatly affected is shown in Figure 2.3B. However, pore size determination using the corrected Horvath-Kawazoe

method for spherical shaped pores[61, 62] indicated that the average cage diameter was ca. 9Å, which clearly indicates some sort of structural changes and/or that some SDA residue remained within the pores volume (i.e., amines). The XRD pattern for the treated sample (Figure 2.2) evidences a considerable intensity reduction as well as peak shifting, which correlates with structural shrinkage. The peak displacement across the pattern is not constant, indicating the possibility of a non-uniform framework distortion. Martucci et al.[63] reported a significant unit cell size reduction in CoAPO-34 materials accompanied by a distortion in which the aperture of the window decreased progressively upon calcination in the 698 – 923 K range. For high Co/Al ratios such unit cell size reduction should be observed at lower temperature ranges due to the cobalt sensitive coordination state. In fact, Lohse et al. found that the temperature of structure collapse of certain CoAPOs significantly decreased as a function of cobalt content of the sample.[64]

It should be mentioned at this stage of the discussion that even SBE-like materials with amine residues within the pore cages and channels could result in good sorbent candidates for applications involving removal of carbon dioxide (CO_2). The idea of using porous materials with occluded amine-containing species to remove carbon dioxide has been considered before.[52, 65] Hernández-Maldonado et al. found that the CO_2 molecules underwent considerable interactions with amine residues occluded in SAPO-43 samples after partial calcination. Their results were based on isosteric heats of adsorption, which were higher than those expected in traditional commercial materials (i.e., van der Waals range).[52]

2.3.3 UV-*vis* Absorption Spectroscopy

The spectrum of the as-synthesized material (Figure 2.7) exhibits a single, sharp absorption band at 349 nm that is assigned to the ligand-to-metal charge transfer (LMCT) for oxygen groups to cobalt. In addition, there are two prominent bands at 598 and 629 nm that can be assigned to the Co(II) *d-d* transition band and identified as Co(II) in a tetrahedral environment characteristic of the $^4A_2(F) \rightarrow {}^4T_1(P)$ transition.[36, 37, 66] After treatment in vacuum, the sample spectra did not show significant changes, which indicate that, the cobalt species oxidation and/or coordination state was not greatly affected.

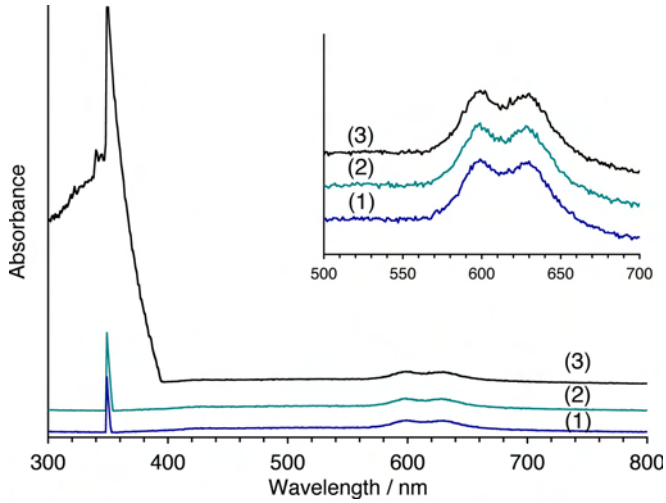

Figure 2.7. UV-*vis* absorption spectra for (1) as-synthesized Co-SBE, (2) Co-SBE after treatment in vacuum at 673 K, and (3) Co-SBE after treatment in air at 673 K.

The same cannot be said about the sample treated in an oxidative atmosphere at 673 K. The 349 nm band now shows a broad and increase absorption that corresponds to Co(III) in an oxygen environment.[66] The broadening of such peak is also attributable to formation of

extra-framework Co_xO_y species[36, 37] associated to non-framework trivalent cobalt species. Although the samples calcined in air also showcase bands associated to the presence of Co(II) tetrahedra, the aforementioned sample black color suggests that much of the metal is now present in the form of Co_xO_y. It should be mentioned that Šponer et al.[36] suggested the presence of distortion-induced charge transfer effects without changing the oxidation state after calcination of CoAPO-5 and -11.

2.3.4 Thermal (TG/DTG) and Redhead's Analyses

Figure 2.8 shows TG data for detemplation in SBE at 10 K/min in oxidative and helium (or nitrogen) atmospheres, respectively. TGA showed that the overall weight loss in the ambient to 1,173 K range is very similar for SBE samples at all heating rates (e.g., 10, 20 and 30 K/min). There is a significant weight loss in the lowest temperature range, which is due to water molecules being eliminated from the surface. For samples treated in inert gas, the bulk of the organic template (1,9-diaminononane) is eliminated at ca. 670 K (see Figure 2.8). However, for Co-SBE treated in air, a significant fraction of products of the template decomposition is only eliminated at temperatures higher than 900 K, probably due to their encapsulation upon the framework collapsing at lower temperatures.

Desorption energies (Table 2.3 and Figure 2.10) of 132 and 165 kJ/mol for the desorption and Hofmann elimination of DAN, respectively, were obtained for the oxidative atmosphere. The value of 165 kJ/mol is not too far from the value of 140 kJ/mol obtained by Hernández-

Maldonado and Yang[52] in 2003 for the decomposition of isopropylamine by a Hoffman elimination process from SAPO-43. Afterwards, they could only partially calcine the silicoaluminophosphate to obtain a nanoporous sorbent.

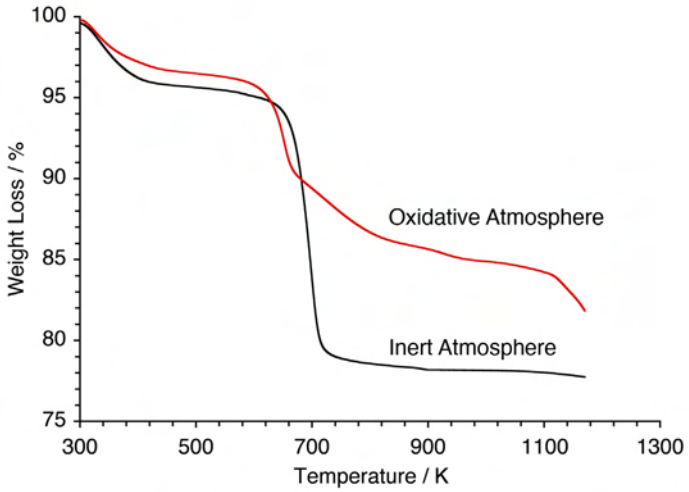

Figure 2.8. Co-SBE TG profiles at 10 K/min. Calcination done under oxidative and inert atmospheres, respectively.

DTG analysis (Figure 2.9 and Table 2.3) showed a fourth region possibly related to the oxidation of the organic material. Although the role that oxygen plays in the decomposition mechanism is still unclear, the appearance of an additional peak could suggest that template decomposition occurs by pyrolysis and/or oxidation, depending on the atmosphere used to calcine the sample. It is believed that alkylammonium ions from adsorbed protonated alkyldiamines through the generation of Brønsted sites decompose to ammonia and olefins via a reaction similar to the Hoffman-elimination reaction.

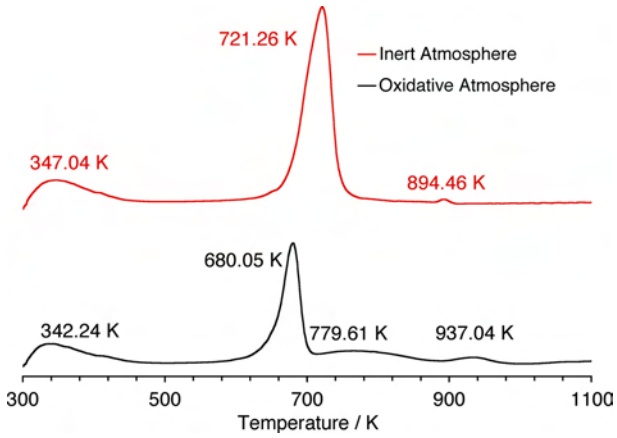

Figure 2.9. Co-SBE DTG profiles at a heating rate of 30 K/min.

Table 2.3. Redhead's analysis data. Refer to Figure 2.9 for DTG data.

		Oxidative Treatment		Inert Atmosphere Treatment	
Region	β(K/min)	T_m (K)	E_d (kJ/mol)	T_m (K)	E_d (kJ/mol)
1	10	327.16	50.91	336.21	64.61
	20	341.84		348.69	
	30	342.24		347.04	
2	10	651.92	132.24	697.79	182.89
	20	670.04		713.11	
	30	680.05		721.26	
3	10	749.82	165.15	---	---
	20	769.42		---	
	30	779.61		---	
4	10	927.45	438.92	---	---
	20	941.06		---	
	30	937.04		---	

Analysis of template removal using thermal gravimetrical analysis in helium atmosphere showed only three major weight losses attributed to the desorption of intracrystalline water, and to the alkene (1,8-nonadiene) and ammonia produced during the Hoffman reaction of the amine. Combined with experimental observations (i.e., sample color) and the results

mentioned above, it seems that treatment with inert gas provides a simple method to decompose most of the SDA.

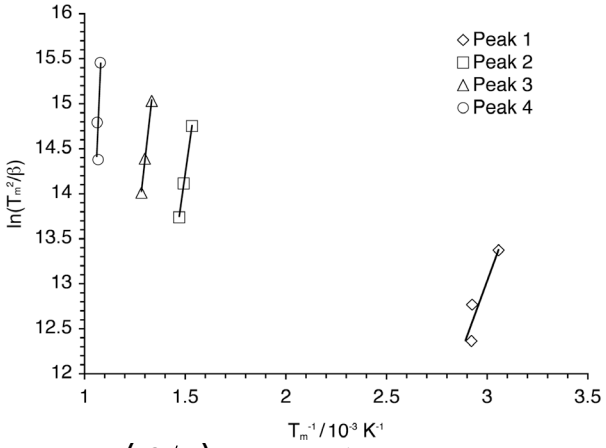

Figure 2.10. Plot of $\ln\left(T_m^2/\beta\right)$ versus T_m^{-1} for template removal of Co-SBE.

The scheme shown in Figure 2.11 depicts the suggested mechanism of the alkylammonium ion elimination via a Hoffman degradation path in non-oxidative environments. This elimination path is being proposed based on the TG/DTG data analysis. The first step consists of the production of the formation of 1,8-nonadiene and ammonium cations. The former corresponds to approximately 17-wt% of the unit cell composition, which matches very well with the second weight loss region observed in the TGA curves. The second and last step should correspond to the elimination of ammonia and, therefore, formation of proton sites. However, the last weight loss region quantified during the TGA analysis does not correlate to the desorption of two ammonia molecules per unit cell. This indicates that perhaps some other species are balancing new charges that could result during the SBE material treatment. It should be mentioned that the volatile compounds eliminated during the

TGA runs could not be identified and, therefore, the proposed mechanism would need validation in the future using combined mass spectrometry (MS)/FT-IR/TGA to identify such evolved species.

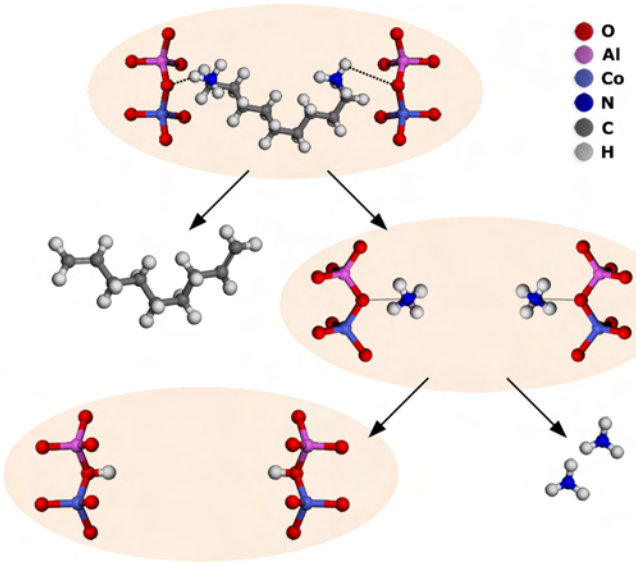

Figure 2.11. Proposed mechanism for Hoffman elimination reaction. Light shade represents a segment of the zeolite framework.

2.3.5 Raman and FT-IR Spectroscopy

Figure 2.12 shows the Raman spectra of as-synthesized Co-SBE, Co-SBE treated in vacuum at 673K, and DAN, respectively, after being exposed to an excitation wavelength of 244 nm. It was quite difficult to observe Raman bands associated to the chemical environment of the template or the cobalt in the aluminophosphate framework. Regarding the protonation of the alkyldiamine, 1,9-diaminononane, the treatment process resulted in the loss of the N-H stretch, and NH_2^+ vibrations that give rise to weak Raman bands below 3000 cm^{-1} as suggested by Ashtekar et al.[67] Modes in the 1100-600 cm^{-1} are sometimes related to the bending and stretching of bridging oxygen (Al-O-P angles).[68-70] Bands below 800 cm^{-1},

usually corresponding to the breathing mode of the sieve channel opening, were observed in the vibrational spectra of the cobalt aluminophosphate system as a broad band in the lower frequency region that was associated to the SBE framework (Figure 2.12). A prominent band in the 3000-2800 cm^{-1} region was associated to the organic template present inside the crystals due to CH_2 groups[71] that disappeared after the sample was pre-treated in vacuum at 673K. N-H stretching bands were also observed in the 3300-3200 cm^{-1} region for all the samples. For the vacuum treated sample, this band is associated to the presence of ammonium cations. Raman spectroscopy cannot reveal precise information about the nature of template-framework coordination. FT-IR in the attenuated total reflection (FTIR-ATR) absorbance spectra was also used to elucidate more information about the removal of the organic template and the consequences of this on the structural characteristics.

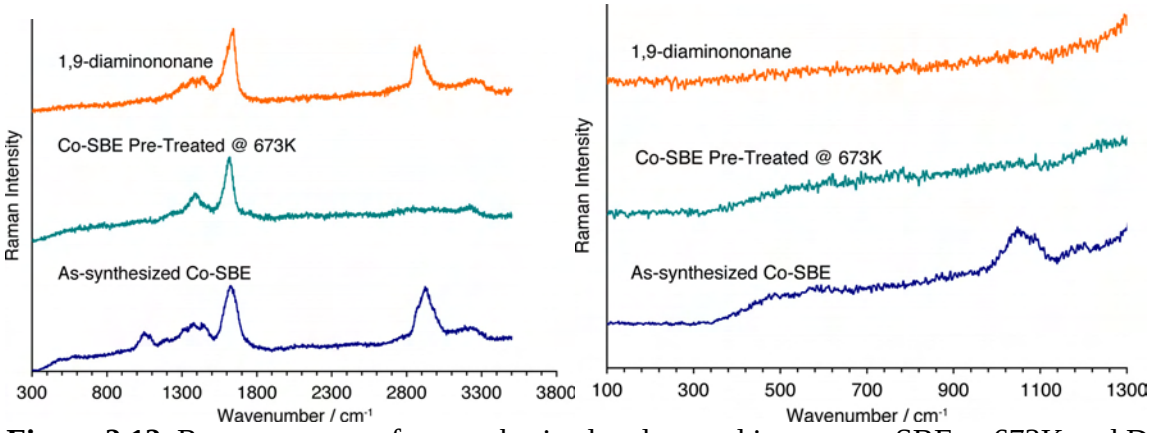

Figure 2.12. Raman spectra of as-synthesized and treated in vacuum SBE at 673K and DAN.

Figure 2.13 shows infrared spectra (in absorbance) of as-synthesized and vacuum treated SBE, respectively, and DAN. Strong bands due to fundamental vibration of the framework were seen in the 1400-650 cm^{-1} region and associated to symmetric and asymmetric

stretching of the TO_4 tetrahedra.[72] Internal vibrations of the SBE unit cell due to symmetric stretching modes[73-77] are observed at 744 and 729 cm^{-1}, for the as-synthesized and treated SBE, respectively. The presence of a broad and intense peak at 1031 cm^{-1} in the FTIR spectra for the as-synthesized SBE and at 1062 cm^{-1} for the treated sample was associated to the asymmetrical T-O stretching modes.[73-77] This shift in the frequency is correlated to the protonation of the zeolitic lattice[74] which induces the shift of such features to a higher wavenumber. It should be mentioned that such peak broadening is typical of cobalt substituted aluminophosphates.[64] Weak bands at 1616, 1523 and 1473 cm^{-1} are related to deformation modes of CH_2 groups and N-H bending for the as-synthesized SBE. These are observed with a higher intensity in the 1,9-diaminononane spectra, probably because of the strength of the hydrogen bonding.[78] For treated samples, these bands are associated to the presence of ammonium ions. The observed absorption bands in the 3500-2800 cm^{-1} region are associated to the C-H and N-H stretching vibrations due to occluded template molecules in the as-synthesized SBE samples that reduced its intensity from pre-treated samples. These bands still remained in the treated SBE (2939 and 2974 cm^{-1}), but now showcasing lower intensities and shifting to higher frequencies. The disappearance of CH_2 bands and reduction in the intensity of amine bands were related to the removal of the organic species from the framework. Bands associated to the ring vibrations, T–O–T bending or breathing of the pore opening in the analyzed samples were impossible to detect due to limitations in the instrument range.

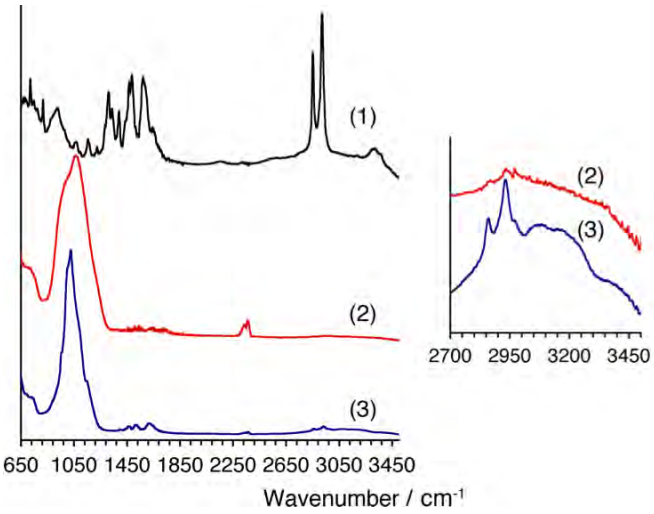

Figure 2.13. FT-IR spectra of (1) DAN, (2) SBE pre-treated in vacuum at 673K, and (3) as-synthesized SBE, respectively.

2.3.6 Molecular Modeling of Template Interactions in SBE Frameworks

1,9-diaminononane is the linear alkyldiamine used for the synthesis of SBE, which becomes protonated during the synthesis. The specific template-framework species interaction is transformed into a N–H···O interaction in the SBE framework structure.[43, 79] The charge on the inorganic framework is adjusted to the organic template charge by restructuring the framework assembly.[43, 79] Bu and Stucky allowed the charge requirements of the organic template determine the framework composition and charge, where the net negative charge of the framework is therefore balanced by the protonated amine.

The supercages in the structure of SBE are body centered. It was estimated that there are eight amines per cage and two cages per unit cell. The atomic coordinates available from IZA Structures Database, which include the positions of the amine, facilitate the construction the SBE structure.[54] The resulting cage was symmetrical and the interaction of each amine is

with an eight-oxygen ring, which is not located in the orthogonal channels of the structure (Figure 2.14). Problems arise trying to assign Al or Co sites because the probability of finding Al occupying a certain position is the same that those of Co atoms. The unit cell composition of SBE is $|(C_9H_{24}N_2^{2+})_{16}|$ $[Al_{32}Co_{32}P_{64}O_{256}]$-SBE where $(C_9H_{24}N_2^{2+})$ is the protonated amine. It has the same number of cobalt and aluminum atoms and half of the number of phosphorus atoms. It should be mentioned that the phosphorus T-atoms could coordinate to aluminum or to cobalt. A number of cases were proposed for cluster models trying to estimate the interaction energy:

1. Amines weakly bonded to surface: non-protonated amines.
2. Cobalt as the T-atom and coordinated to two amines.
3. Amine bent and coordinated to cobalt as the T-atom
4. Aluminum as the T-atom and coordinated to one amine.

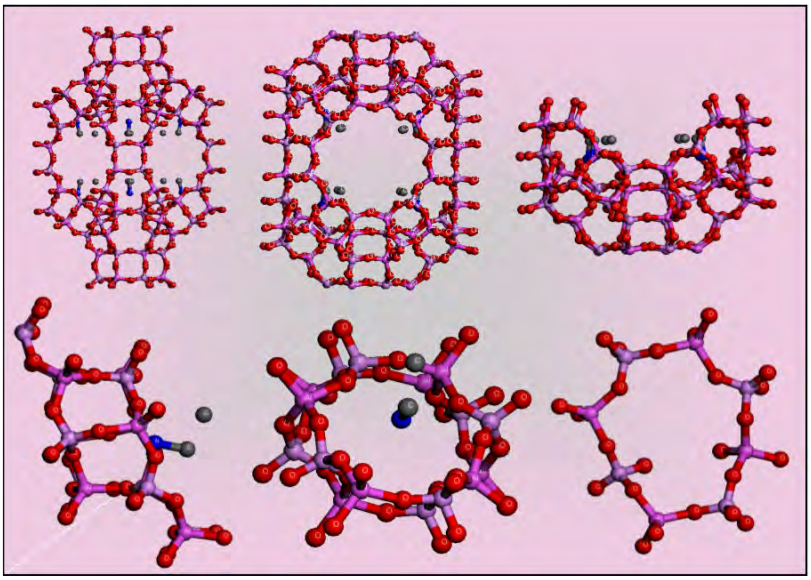

Figure 2.14. Cluster model proposed for computational calculations.

The results for the optimized molecules using *Gaussian03* software are presented below (Table 2.4). Calculations were done using Hartree-Fock and DFT methods. The interaction energy (Equations 2.2 and 2.3), or the energy of adsorption (ΔE), can be calculated from energy of sorbate-sorbent (E_{AB}), energy of free sorbate (E_A), and energy of free sorbent (E_B):

$$\Delta E = E_{AB} - E_A - E_B \qquad (2.2)$$

$$\Delta E = E_{cluster-amine} - E_{amine} - E_{cluster} \qquad (2.3)$$

Figure 2.15 displays the images obtained after the optimization of the amine molecules and Figure 2.16 the ones for the aluminum cluster. The basis set chosen (i.e., LANL2DZ) was the same used for the cluster model. Because of the infinite dimension of solids, it is important to select a finite structure that can adequately represent the periodic structure. For economy in computation, however, the cluster structure shown in Figure 2.16 was selected for the calculations. These clusters have the formula $(HO)_4$-P-Al$(OH)_2$-$(OH)_4$ and results from truncation of the original cluster (i.e., eight-membered ring). However, it contains the essential structural and chemical information of the interaction sites, including the charge, and the Al/P ratio. In addition, following the analogy of Nicholas, rather than being directly saturated by hydrogen, the Al and P atoms are now surrounded by oxygen atoms.[80]

Figure 2.15. 1,9-diaminononane (left) and protonated 1,9-diaminononane (right).

Table 2.4. Energy values obtained from *Gaussian 03*.

	DFT	**HF**	**ΔE**
SCF (Self Consistent Field)	E (RB+HF-LYP)	E(RHF) or E(UHF)	-----
1,9-diaminononane	-465.6	-462.4	-----
protonated DAN	-466.3	-463.1	-304.9
aluminum cluster	-----	-768.0	
cobalt cluster	-----	Convergence criterion not met. -909.3	-446.2

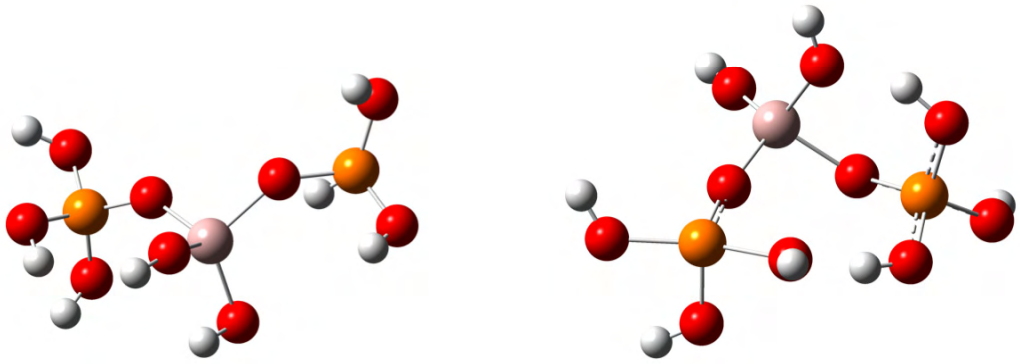

Figure 2.16. Aluminum cluster model prior (left) and after the optimization (right).

Questions arise regarding whether the energy calculated for the cluster model was a *"true"* value. It can be seen from the results that the value of the energy for the aluminum cluster is smaller than the one calculated for the cobalt cluster relative to the protonated amine, although it did not met the convergence criterion. In the final structure (Figure 2.16) there are additional bonds in the oxygen atoms coordinated to phosphorus T-atoms, like the ones seen for aromatic bonds. For case I, if the amine is weakly bonded, a long coordination distance should be consistent with a weak binding energy (in the same range of physical adsorption). For the other case, (protonated amine) the expected value of energy should be higher than for case I.

2.4 Conclusions

While Co-SBE powder synthesis was successfully obtained by increasing aging time and decreasing reaction temperature, the observed particle morphology differs from the one previously reported for single crystals. In terms of detemplation, calcination in an oxidative atmosphere greatly influences the structural stability of cobalt-substituted SBE as evidenced by UV-*vis* spectroscopic analysis and the low surface area displayed by the treated material. Cautious vacuum treatment, however, results in a microporous sorbent with features similar to that of the as-synthesized sample as determined by UV-*vis,* Raman and FT-IR analyses. Nevertheless, porosimetry and XRD data showed that the Co-SBE material was affected to some extent upon the inert treatment as the resulting average cage size decreased considerably.

TGA measurements and a Redhead's analysis corroborated that 1,9-diaminononane SDA is not just a space-filler (non-dissociated ion pair). The template experiences a strong interaction with the host framework and this, together with the cobalt tetrahedra metastability, introduces a high degree of complexity when trying detemplation. Our group also applied other techniques, such as solvent extraction and ion exchange, to address this problem and the results are reported in Chapter 4. In general, this study has demonstrated that SBE could be a suitable nanoporous material for adsorption related applications.

2.5 Acknowledgements

The work presented in Chapter 2 was supported by the National Science Foundation Awards CBET-0546370 and CBET-0619349. Support from the Alfred P. Sloan Foundation and the GEM Consortium is also gratefully acknowledged. SEM images were gathered at the Microscopy Center of the UPR-Mayagüez at the Biology Department. Help from professors Dr. Nelson Cardona-Martínez, Dr. Carlos Rinaldi (UPR-Mayagüez, Chemical Engineering) and Dr. Samuel Hernández (UPR-Mayagüez, Chemistry) for providing access to FT-IR and Raman spectroscopic analyses, respectively is also acknowledged. UV-*vis* spectroscopic analysis was provided by Dr. Raphael Raptis and Dr. Indranil Chakraborty (UPR-Río Piedras, Chemistry).

LITERATURE CITED

[1] Szostak, R., Synthesis of Molecular Sieve Phosphates In *Molecular Sieves - Science and Technology*, Springer Berlin / Heidelberg: 1998; Vol. 1, pp 157-185.

[2] Pfenninger, A., Manufacture and Use of Zeolites for Adsorption Processes. In *Molecular Sieves: Science and Technology*, Karge, H. G.; Weitkamp, J., Eds. Springer-Verlag: Berlin ; New York, 1999; Vol. 2, pp 163-198.

[3] Yang, R. T. *Adsorbents: Fundamentals and Applications*. Wiley: New York, 2003.

[4] Thompson, R. W., Recent Advances in the Understanding of Zeolite Synthesis. In *Molecular Sieves: Science and Technology*, Karge, H. G.; Weitkamp, J., Eds. Springer-Verlag: Berlin ; New York, 1998; Vol. 1, pp 1-33.

[5] Davis, M. E. Ordered Porous Materials for Emerging Applications. *Nature* **2002**, *417*(6891), 813-821.

[6] Davis, T. M.; Drews, T. O.; Ramanan, H.; He, C.; Dong, J. S.; Schnablegger, H.; Katsoulakis, M. A.; Kokkoli, E.; McCormick, A. V.; Penn, R. L.; Tsapatsis, M. Mechanistic Principles of Nanoparticle Evolution to Zeolite Crystals. *Nat. Mater.* **2006**, *5*(5), 400-408.

[7] Gorte, R. J.; White, D. Interactions of Chemical Species with Acid Sites in Zeolites. *Top. Catal.* **1997**, *4*(1-2), 57-69.

[8] Moissette, A.; Marquis, S.; Gener, I.; Bremard, C. Sorption of Anthracene, Phenanthrene and 9,10-Dimethylanthracene on Activated Acid HZSM-5 Zeolite: Effect of Sorbate Size on Spontaneous Ionization Yield. *Phys. Chem. Chem. Phys.* **2002**, *4*(22), 5690-5696.

[9] Davis, M. E.; Saldarriaga, C.; Montes, C.; Garces, J.; Crowder, C. A Molecular-Sieve with 18-Membered Rings. *Nature* **1988**, *331*(6158), 698-699.

[10] Dessau, R. M.; Schlenker, J. L.; Higgins, J. B. Framework Topology of AlPO4-8: The 1st 14-Ring Molecular-Sieve. *Zeolites* **1990**, *10*(6), 522-524.

[11] Freyhardt, C. C.; Tsapatsis, M.; Lobo, R. F.; Balkus, K. J.; Davis, M. E. A High-Silica Zeolite with a 14-Tetrahedral-Atom Pore Opening. *Nature* **1996**, *381*(6580), 295-298.

[12] Silva, A. O. S.; Souza, M. J. B.; Araujo, A. S. Hydrothermal Synthesis and Thermal Characterization of Niobium-Aluminophosphate with AEL Structure. *Int. J. Inorg. Mater.* **2001**, *3*(6), 461-466.

[13] Thomas, J. M.; Greaves, G. N.; Sankar, G.; Wright, P. A.; Chen, J. S.; Dent, A. J.; Marchese, L. On the Nature of the Active-Site in a CoAPO-18 Solid Acid Catalyst. *Angew. Chem.-Int. Edit.* **1994**, *33*(18), 1871-1873.

[14] Hartmann, M.; Kevan, L. Transition-Metal Ions in Aluminophosphate and Silicoaluminophosphate Molecular Sieves: Location, Interaction with Adsorbates and Catalytic Properties. *Chem. Rev.* **1999**, *99*(3), 635-663.

[15] Pastore, H. O.; Coluccia, S.; Marchese, L. Porous Aluminophosphates: From Molecular Sieves to Designed Acid Catalysts. *Annu. Rev. Mater. Res.* **2005**, *35*, 351-395.

[16] Gorte, R. J. What do We Know About the Acidity of Solid Acids? *Catal. Lett.* **1999**, *62*(1), 1-13.

[17] Chen, J. S.; Sankar, G.; Thomas, J. M.; Xu, R. R.; Greaves, G. N.; Waller, D. Cobalt-Substituted Aluminophosphate Molecular-Sieves - X-Ray Absorption, Infrared Spectroscopic, and Catalytic Studies. *Chem. Mat.* **1992**, *4*(6), 1373-1379.

[18] Fan, W. B.; Li, R. F.; Dou, T.; Tatsumi, T.; Weckhuysen, B. M. Solvent Effects in the Synthesis of CoAPO-5,-11 and-34 Molecular Sieves. *Micropor. Mesopor. Mat.* **2005**, *84*(1-3), 116-126.

[19] Fan, W. B.; Schoonheydt, R. A.; Weckhuysen, B. M. Synthesis of Co-Rich CoAPO-CHA Molecular Sieves in the Presence of Ethanol and Caesium. *Chem. Commun.* **2000**, (22), 2249-2250.

[20] Batista, J.; Kaucic, V.; Rajic, N.; Stojakovic, D. On the Formation of CoAPSO-44. *Zeolites* **1992**, *12*(8), 925-928.

[21] Hill, S. J.; Williams, C. D.; Duke, C. V. A. The Synthesis of High Cobalt-Containing CoAPO-34. *Zeolites* **1996**, *17*(3), 291-296.

[22] Canesson, L.; Tuel, A. Synthesis and Characterization of CoAPO(4)-39 Molecular Sieves. *Zeolites* **1997**, *18*(4), 260-268.

[23] Yokomori, Y.; Kawachi, Y. Synthesis of Large Single-Crystals of CoAPO-5 Molecular-Sieves. *Zeolites* **1995**, *15*(7), 637-639.

[24] Duke, C. V. A.; Hill, S. J.; Williams, C. D. Synthesis of MnAPO-20 and CoAPO-20 Using Tetrahedral Metal Species. *J. Chem. Soc. Chem. Comm.* **1994**, (22), 2633-2633.

[25] Singh, P. S.; Shaikh, R. A.; Bandyopadhyay, R.; Rao, B. S. Synthesis of CoVPI-5 with Bifunctional Catalytic Activity. *J. Chem. Soc. Chem. Comm.* **1995**, (22), 2255-2256.

[26] Ahn, S.; Chon, H. The Influence of Metal Ions on the Synthesis of MeAPO-5 (Me=Co, Mg) in the Presence of Acetate Ions. *Micropor. Mater.* **1997**, *8*(3-4), 113-121.

[27] Meusinger, J.; Vinek, H.; Lercher, J. A. Cracking of N-Hexane and N-Butane over SAPO-5, MgAPO-5 and CoAPO-5. *J. Mol. Catal.* **1994**, *87*(2-3), 263-274.

[28] Marchese, L.; Chen, J. S.; Thomas, J. M.; Coluccia, S.; Zecchina, A. Bronsted, Lewis, and Redox Centers on CoAPO-18 Catalysts: 1. Vibrational-Modes of Adsorbed Water. *J. Phys. Chem.* **1994**, *98*(50), 13350-13356.

[29] Montes, C.; Davis, M. E.; Murray, B.; Narayana, M. Isolated Redox Centers within Microporous Environments: 1. Cobalt-Containing Aluminophosphate Molecular-Sieve 5. *J. Phys. Chem.* **1990**, *94*(16), 6425-6430.

[30] Prakash, A. M.; Hartmann, M.; Kevan, L. Synthesis, Characterization, and Adsorbate Interactions of CoAPO-41 and CoAPSO-41 Molecular Sieves. *J. Phys. Chem. B* **1997**, *101*(35), 6819-6826.

[31] Zhang, G. A.; Harris, T. V. X-Ray-Absorption Studies of Cobalt Aluminophosphate Zeolites (CoAPO-5). *Physica B* **1995**, *209*(1-4), 697-698.

[32] Akolekar, D. B. Investigations on the CoAPO-36 Molecular-Sieve. *Catal. Lett.* **1994**, *28*(2-4), 249-262.

[33] Perot, G. Hydrotreating Catalysts Containing Zeolites and Related Materials: Mechanistic Aspects Related to Deep Desulfurization. *Catal. Today* **2003**, *86*(1-4), 111-128.

[34] Salem, A. B. S. H. Naphtha Desulfurization by Adsorption. *Ind. Eng. Chem. Res.* **1994**, *33*(2), 336-340.

[35] Wood, D. L.; Remeika, J. P. Optical Adsorption of Tetrahedra; Co^{3+} and Co^{2+} in Garnets. *J. Chem. Phys.* **1967**, *46*(9), 3595-3602.

[36] Sponer, J.; Cejka, J.; Dedecek, J.; Wichterlova, B. Coordination and Properties of Cobalt in the Molecular Sieves CoAPO-5 and-11. *Micropor. Mesopor. Mat.* **2000**, *37*(1-2), 117-127.

[37] Borges, C.; Ribeiro, M. F.; Henriques, C.; Lourenco, J. P.; Murphy, D. M.; Louati, A.; Gabelica, Z. Structural State and Redox Behavior of Framework Co(II) in CoIST-2: A Novel Cobalt-Substituted Aluminophosphate with AEN Topology. *J. Phys. Chem. B* **2004**, *108*(24), 8344-8354.

[38] Tusar, N. N.; Mali, G.; Arcon, I.; Kaucic, V.; Ghanbari-Siahkali, A.; Dwyer, J. Framework Cobalt and Manganese in MeAPO-31 (Me = Co, Mn) Molecular Sieves. *Micropor. Mesopor. Mat.* **2002**, *55*(2), 203-216.

[39] Verberckmoes, A. A.; Uytterhoeven, M. G.; Schoonheydt, R. A. Framework and Extra-Framework Co^{2+} in CoAPO-5 by Diffuse Reflectance Spectroscopy. *Zeolites* **1997**, *19*(2-3), 180-189.

[40] Berndt, H.; Martin, A.; Zhang, Y. Study on the Nature and the Redox Properties of Cobalt Species Located in CoAPO Molecular Sieves. *Micropor. Mater.* **1996**, *6*(1), 1-12.

[41] Bennett, J. M.; Marcus, B. K., The Crystal Structures of Several Metal Aluminophosphate Molecular Sieves. In *Innovation in Zeolite Materials Science (Stud. Surf. Sci. Catal.)*, Grobet, P. J.; Mortier, W. J.; Vansant, E. F.; Shultz-Ekloff, G., Eds. Elsevier Science Publishers B. V.: Amsterdam, 1988; Vol. 37, p 269.

[42] Feng, P. Synthesis and Characterization of Transition Metal Phosphate-Based Novel Framework Materials. Doctoral Dissertation, University of California, Santa Barbara, 1998.

[43] Bu, X. H.; Feng, P. Y.; Stucky, G. D. Large-Cage Zeolite Structures with Multidimensional 12-Ring Channels. *Science* **1997**, *278*(5346), 2080-2085.

[44] Breck, D. W. *Zeolite Molecular Sieves*. Wiley: New York, 1973.

[45] Liu, S. B.; Ma, L. J.; Lin, M. W.; Wu, J. F.; Chen, T. L. NMR Investigation of the Distribution of Benzene in NaX and NaY Zeolites: Influence of Cation Location and Adsorbate Concentration. *J. Phys. Chem.* **1992**, *96*(20), 8120-8125.

[46] Yang, R. T. *Gas Separation by Adsorption Processes*. Imperial College Press: River Edge, N.J., 1997; Vol. 1.

[47] Do, D. D. *Adsorption Analysis: Equilibria and Kinetics*. Imperial College Press: London, 1998.

[48] Redhead, P. A. Thermal Desorption of Gases. *Vacuum* **1962**, *12*(4), 203-211.

[49] Parrillo, D. J.; Gorte, R. J. Characterization of Acidity in H-ZSM-5, H-ZSM-12, H-Mordenite, and H-Y Using Microcalorimetry. *J. Phys. Chem.* **1993**, *97*(34), 8786-8792.

[50] Tomkova, E. TDS Spectra Analysis. *Surf. Sci.* **1996**, *351*(1-3), 309-318.

[51] Fesenko, E. A.; Barnes, P. A.; Parkes, G. M. B.; Brown, D. R.; Naderi, M. A New Approach to the Study of the Reactivity of Solid-Acid Catalysts: The Application of Constant Rate Thermal Analysis to the Desorption and Surface Reaction of Isopropylamine from NaY and HY Zeolites. *J. Phys. Chem. B* **2001**, *105*(26), 6178-6185.

[52] Hernandez-Maldonado, A. J.; Yang, R. T.; Chinn, D.; Munson, C. L. Partially Calcined Gismondine Type Silicoaluminophosphate SAPO-43: Isopropylamine Elimination and Separation of Carbon Dioxide, Hydrogen Sulfide, and Water. *Langmuir* **2003**, *19*(6), 2193-2200.

[53] Foresman, J. B.; Frisch, *Æ. Exploring Chemistry with Electronic Structure Methods.* 2nd ed.; Gaussian, Inc.: Pittsburgh, PA 1996; p 296.

[54] Baerlocher, C.; McCusker, L. B., Database of Zeolite Structures. In International Zeolite Association Synthesis Commission: 2007.

[55] Thomson, S.; Luca, V.; Howe, R. Framework Co(II) in CoAPO-5. *Phys. Chem. Chem. Phys.* **1999**, *1*(4), 615-619.

[56] Fan, W. B.; Schoonheydt, R. A.; Weckhuysen, B. M. Hydrothermal Synthesis of Co-Rich CoAPO-5 Molecular Sieves. *Phys. Chem. Chem. Phys.* **2001**, *3*(15), 3240-3246.

[57] Arieli, D.; Prisner, T. F.; Hertel, M.; Goldfarb, D. Resolving Mn Framework Sites in Large Cage Aluminophosphate Zeotypes by High Field EPR and ENDOR Spectroscopy. *Phys. Chem. Chem. Phys.* **2004**, *6*(1), 172-181.

[58] Mali, G.; Meden, A.; Ristic, A.; Tusar, N. N.; Kaucic, V. Interaction of Dipropylamine Template Molecules with the Framework of as-Synthesized $AlPO_4$-31. *J. Phys. Chem. B* **2002**, *106*(1), 63-69.

[59] Lazaro, F. J.; Lopez, A.; Larrea, A.; Pankhurst, Q. A.; Nieto, J. M. L.; Corma, A. Paramagnetic-Superparamagnetic Transition in Molecular-Sieve-Supported Antiferromagnetic Particles. *IEEE T. Magn.* **1998**, *34*(4), 1030-1032.

[60] Lopez, A.; Lazaro, F. J.; Garcia-Palacios, J. L.; Larrea, A.; Pankhurst, Q. A.; Martinez, C.; Corma, A. Superparamagnetic Particles in ZSM-5-Type Ferrisilicates. *J. Mater. Res.* **1997**, *12*(6), 1519-1529.

[61] Cheng, L. S.; Yang, R. T. Improved Horvath-Kawazoe Equations Including Spherical Pore Models for Calculating Micropore Size Distribution. *Chem. Eng. Sci.* **1994**, *49*(16), 2599-2609.

[62] Rege, S. U.; Yang, R. T. Corrected Horvath-Kawazoe Equations for Pore-Size Distribution. *AIChE J.* **2000**, *46*(4), 734-750.

[63] Martucci, A.; Alberti, A.; Cruciani, G.; Frache, A.; Marchese, L.; Pastore, H. O. Temperature-Induced Transformations in CoAPO-34 Molecular Sieve: A Combined in Situ X-ray Diffraction and FTIR Study. *J. Phys. Chem. B* **2005**, *109*(28), 13483-13492.

[64] Lohse, U.; Bertram, R.; Jancke, K.; Kurzawski, I.; Parlitz, B.; Loffler, E.; Schreier, E. Acidity of Aluminophosphate Structures: 2. Incorporation of Cobalt into CHA and AFI by Microwave Synthesis. *J. Chem. Soc. Faraday T.* **1995**, *91*(7), 1163-1172.

[65] Yue, M. B.; Chun, Y.; Cao, Y.; Dong, X.; Zhu, J. H. CO_2 Capture by As-Prepared SBA-15 with an Occluded Organic Template. *Adv. Funct. Mater.* **2006**, *16*(13), 1717-1722.

[66] Kurshev, V.; Kevan, L.; Parillo, D. J.; Pereira, C.; Kokotailo, G. T.; Gorte, R. J. An Investigation of Framework Substitution of Cobalt into Aluminophosphate-5 Using Electron-Spin-Resonance and Temperature-Programmed Desorption Measurements. *J. Phys. Chem.* **1994**, *98*(40), 10160-10166.

[67] Ashtekar, S.; Barrie, P. J.; Hargreaves, M.; Gladden, L. F. An FT-Raman Study of the Template-Framework Interaction in $AlPO_4$-Based Molecular Sieve *Angew. Chem.-Int. Edit.* **1997**, *36*, 876-878.

[68] Holmes, A. J.; Kirkby, S. J.; Ozin, G. A.; Young, D. Raman Spectra of the Unidimensional Aluminophosphate Molecular Sieves AlPO4-11, AlPO4-5, AlPO4-8, and VPI-5. *J. Phys. Chem.* **1994**, *98*(17), 4677-4682.

[69] Dutta, P. K.; Mohana Rao, K.; Park, J. Y. Correlation of Raman Spectra of Zeolites with Framework Architecture. *J. Phys. Chem.* **1991**, *95*(17), 6654-6656.

[70] Dutta, P. K.; Shieh, D. C.; Puri, M. Correlation of Framework Raman Bands of Zeolites with Structure. *Zeolites* **1988**, *8*(4), 306-309.

[71] Wu, C.; Chao, K.; Chang, H.; Lee, L.; Naccache, C. Study of Oxygen-Binding Cobalt Species on CoAPO-11 Molecular Sieve Under Redox Treatment. *J. Chem. Soc. Faraday T.* **1999**, *93*(19), 3551-3553.

[72] Akolekar, D. B.; Bhargava, S.; van Bronswijk, W. Fourier Transform Raman Spectroscopy of Novel Aluminophosphate Molecular Sieves. *Appl. Spectrosc.* **1999**, *53*(8), 931-937.

[73] Pichat, P.; Beaumont, R.; Barthomeuf, D. Infra-red Structural Study of Aluminium-deficient Y Zeolites. *J. Chem. Soc. Faraday Trans.* **1974**, *70*, 1402-1407.

[74] Jacobs, W. P. J. H.; van Wolput, J. H. M. C.; van Santen, R. A. Fourier-Transform Infrared Study of the Protonation of the Zeolitic Lattice Influence of Silicon : Aluminium Ratio and Structure. *J. Chem. Soc. Faraday Trans.* **1993**, *89*(8), 1271-1276.

[75] Chao, K. J.; Sheu, S. P.; Sheut, H. S. Structure and Chemistry of Cobalt in CoAPO-5 Molecular Sieve. *J. Chem. Soc. Faraday Trans.* **1992**, *88*(19), 2949-2954.

[76] Janchen, J.; Peeters, M. P. J.; van Wolput, J. H. M. C.; Wolthuizen, J. P.; van Hooff, J. H. C.; Lohse, U. CoAPO Molecular Sieve Acidity investigated by Adsorption Calorimetry and IR Spectroscopy. *J. Chem. Soc. Faraday Trans.* **1994**, *90*(7), 1033-1039.

[77] Miecznikowski, A.; Hanuza, J. Application of the Long Chain Approach to the Structure and Vibrational Spectra of X and Y Zeolites. *Zeolites* **1985**, *5*, 188-193.

[78] Mayo, D. W.; Miller, F. A.; Hannah, R. W. *Course Notes on the Interpretation of Infrared and Raman Spectra*. John Wiley & Sons, Inc.: Hoboken, New Jersey, 2004; p 567.

[79] Feng, P. Y. Synthesis and Characterization of Transition Metal Phosphate-Based Novel Framework Materials. Doctoral Dissertation, University of California, Santa Barbara, 1998.

[80] Nicholas, J. B. Density Functional Theory Studies of Zeolite Structure, Acidity, and Reactivity. *Top. Catal.* **1997**, *4*, 157-171.

CHAPTER 3

SBE-TYPE METAL-SUBSTITUTED ALUMINOPHOSPHATES: DETEMPLATION AND COORDINATION CHEMISTRY

3.1 Introduction

Incorporation of transition-metal ions into aluminophosphate (AlPO-*n*) molecular sieves frameworks provides specific properties that could produce potential materials candidates for both catalytic and adsorption applications.[1, 2] Metal aluminophosphates (MeAPOs) are of particular interest for the design of new materials functional for a series of heterogeneously catalyzed reactions in environmental catalysis[1, 3, 4] such as oxidation of NO_x and CO, and acid-catalyzed reactions such as methanol-to-olefins.[5] The isomorphic substitution of AlPO-*n* framework atoms with metals (e.g., Me = Co, Mn, Fe, Ti, Cr) generates negative charge sites in the framework that must be compensated with positive charges from other species.[6, 7] These at the same time could act as effective catalytic or adsorption sites, rendering different functionalization states within the same porous framework. For instance, the replacement of Al^{3+} with divalent metals, besides enhancing Brønsted acidity levels, brings about the interesting solid oxidation properties for redox[1, 3, 7-23] and hydrodesulfurization[24] applications, oxidative dehydrogenation of hydrocarbons[25-27] and isomerizations,[28] among others. In addition to transition metals, many structures in the AlPO-*n* family incorporate in structure alkaline earth metals such as magnesium, that can be used for purification of raw

materials for the manufacture of pharmaceuticals[29] (e.g., separation of *p*-xylene), and due to the high Brønsted acidity, for the catalytic cracking of alkanes.[30-35] In comparison to CoAPOs or MnAPOs, Mg^{2+} atoms incorporated in aluminophosphates cannot increase its oxidation state, which could become often a limiting factor in catalytic activity.

During the late 1990s, Stucky and co-workers reported the synthesis of more than a dozen porous zeolitic-type structures with large cages and a Me/Al ratio close to unity.[36, 37] Among them, the SBE-type materials (Figure 3.1), promise unique properties for adsorption and catalysis applications, the potential could only be achieved after removal of the SDA while preserving the framework integrity. In other words, maintaining the material microporosity via detemplation.

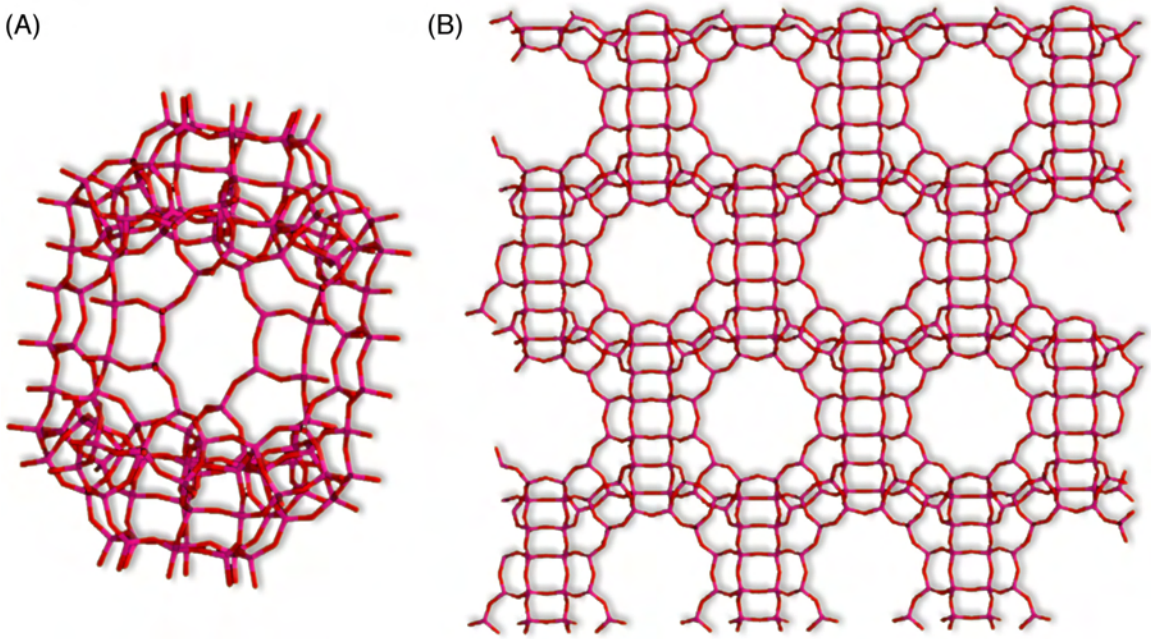

Figure 3.1. SBE framework (A) unit-cell/supercage and (B) view along ***a*** or ***b***.

In the work presented in Chapter 2, the Co-SBE variant synthesis procedure was systematically studied and optimized, and several characterization techniques were used to gather information about the material's framework properties.[38] Single-phase powder crystals of SBE-type cobalt aluminophosphates were produced by extending aging times and decreasing the crystallization temperature during the synthesis. While XRD data confirmed the presence of a rich Co-SBE phase, SEM images showed a hexagonal plate-like crystal growth, in contrast to the corner-truncated square plates which were previously reported during single crystal studies.[36, 37] Such differences in morphology could be attributed to variations in aging procedures, which are well known to influence the particle growth and dispersity.[39-41] Parameters such as pH value, concentration and temperature can affect crystal morphology also,[42] but those variable effects were not considered. Post-synthesis treatments to study the removal of the SDA indicated that exposure to an oxidative atmosphere resulted in a "non-porous" framework. Conversely, a vacuum treated material exhibited a surface area and an average pore diameter of ca. 320 m^2/g and 9 Å, respectively.[38]

The current chapter encompasses the extension of the cobalt-rich SBE synthesis procedure and characterization previously reported (Chapter 2) by our group[38] to the Mg- and Mn-SBE variants to further understand the detemplation process in the particular framework. After detailed studies, the optimum conditions for the template removal were determined via gravimetric (TGA), *in situ* high temperature XRD and simultaneous X-Ray Diffraction and Differential Scanning Calorimetry (XRD-DSC). Several spectroscopic techniques (e.g., UV-

vis, XPS, EPR, NMR) were employed to demonstrate the substitution of the metal ions and to elucidate the chemical environment of the metal atoms. Water vapor adsorption on the detemplated Mg-SBE was investigated to evaluate the material hydrophilicity.

3.2 Experimental Section

3.2.1 SBE Synthesis Procedure

Co-SBE was prepared following the method previously reported in Chapter 2.[38] Mg-SBE and Mn-SBE were synthesized hydrothermally following the characteristic synthesis procedure described elsewhere.[36-38] Aging time for solution *A*, containing aluminum isopropoxide (AIP), *o*-phosphoric acid and ethylene glycol, was extended to one week. Solution *B* was prepared using the preferred metal (Me = Mn or Co) carbonate or magnesium hydrogen phosphate for the magnesium containing material (Me = Mg), *o*-phosphoric acid and deionized water. The solutions *A* and *B* were mixed together and stirred at room temperature for approximately 20 minutes until a homogeneous phase was formed (pH ~ 3). 1,9-diaminononane (DAN) was slowly added under constant stirring for up to 20 minutes. At the pH level of the mixture, DAN molecules are believed to be protonated and the templating process starts. Dipropylamine (DPA), the co-solvent, was added dropwise until the measured pH of the final solution was around 7.8. A typical gel composition was $0.5C_9H_{24}N_2$:$2.5C_6H_{16}NO$:MeO (Me = Co, Mn, or Mg) : $0.5Al_2O_3$: P_2O_5 : 50 H_2O. Crystallization of the gel was carried out in 45 mL Teflon-lined stainless-steel autoclaves (Parr Instruments Co., Moline, IL) at temperatures up to 443 K for 168 hours. SBE powder crystals were filtered, thoroughly washed with deionized water and ethanol, and dried in a

forced-convection oven at 363 K overnight.

3.2.2 Standard Powder X-Ray Diffraction and Scanning Electron Microscopy

As-synthesized samples were characterized by X-ray Diffraction (XRD) and Scanning Electron Microscopy (SEM) for determination of phase purity and morphology, respectively. XRD analyses were performed using a Rigaku ULTIMA III X-ray Diffraction unit equipped with cross beam optics and a CuK_{α} target operating at 40 *k*V and 44 *m*A. The diffraction angle *(2θ)* range was set to 2-60°. The step size and speed (step scan) were 0.04° and 2°/min, respectively. SEM images were obtained using a JEOL JSM-6390 instrument. The morphologies of SBE samples were captured using a SEI detector and an accelerating voltage of 10.0 *k*V. Samples were sputter-coated with gold using a Denton Vacuum Desk IV (Denton Vacuum, LLC) unit to improve secondary electron emission and prevent charging.

3.2.3 Energy Dispersive X-Ray Analysis

Metal composition was determined by using the aforementioned SEM unit and an EDAX Energy Dispersive X-Ray (EDX) spectrometer. Surface composition was analyzed using the ZAF Algorithm by means of standard-less quantification. The surface elements identified include P, Al, Co, Mg, and Mn as expected. The EDX area scan mode analysis was performed at 10 *k*V with a beam current of 102.6 μA. In order to ensure that the data

collected were representative of the bulk sample, scans were performed to at least four different randomly selected spots and the average was reported.

3.2.4 Transmission Electron Microscopy

SBE samples for Transmission Electron Microscopy (TEM) were prepared by grinding the powder, and then, transferring it to a copper grid. Finally, the excess of material was removed by shaking the grid with tweezers. The TEM analysis was carried out using a Tecnai G2 F30 field-emission gun transmission electron microscope (FEI Company, Oregon, USA) equipped with a charge couple device (CCD) and operated at an accelerating voltage of 300 *k*V. TEM digital images were processed and examined by performing Fast Fourier Transform (FFT) analysis with commercial image analysis software (Digital Micrograph, Gatan, USA).

3.2.5 Detemplation, Porosimetry and Thermal Gravimetric Analyses

A Micromeritics ASAP 2020 instrument was used for activation of as-synthesized samples (i.e., detemplation) and acquisition of porosimetry data. The former was accomplished using the sample activation module while the latter was gathered using the static volumetric adsorption setup of the instrument. Porosimetry tests were performed using adsorption of nitrogen at 77 K. Samples were degassed *in situ* in a two-stage process prior to each measurement. It should be mentioned that the degassing or activation ports vapor exhausts were isolated from the vacuum pumps by means of condensing traps. The evacuation stage

was run at a heating rate of 5 K/min using a vacuum rate that ranged from 10 mm Hg/s to 50 mm Hg/s for 5 h. Similar heating rates were employed for the formal heating stage (i.e., detemplation), with final soaking temperatures that ranged from 623 K to 723 K and sustained for 18 h. The specific surface area was determined according to the Langmuir approach in the relative pressure (P/P_o) range of 0.01–0.20.[43]

Thermal gravimetric analysis (TGA) was performed using a TA-Q500 microbalance, while varying the heating rate from 10 K/min to 30 K/min over a temperature range from ambient to 1,173 K and using a constant flow of helium or air (both ultra high purity grade, Praxair) at 60 mL/min. All gases were pre-treated using pre-sorbers (i.e., 3A Zeolites and hydrocarbon traps) to remove any traces of water and other contaminants. The gravimetric tests were conducted to investigate the thermal behavior of the samples and to determine the peak temperature of degradation/elimination of the structure-directing agent. Apparent activation energy for desorption of the SDA was estimated using the second region of the TG profile for a first-order kinetics reaction and the Redhead's approach (Equation 3.1): [44-48]

$$\frac{E_a}{RT_m^2} = \frac{A}{\beta}\exp\left(-\frac{E_a}{RT_m}\right) \qquad (3.1)$$

where T_m is the temperature at peak maximum (K), A is a pre-exponential factor, β is the heating rate (K/min), and E_a is the apparent activation energy for desorption. T_m was determined from the differential TG (DTG) profile.

3.2.6 *In situ* High Temperature and Differential Scanning Calorimetry X-Ray Diffraction

In situ high-temperature X-ray diffraction measurements were performed using a Rigaku ReactorX (Rigaku, Japan) module equipped with a continuous beryllium window. This module was attached to the Rigaku ULTIMA III X-ray Diffraction equipment (CuK_{α}) goniometer previously mentioned. After careful parallel beam type calibration, measurements were performed on as-synthesized powder samples from room temperature to 1,173 K in either air or helium atmospheres by means of infrared heating. This technique enables precise and rapid heating/cooling of the samples. A temperature ramp of 5 K/min and a gas flow of 60 mL/min were used. *In situ* powder diffraction analyses were carried out at 40 *kV* and 44 *mA*, with a diffraction angle *(2θ)* range from 2 to 60° and a scan speed of 8°/min.

Simultaneous X-ray diffraction and differential scanning calorimetry (XRD-DSC) measurements were performed using an XRD-DSC II heat-flow type module (Rigaku, Japan) equipped with aluminum windows. A small amount of as-synthesized samples (less than 10 mg) were heated from room temperature to 613 K at 5 K/min and purged in either air or helium at a rate of 60 mL/min. The final temperature was held for one hour to allow extended crystallographic data acquisition. The maximum temperature and the *2θ* scanning range for the XRD-DSC II module are 623 K and 5-40º, respectively, due to the chamber windows configuration and materials. The DSC temperature and heat-flow signals were calibrated with

standards of neat indium, tin and lead, respectively, using the same heating rate. CuK_{α} radiation was generated at 40 *k*V and 44 *m*A using a 2θ range from 5 to 40º and a scan speed of 5°/min. An aluminum disk was used as a reference material during DSC measurements.

3.2.7 FT-IR, UV-*vis* and X-Ray Photoelectron Spectroscopy

FT-IR in the attenuated total reflection (ATR) absorbance spectra were recorded on the as-synthesized and pre-treated samples in vacuum and at variable temperatures using a Varian 800 FT-IR SCIMITAR series spectrometer. The spectral resolution was 4 cm^{-1} and signal averaging was performed for 100 scans/sample. Samples were degassed at 423 K prior to analysis and scanned in an out-of-compartment horizontal ATR accessory (PIKE MIRacle™ Single Reflection ZnSe HATR) for a range of 4000-600 cm^{-1}.

UV-*vis* absorption spectra were collected at room temperature using a Varian Cary 500 Scan UV-*vis* spectrometer in a single-beam mode. Samples were dehydrated prior to measurements to remove all adsorbed water and prepared in the form of KBr pellets. To confirm the absence of absorption bands in the region measured, a background spectrum of KBr pellets was recorded.

X-Ray Photoelectron Spectroscopy (XPS) spectra were recorded using a Perkin Elmer PHI 5600ci ESCA system, employing an Al-Kα polychromatic source (1486.6 eV, 350 W, 15 *k*V). The takeoff angle was 45º. Wide scan survey and multiplex spectra were obtained with pass energies of 187.85 eV and 58.70 eV, respectively for the electron energy analyzer. The

working pressure was lower than 10^{-9} Pa. All the binding energies reported were corrected utilizing the XPS signal of the carbon contamination peak (C_{1s}) at 284.5 eV of an internal standard. Extended spectra (survey) were collected in the range 0 -1200 eV (1 eV step, 1.6 s $step^{-1}$). Detailed spectra were recorded for the following regions: Al_{2p}, N_{1s}, C_{1s}, Co_{2p}, P_{2p} and O_{1s}, (1 eV step, 0.25 s $step^{-1}$).

3.2.8 Electron Paramagnetic Resonance Spectroscopy

EPR spectra of Mg- and Mn-SBE samples were recorded on a Bruker EMX Electron Paramagnetic Resonance (EPR) spectrometer operating at X-band frequencies of 9.4 GHz and a microwave power of 0.6 mW or lower. Powder samples were loaded into quartz capillary tubes (0.7 mm in diameter) and later inserted into 4 mm quartz EPR tube for measurements at an ambient condition. Variable temperature (VT) EPR measurements were performed for the Co-SBE sample for a temperature range between 4 K and 290 K. For the VT experiment it was necessary to remove oxygen molecules from the Co-SBE powder samples by evacuation. The final pressure of 10^{-2} mm Hg was maintained throughout the VT EPR measurements.

3.2.9 Solid-State Magic Angle Spinning-Nuclear Magnetic Resonance

Solid-State Magic Angle Spinning-Nuclear Magnetic Resonance (MAS NMR) measurements were performed at room temperature using a Bruker Advanced 500 MHz spectrometer equipped with a Bruker 4 mm MAS probe. Spectral frequencies were 500.23 MHz, 202.50, 130.35, 125.79 MHz for the ^{1}H, ^{31}P, ^{27}Al, and ^{13}C nuclei, respectively. Samples were loaded

into 4 mm ZrO_2 rotors at ambient conditions and spun at speeds of 11-13 kHz. Typical one-dimensional (1-D) ^{1}H, ^{31}P, and ^{13}C MAS NMR spectra were acquired after a single 4 μs-90^{o} pulse. A short pulse (i.e., < $\pi/18$) was used for ^{27}Al nucleus for uniform excitation and quantification purpose. The NMR shifts were reported in parts per million (ppm) and calibrated with respect to standard external references (e.g. tetramethylsilane (TMS) for ^{1}H and ^{13}C, 1.0M aqueous solution of aluminum nitrate for ^{27}Al, and neat *o*-phosphoric acid for ^{31}P nuclei).

3.2.10 Water Adsorption Isotherms

In order to evaluate the general hydrophobic/hydrophilic characteristics of the material exhibiting the highest porosity, water sorption analyses were executed using a fully automated Intelligent Gravimetric Analyzer (IGA). These analyses were supplied by Hiden Analytical, Ltd. (Warrington, United Kingdom). Prior to adsorption testing, the samples were degassed in vacuum for 6 h at 373 K using an evacuation rate of 10 mm Hg/s and heated up to 648 K at a heating rate of 5 K/min for 18 h. Following the degassing step samples were analyzed at 298 K. Vapor pressure was increased using pressure intervals in the range of P/P_0 values up to 0.99 to obtain the water vapor isotherms. Water vapor uptake was measured as a function of time until system reached equilibrium at a specific pressure step.

Frequently, kinetic data for the adsorption process are correlated in terms of a diffusion time constant (D/L^2), where D and L are the diffusion constant and the characteristic length, respectively.[49, 50] The diffusion time constant was estimated by fitting fractional uptake (F)

data with the theoretical curve derived from a phenomenological model that depends on the crystal geometry. For a slab-shape solid particle the model is given by equation 3.2:[50]

$$F = \frac{m_t}{m_\infty} = 1 - \frac{2}{\pi^2}\sum_{n=1}^{\infty}\frac{1}{(n-1/2)^2}\exp\left(-(n-1/2)^2\pi^2\frac{Dt}{L^2}\right) \qquad (3.2)$$

where m_t is the uptake at any time t and m_∞ is the uptake as t approaches infinity.

3.3 Results and Discussion

3.3.1 Syntheses, X-Ray Diffraction and Scanning Electron Microscopy

Optimized synthesis conditions for the preparation of powder crystals of SBE containing magnesium and manganese were successfully attained by decreasing the reaction temperature to 443 K and increasing aging time.[36-38] One should note that for the case of Mg-SBE the preparation of solution *B* required less amount of *o*-phosphoric acid due to the presence of phosphate already in the magnesium source reagent. DAN was used as the SDA and DPA, the co-solvent, was added to facilitate the increase of the solubility of *protonated* DANs to the required levels for hydrothermal templating. Comparison of our powder X-ray diffraction experimental results (see Figure 3.2) to the single crystal diffraction data reported by Stucky and co-workers,[36, 37] and to the simulated pattern of SBE reported by the International Zeolite Association (IZA),[51] confirmed the presence of a highly crystalline phase for Co-, Mg- and Mn-SBE metal-substituted aluminophosphates. The observed differences in intensity ratios are probably due to preferential orientation of the powder crystals.

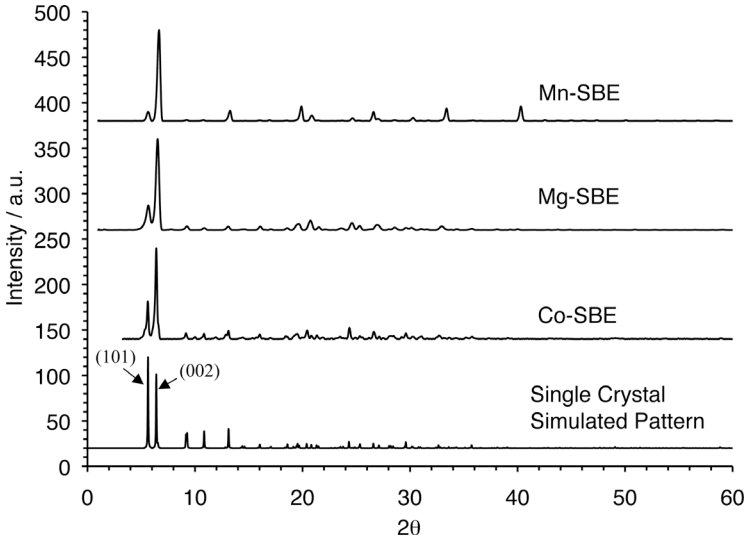

Figure 3.2. Powder XRD patterns for as-synthesized SBE (Co, Mn and Mg) samples. Plane (101) stretches out along ***b*** and (002) along ***a*** or ***b***. The simulated XRD pattern for SBE was obtained using the single-crystal data from IZA database.[51]

In terms of appearance, the as-synthesized Co-SBE samples have an intense blue color, which is characteristic of a high concentration of divalent cobalt in a tetrahedral environment.[5, 8, 52-55] A semi-quantitative EDX analysis previously reported by Belén-Cordero and Hernández-Maldonado confirmed the high cobalt framework content in as-synthesized Co-SBE.[38] A summary of the metal compositional analysis for the samples tested is shown in Table 3.1. In general, EDX analysis for all the SBE variants showed highly metal-substituted aluminophosphates (i.e., Me/Al ~ 1.0). Surface morphology for all the SBE variants crystals was studied by means of SEM. Co-SBE exhibits hexagonal-plate morphology with a crystal size of ca. 100 μm (Figure 3.3). This is in well agreement with our previous report.[38]

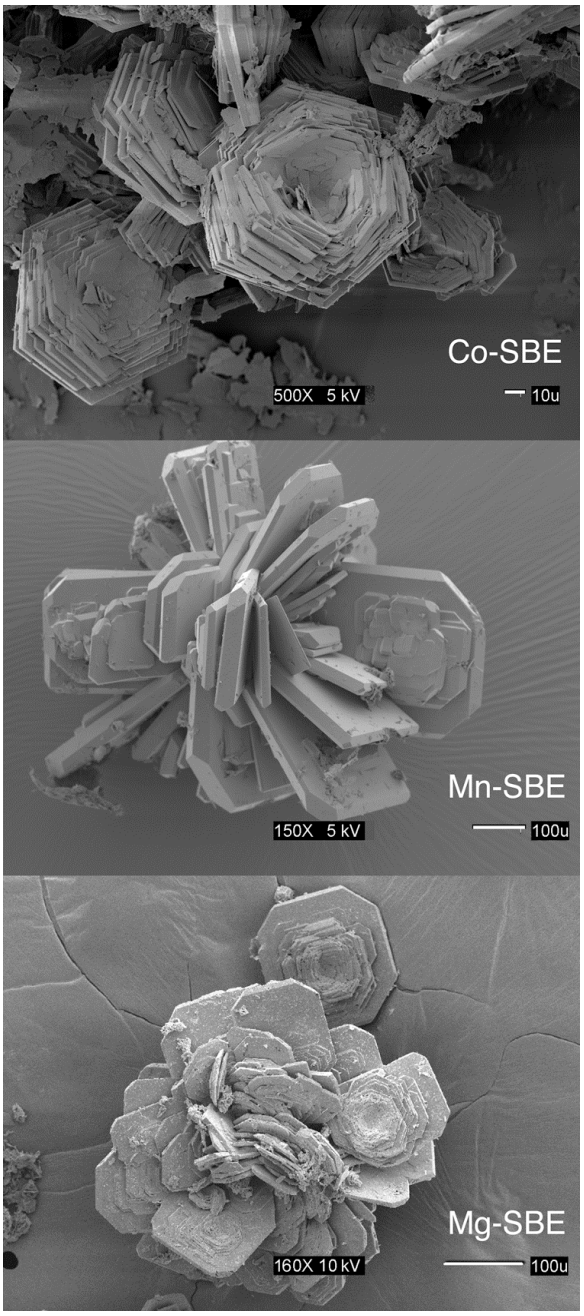

Figure 3.3. SEM micrographs for as-synthesized Co-, Mn- and Mg-SBE samples.

Pitting of the as-synthesized Co-SBE crystals could be attributed to the mild instability of aluminophosphates in their mother liquor.[56] In contrast, Mn-SBE and Mg-SBE

synthesis resulted in the blooming of aggregated crystals displaying square plates with truncated corners, and around 100 μm in size and exhibiting a higher packing density when compared to Co-SBE. Mg- and Mn-SBE crystals possess the same morphological appearance observed by Bu et al.[36, 37]

Table 3.1. Framework molar metal (Me = Co, Mn, or Mg) ratios for as-synthesized SBE-type aluminophosphates. Data obtained from surface composition EDX analysis.

Sample	Me/P**	Me/P	Al/P*	Al/P	(Me+Al)/P
Co-SBE	-----	0.59	-----	0.56	1.16
Mn-SBE	0.41	0.48	0.57	0.71	1.19
Mg-SBE	0.43	0.50	0.59	0.55	1.06

3.3.2 Transmission Electron Microscopy

The porous structure of the Mn-SBE was elucidated by Transmission Electron Microscopy (TEM). SBE-type MeAPOs are highly crystalline materials but also very sensitive to the electron beam and made the high-resolution imaging challenging. Mn-SBE appeared to be the least beam sensitive and the difference in morphology is apparent from TEM images. Broken crystals appeared to be single-crystalline. Figure 3.4 shows typical TEM micrographs of Mn-SBE samples. The picture in the right was obtained from the FFT analysis performed on digitally acquired TEM images. Figure 3.5 exhibits a highly oriented structure of Mn-SBE in the inverse FFT spectrum, which arrangement corresponds exactly with the position

**Experimental values of metal ratios for as-synthesized SBS- and SBE-type metal aluminophosphates as reported by Stucky and coworkers from EDX analysis.

of the pores in the unit cell structure along the *b*-axis. The image in Figure 3.5 indicates that the pores are ordered and exhibit regular pore diameters of approximately 7.1 Å.

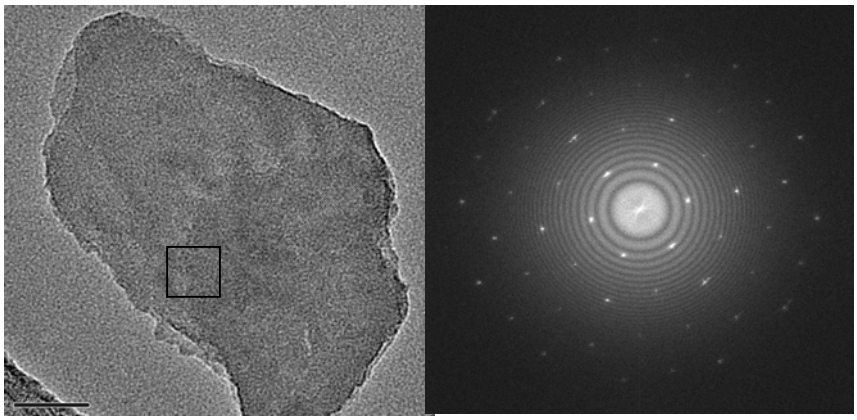

Figure 3.4. TEM digital image of an Mn-SBE crystal (left) and FFT spectrum (right).

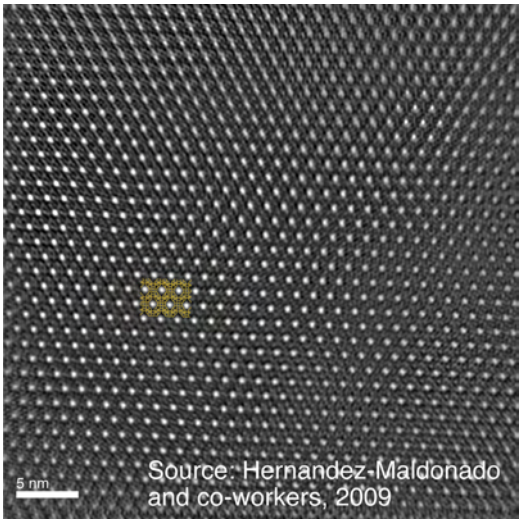

Figure 3.5. High-resolution electron micrograph of Mn-SBE (i.e., inverse FFT image) showing pore network and unit cell along *b*-axis.

3.3.3 Thermal Gravimetric Analysis (TG/DTG)

TG data for decomposition of the template in Co-, Mg- and Mn-SBE at 10 K/min in helium gas are shown in Figure 3.6. TG profiles of SBE samples are characterized by three weight

losses up to 1,173 K. TGA curves showed weight losses of about 5% in the low temperature range, which could be attributed to residual physisorbed water molecules. The major weight loss occurred at higher temperatures (e.g. ~ 690 K), which corresponds to the elimination of the 1,9-diaminononane and probable cracking of occluded template molecules to form hydrocarbons and ammonia. For Co-SBE and Mg-SBE, a significant fraction of products of the detemplation were eliminated at temperatures higher than 800 K. It is believed that this last step is related to the desorption of likely ammonia or hydrocarbon fragments that remained adsorbed during the template degradation process. The first weight loss, enclosing the range of 298 - 440 K, corresponds to a 5.7 % for Co- and Mg-SBE. The reduction in weight percent of Mn-SBE due to physisorbed water molecules is relatively low as compared to the other metal aluminophosphates. In the case of Mn-SBE the second weight loss appeared at around 550 K. Theoretical weight losses associated to the desorption of the organic template while leaving ammonium groups (i.e., traditional Hoffman degradation or elimination) for charge balancing of the metal sites are in the range of 17.5 %, 19.3 % and 17.6 % for Co-, Mg- and Mn-SBE, respectively. These values were calculated from the unit cell compositions. Meanwhile, the weight losses observed in the range of 600–750 K are probably related to the removal of the organic template from the crystal lattice, corresponding to an experimental value of 17.4 % for Co-SBE. In the case of Mg-SBE samples, this weight percent was higher (i.e., 19.3 %). The corresponding experimental weight loss value in Mn-SBE is 17.1 % and should be the result of encapsulation of some of the SDA degradation products. The complete collapse of the SBE structure occurs at a temperature range above 700 K, as evidenced by the formation of an amorphous phase.

However, early distortion of the Mn-SBE framework was probably responsible for the aforementioned encapsulation process. This was also confirmed by *in situ* high-temperature XRD data, which will be discussed in detail shortly.

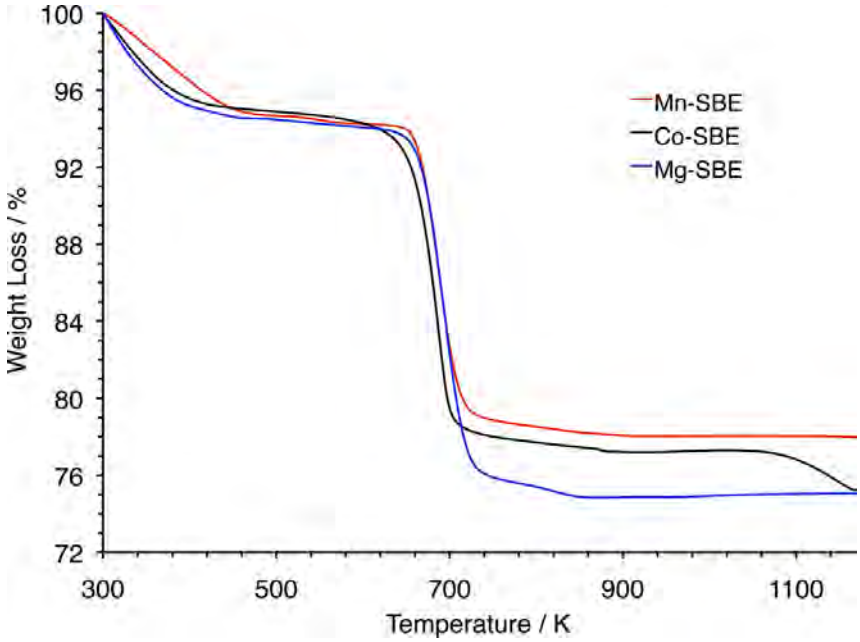

Figure 3.6. TG profiles at 10 K/min obtain in inert atmosphere.

The apparent activation energies (E_a) for the desorption of DAN as calculated from the TG data using the Redhead approach (Equation 3.1) were 182.9 KJ/mol, 188.4 KJ/mol, and 221.8 KJ/mol for Co-, Mg- and Mn-SBE, respectively. As expected, E_a of the Mn-SBE is higher than those for the Co- and Mg-SBE. Among SBE materials, the weight loss percentage of Mn-SBE due to the desorption of water is relatively low and, in addition, the observed TG overall weight loss was smaller when compared to those exhibited by Co-SBE and Mg-SBE, respectively. Note that TGA of as-synthesized SBE samples performed in air showed a vastly different profile from the ones presented here for all SBE-type variants.

Further studies for proper assignment are underway and will be reported in the near future elsewhere.

3.3.4 Optimized Vacuum Detemplation

Attempting the removal of the organic template from a Co-SBE framework was one of the objectives of our previous Chapter.[38] The cobalt-rich SBE samples were subjected to different environments in the investigation of the detemplation process. It was clearly demonstrated by XRD and porosimetry data how detrimental an oxidative thermal treatment is for the SBE framework, to result in framework modification and the formation of a non-porous amorphous phase. Treatment under controlled vacuum conditions, on the other hand, yielded highly porous materials while the surface area values were found to be much smaller than anticipated. Here, a series of experiments were performed to search the optimum conditions (e.g., temperature, heating rate, evacuation rate) for detemplation that could yield the highest possible surface area. Porosimetry tests indicated that the highest micropore surface areas could be obtained using an evacuation rate of 10 mm Hg/s at temperature of 648 K in the heating phase, with minimal effect on the structural stability of the SBE framework. For all the tests, a heating rate of 5 K/min was used and the target temperature at the evacuating phase was kept constant at 373 K for 5 h. Only the temperature for the second ramp was varied.

Figure 3.7 summarizes the micropore and external surface areas obtained with the aforementioned approach. The experimental nitrogen adsorption isotherm was transformed

using the *t*-plot method (Lippens and de Boer) to assess the adsorption capacity and determine the contribution of the micropores to the overall surface area.[57-59] The micropore area was calculated from the extrapolation of the linear range on the *y*-axis while the external surface area was calculated from the slope of the plot. Langmuir surface area values of the as-synthesized samples were 7.3, 5.1 and 2.8 m^2/g for Co-, Mg- and Mn-SBE, respectively. As shown in Figure 3.7, the Mg-SBE samples exhibited the highest surface area with ~ 700 m^2/g (pore volume: 0.24 cm^3/g), followed by the Co-SBE, with ~ 500 m^2/g (pore volume: 0.16 cm^3/g). In the case of Mn-SBE, the same treatment was capable of recovering only 130 m^2/g (pore volume: 0.10 cm^3/g). Overall, the observed trend correlates with framework stress due to multiple coordination states in transition-metal centers, which should be absent in the Mg-SBE variant. Although the same micropore surface area can be attained using a combination of higher evacuation rates and temperatures, higher temperatures resulted in heavy loss of crystallinity and pore shrinkage or deformation. In addition, higher heating rates did not show a noticeable effect in the final properties of the SBE samples. In contrast, prior investigations on stable silicalite-1 zeolites showed that an increased heating rate increases the rate of weight loss on template decomposition.[60]

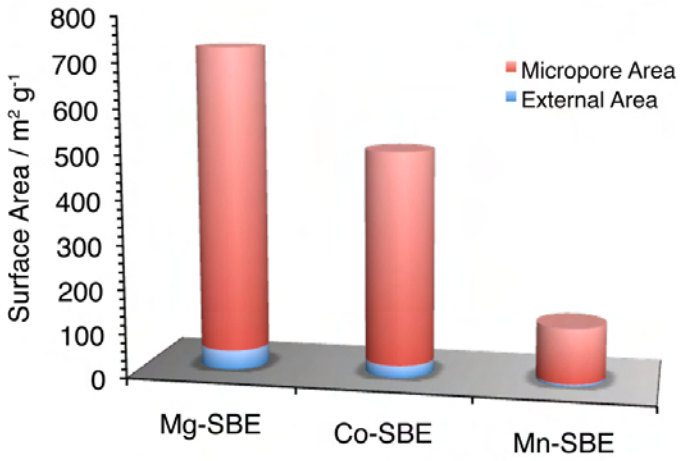

Figure 3.7. Surface area of SBE samples detemplated in vacuum at 648 K.

3.3.5 *In situ* High Temperature and Differential Scanning Calorimetry X-Ray Diffraction

The detemplation process in the SBE frameworks (Co, Mn and Mg) was followed by *in situ* X-ray diffraction in two different atmospheres: air and helium. Helium was employed here to emulate the inert treatment option because maintaining vacuum at high temperatures was not an option for our current setup. Figure 3.8 shows sequential powder patterns obtained while heating the SBE samples from room temperature up to 1,173 K. In the course of treatments, changes in the diffraction patterns revealed a considerable rearrangement and modifications in some of the SBE variants. Shown clearly in Figure 3.8, treatment of all SBE samples at temperatures above 820 K resulted in the eventual formation of a dense $AlPO_4$ phase (i.e., trydimite, structural analogue of SiO_2).[61-64] In general, when comparing the results among all the SBE samples (see Figure 3.8), it is evidently clear that the framework collapses significantly faster in air than in an inert atmosphere (i.e., helium). In addition, the overall

thermal stability of Mg-SBE samples is greater than the ones observed for Co-SBE- or Mn-SBE, which correlates well with the porosimetry analyses presented in the previous section.

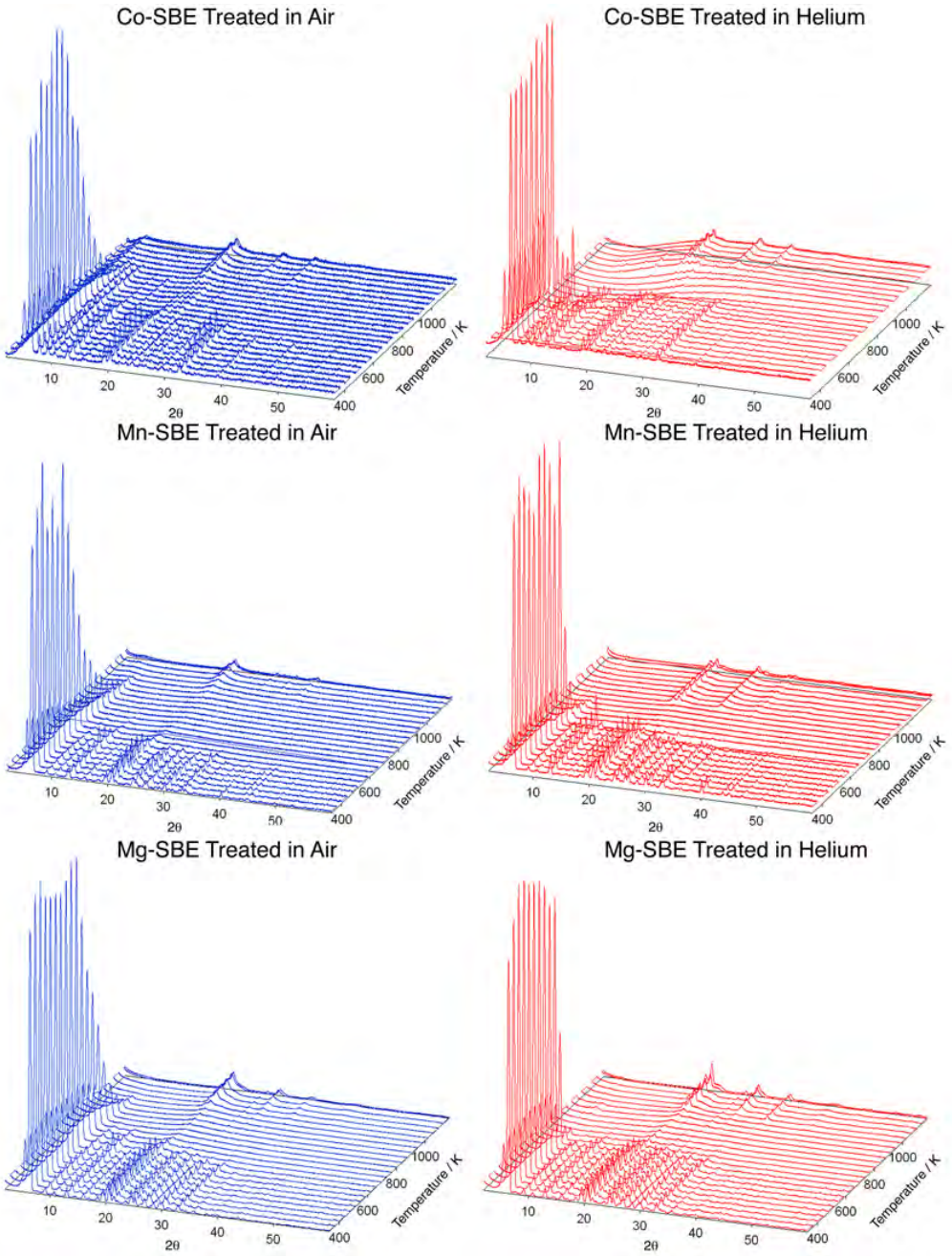

Figure 3.8. *In situ* high-temperature XRD patterns for SBE samples treated under oxidative and inert atmospheres, respectively (maximum temperature: 1173 K).

Before proceeding with a more elaborated discussion of the *in situ* XRD data, it is imperative to further understand the SBE structural features that could be affected during the removal of the template. SBE-type structures are built of ellipsoidal cages connected by an orthogonal channel system and linked to each other at the 12-ring position. This 12-ring window is perpendicular to ATN connections.[65] In tetragonal SBE, 12-ring channels and 8-ring channels, are parallel to (1 0 1) and (0 0 2) planes, respectively (see Figures 3.1 and 3.2). The former plane runs along the unit cell ***b*** axis while the latter one runs parallel to either the ***a*** or ***b*** axes. The SBE supercages are accessible through the 12-ring opening that have a diameter of 0.72 x 0.74 nm.[51] The dimensions of the internal cages are 2.0 nm x 1.5 nm.[36, 37] Since the organic template in the metal aluminophosphate, 1,9-diaminononane, is protonated and bounded to the framework in the stage of as-synthesized powders, it is important to keep in mind that its removal will certainly induce framework changes to compensate for coordination changes. Especially in these cases where the framework metal concentration is high.

During the detemplation process in helium, only minor variations in the Co-SBE XRD patterns were observed in the temperature range from 350 to 450 K that corresponds to the dehydration step in the TG profile. As the temperature was increased up to 500 K, crystallographic planes corresponding to the highest observed intensities [i.e., (1 0 1) and (0 0 2)] showed a displacement to the low 2θ range (i.e., higher *d*-space). These reflections correspond to 2θ angles of 5.6° and 6.4°, respectively, and again are related to the structure channels formed by the inter-connection of the supercages. At temperatures between 500 and

730 K, the framework experienced a considerable lattice expansion associated to the decomposition of the template. This is of utmost importance to allow for unrestricted desorption of the DAN decomposition products during detemplation. At temperatures above 670 K, the (1 0 1) plane showed a subtle displacement to high *d*-space and a sharp increase also related to the template removal.[66]

Mn-SBE detemplation in helium resulted in the most severe framework changes (see Figure 3.8). For instance, the (1 0 1) plane showed a displacement to low *d*-space starting at 513 K; the intensity of the peak increases at around 549 K, followed by a split at 622 K and complete disappearance at 803 K. Such trend indicates atomic re-ordering and plausible distortion/contraction of the framework. Observed changes in the (0 0 2) plane also correlated to a framework contraction. For Mg-SBE samples under helium atmosphere, the (1 0 1) plane showed no variations during the treatment until 694 K. Although the (0 0 2) plane presented a slight expansion at 513 K probably attributed to the release of the SDA, this sample exhibited the most stable framework among all the cases.

The close correlation between the thermal transformation behavior and the framework deformation was also analyzed by means of *in situ* differential heat-flow calorimetric XRD-DSC method. The XRD data was gathered in the 5 to 40º range and at a scan speed of 5°/min. The thermal treatment was performed in both air and helium as mentioned before for three Me-SBE samples, and the data is compiled in Figure 3.9. While the details are discussed below, Figure 3.9 represents a simple overview of the tight correlation between the

framework deformation and exothermic removal of template in air. The result indicates that the traditional calcination detemplation schemes (i.e., with air) are critically detrimental to the transition metal containing SBE frameworks. DSC data shows that the detemplation process in SBE samples clearly consists of two principal steps: (1) elimination of residual physically adsorbed water and (2) SDA decomposition,[53] corroborating the gravimetric results previously reported. The signal above 623 K can be assigned to the decomposition of the DAN^+ cations (see Figure 3.6 for TGA data). However, the oxidative detemplation process in general is both endothermic and exothermic in nature. The Mn-SBE sample showed the lowest onset temperature for this detemplation process, which revealed that it has the less ordered structure among the SBE samples and in agreement with the TGA results. The heat of desorption was calculated by integration of the DSC response. According to the DSC results, the endothermic onset of template desorption occurs at around 400 to 500 K. For the template decomposition in helium, the process was mostly endothermic for the observed temperature range, consuming energies that ranged from 40 to 70 J/g. This can be used as an estimate of the energy of interaction for the host-guest system involving the organic template and the framework. Previous calorimetric studies for the decomposition of tri-(2-aminoethyl)amine (TREN) from Mg-NJU resulted in an endothermic region with an energy of 220.2 J/g for desorption while using nitrogen as the purge gas up to 1473 K.[67]

For Co-SBE samples, the XRD-DSC data reveals that the framework variations onset at about 550 K, leading to the conclusion that the detemplation affects the cobalt coordination in an early stage. When air is used, the XRD data shows that the peak intensity at $2\theta = 17.5^{\circ}$

considerably increases during the exothermic part of the detemplation process for the observed temperature range. This peak corresponds to the (3 1 3) plane and is associated to the STI sub-building units present on the SBE frameworks.[51] Therefore, this sudden change in intensity could be attributed to realignment of the atoms in the STI sub-building units that encompass the supercages. It is plausible to state that the template was coordinated to tetrahedra located in those STI building blocks and that distortion of the framework through these anchorage points was unavoidable upon oxidation of cobalt centers. The latter is evidenced by the eventual loss of most of the (3 1 3) plane intensity. It should be mentioned that these changes are not present in the Co-SBE samples treated in helium.

Mn-SBE samples treated in air result in DSC thermograms with also two distinct regions, one in the low temperature range (endothermic) and another at around 600 K (purely exothermic). Again, these two peaks are attributed to the desorption of water molecules and oxidation of the organic template, respectively. The energy consumption for this second peak was around 1.4 KJ/g and the resulting structural features of the as-synthesized Mn-SBE materials are greatly affected, eventually lacking periodicity and producing the trydimite dense phase previously mentioned (see Figure 3.9). Upon oxidation, the coordination of the Mn centers is compromised and the structure collapsing is necessary to find a thermodynamically stable configuration and dissipate the energy changes associated with the detemplation process.

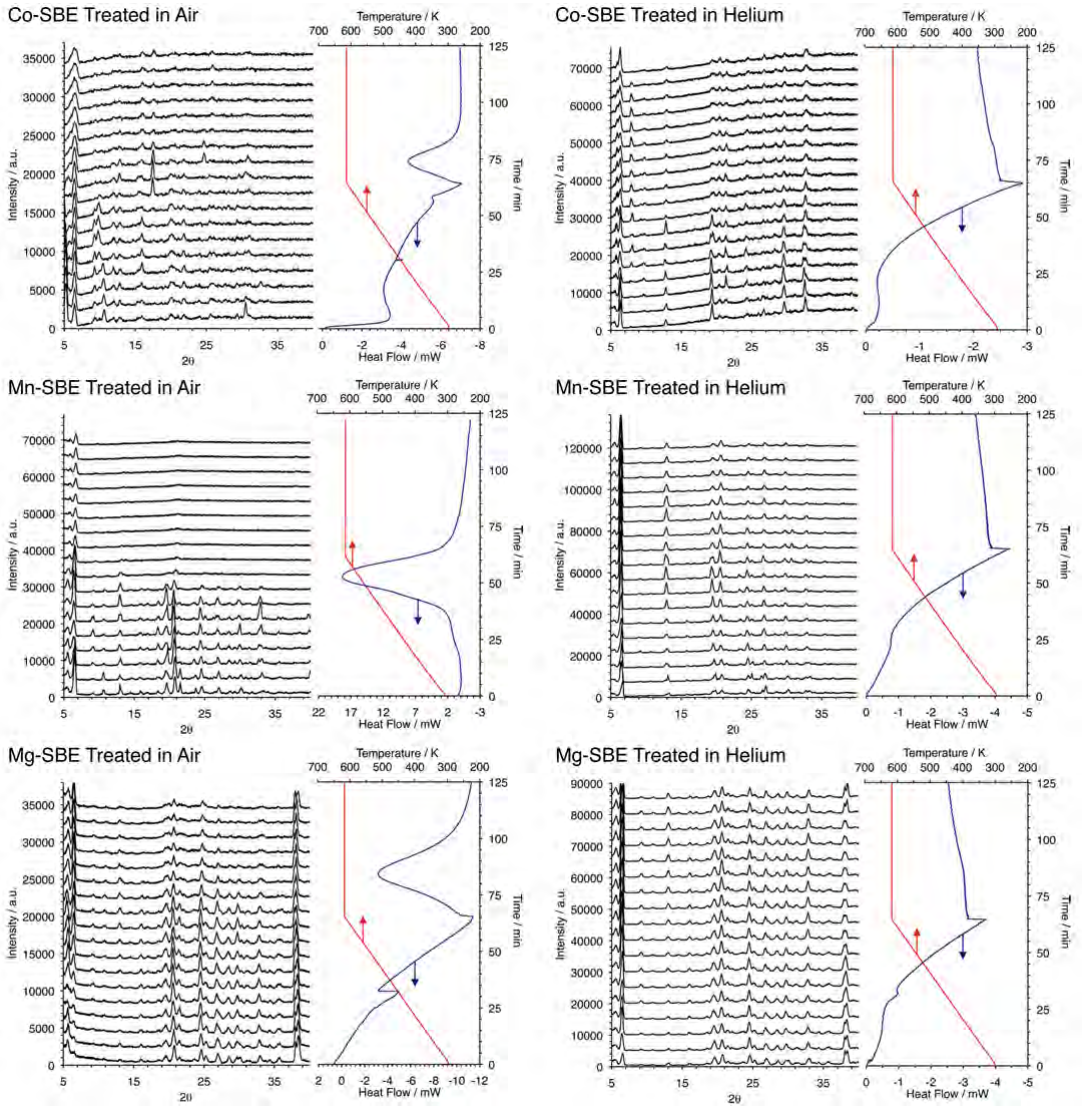

Figure 3.9. *In situ* differential scanning calorimetry XRD data for SBE samples treated under oxidative and inert atmospheres (maximum temperature: 613 K).

3.3.6 FT-IR Spectroscopy

Hernández-Maldonado and co-workers reported FT-IR data for as-synthesized and vacuum pre-treated Co-SBE, as well as the DAN template.[38] The present discussion focuses on the analyses at different temperatures for all the SBE variants. Spectra for all the SBE variants are shown in Figure 3.10. Strong bands associated with symmetric and asymmetric stretching

of the TO_4 tetrahedra were observed in the 1400-650 cm^{-1} region.[68] A broad and intense peak related to the asymmetrical T-O stretching modes is present at ~ 1030 cm^{-1} and at ~ 1040 cm^{-1} for the as-synthesized and detemplated samples, respectively.[69-73] In addition, internal vibrations of the unit cell associated with symmetric stretching modes are observed at 744 and 729 cm^{-1} for the as-synthesized and vacuum treated Co-SBE samples, respectively.[69-73]

For Mg- and Mn-SBE samples, these contributions appear at lower frequencies (~ 740 and ~ 690 cm^{-1}). Weak bands related to deformation modes of CH_2 groups and N-H bending for the as-synthesized SBE were also observed in the 1700 – 1400 cm^{-1} region. In the case of the Mn-SBE detemplated samples, an increase in the intensities and the appearance of new peaks (1370 and 1740 cm^{-1}) were observed in this region. The same observation was made for Co-SBE while their intensities were somewhat weaker. Absorption bands in the 2800-3500 cm^{-1} region (Figure 3.10) were associated to the C-H and N-H stretching vibrations originated from occluded template molecules within the SBE pores. The disappearance of CH_2 bands and reduction in the intensity of N-H stretching amine bands in the Co- and Mg-SBE samples are perhaps related to the removal of the organic species from the framework.

FT-IR at different temperatures in the heating phase of the detemplation process was tested as well. Although, the use of a higher temperature ensures the complete loss of bands related to the presence of the SDA within the framework, it resulted in the structure collapse and/or pore deformation, and is in agreement with porosimetry results. For Mn-SBE samples, the

increase in the intensity of C-H and N-H stretching bands and the appearance of a peak at ~ 2970 cm^{-1} suggests the hosting of other species formed during the detemplation process. This correlates well with the low surface area obtained for Mn-SBE samples from porosimetry testing after an attempt to remove the structure-directing agent (see Figure 3.7) and a lesser overall weight loss in the TG profile (Figure 3.6).

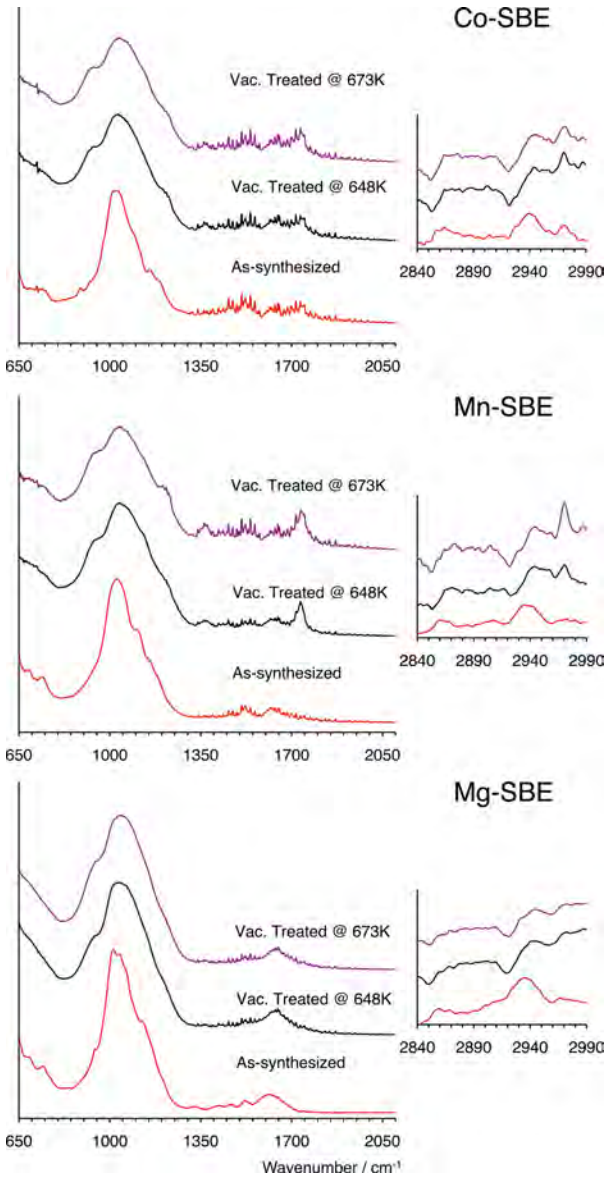

Figure 3.10. FT-IR spectra of SBE samples treated in vacuum at different temperatures (framework and SDA regions).

3.3.7 UV-*vis* Absorption Spectroscopy

Note that due to the fact that Mg is not a *d*-element, UV-*vis* spectra were not available for Mg-SBE. The spectra for the Co-SBE samples were reported in Chapter 2. A single and sharp absorption band at 349 nm seen for the as-synthesized Mn-SBE sample can be assigned to the ligand-to-metal charge transfer (LMCT) from oxygen groups to manganese atoms (Figure 3.11). In addition, there are two distinctive bands at 598 and 629 nm related to the *d-d* transition band.

It is worthwhile to note that for Mn^{2+} in a tetrahedral environment electronic *d-d* transition is Laporte and spin forbidden, so that the *d-d* transition bands appear to be much weaker in intensity compared to those reported for Co-SBE samples.[41] On the other hand, it is also plausible to interpret the observation of such *d-d* transition bands as the existence of species in higher oxidation states that are spin-allowed, suggesting that most of the manganese atoms are present as Mn^{3+} and/or Mn^{4+}. [53, 74-76] Another interesting observation in the current UV-*vis* study is that Mn-SBE samples show UV bands of LMCT and *d-d* transitions identical to those previously observed for Co-SBE (Figure 2.8),[38] regardless of possible energy differences in their *d*-orbitals.

The appearance of a broad and intense band during detemplation treatment of Mn-SBE in vacuum was also observed for air-teated Co-SBE samples.[38] Similar to the latter case, the formation of extra-framework oxide species, Mn_xO_y, could be responsible for the observed

spectral changes. The formation of Mn_xO_y in vacuum implicates the participation of framework oxygen atoms in the metal oxidation and subsequent framework changes. The result is consistent with the XRD, XRD-DSC, and surface area measurements (see Figure 3.7), and further explains the weakness of the Mn-SBE framework upon heat treatments.

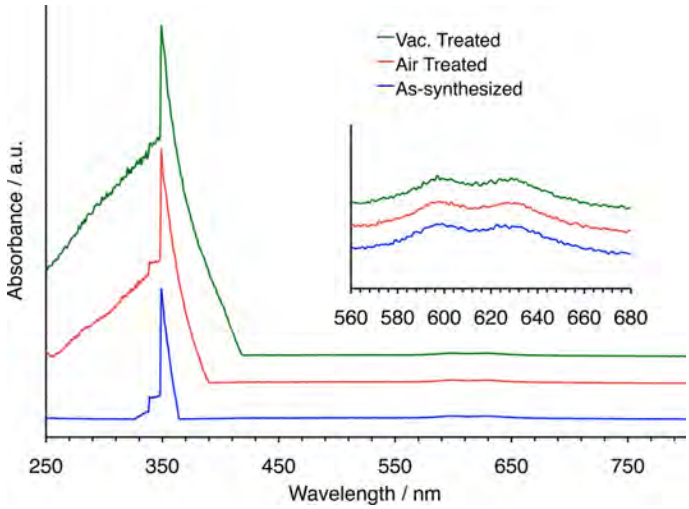

Figure 3.11. UV-*vis* absorption spectra of as-synthesized and treated Mn-SBE samples.

3.3.8 X-Ray Photoelectron Spectroscopy

The XPS spectra of the Co *2p* photoelectron region for as-synthesized and treated SBE samples are presented in Figure 3.12. The energy differences between Co $2p_{1/2}$ and Co $2p_{3/2}$ peaks for the as-synthesized, air and vacuum treated Co-SBE samples are 16.25, 16.00 and 16.00 eV, respectively. These values correspond to a charge-transfer from O *2p* to Co *3p*.[22, 77, 78] Due to the fact that this binding energy difference is close to that of Co^{2+} (16.0 eV) and to a certain extent different from than that Co^{3+} (15.0 eV), the results suggest that cobalt atoms are enclosed in a tetrahedral environment.

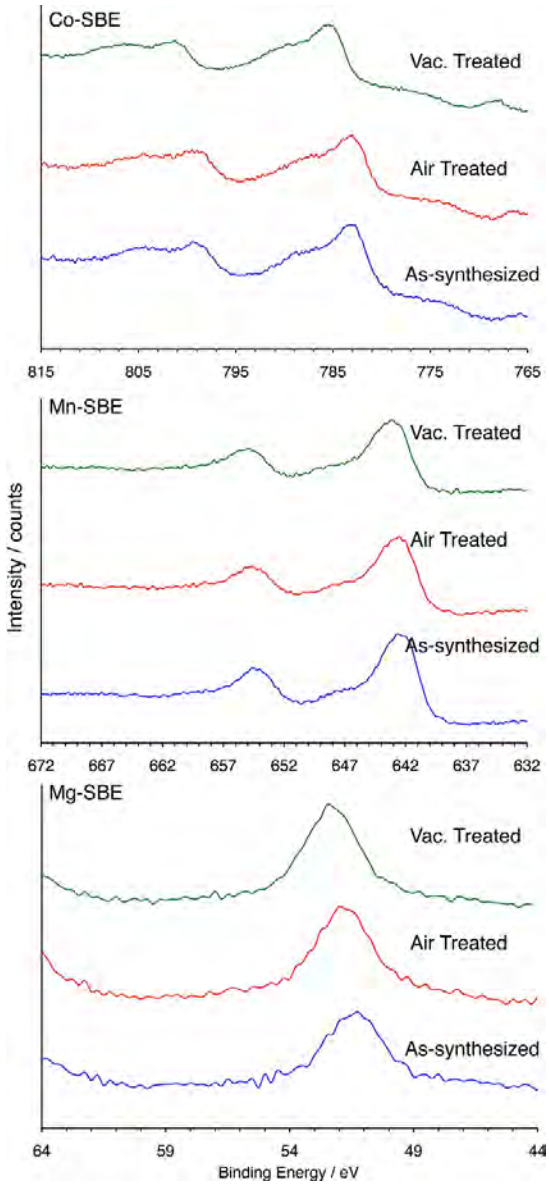

Figure 3.12. XPS spectra for as-synthesized and treated SBE samples.

The binding energies of the photoelectrons from Mg *2p* states in Mg-SBE (Figure 3.12) were found to be 51.25, 51.75, and 52.50 for the as-synthesized, air treated and vacuum treated samples, respectively. These values are close, but higher than the reported by Akolekar (50.3

eV) for the as-synthesized MAPO-39 and -43.[22, 30, 79, 80] Nevertheless, the observed Mg peak appeared at slightly higher binding energies indicating the plausible existence of higher oxidation states. For Mn-SBE samples, the observed Mn $2p_{3/2}$ binding energies were 642.25, 642.50 and 643.0 eV for the as-synthesized, air and vacuum treated SBE samples, respectively, showing a ΔE_b of 12 eV for all the samples. Comparison of the binding energies with the values reported for different Mn-containing compounds in tetrahedral environment, evidences the existence of Mn atoms in higher oxidation states.[81, 82] In fact, the shifting of the binding energy of Mn *2p* peak at 642.0 eV corresponds to MnO_2 species.[83, 84] Therefore, XPS results confirmed that not all Mn atoms are in a tetrahedral environment and again explains the framework distortion observed in the *in situ* high temperature XRD results.

3.3.9 Electron Paramagnetic Resonance Spectroscopy

EPR measurements were made to confirm the paramagnetic nature of the samples and help to elucidate the level of the anticipated broadening in NMR signals since transition metals are highly incorporated in SBE. Figures 3.13A and 3.13B shows the EPR spectra measured at room temperature for Mg- and Mn-SBE as-synthesized and treated samples. For Co-SBE samples, no signal was detected initially at room temperature, and so examination at the low temperature range was carried out (Figures 3.13C). The EPR spectra of Co-SBE samples showed one group of resonances that underwent transition as the temperature was varied around 40K, a broad peak at ca. 1200 G for 4 K < T < 40 K. Observed *g*-factors were about 5.6 and 1.0 (center) for two resonances and the transition from $g = 5.6$ to $g = 1.0$ appeared

around 40 K. The reversible transition was confirmed by varying the temperature up and down. A broad resonance with the *g*-value at 5.6 is close to values reported in previous studies and is considered as a component of *g*-tensors of Co^{2+} ions after substitution in a tetrahedral environment.[21, 54, 85-89] The resonance showed a Curie-Weiss behavior ($I \propto T^{-1}$) in the temperature-intensity plot for all Co-SBE samples and is attributed to the positive zero-field splitting.[90] Note that the reversible transition between the two characteristic EPR resonances at 40 K was observed for all Co-SBE samples regardless of the heat treatments, although only the VT EPR spectra for vacuum treated sample are presented in Figures 3.13C. This indicates that the outcome from EPR measurements is independent of the presence of the organic SDA and its detemplation process. Considering the fact that the unpaired electrons are confined in the *d*-orbitals, and that they are generally sensitive to changes in the local coordination geometry around Co ions in the framework of SBE, it is possible that EPR measurements are not well reflecting the consequences of the structure deformation observed all the way through a number of other techniques.

Unlike the case of Co-SBE, visible changes are observed in EPR spectra of the other materials at room temperature. As-synthesized Mn-SBE showed a broad and intense signal at room temperature (see Figure 3.13A), representing a typical case of paramagnetic electrons delocalized over *d*-orbitals and showing no specific hyperfine couplings. The signal strength was about two orders magnitude higher compared to that of Co-SBE at room temperature. Treatment of the Mn-SBE in air resulted in a slight decrease of the signal intensity, while treatments in vacuum showed less dispersion of the spectral width without any signal

reduction as compared to the as-synthesized Mn-SBE. A strong signature of the formation of Mn_xO_y was observed in the UV-*vis* spectra (see Figure 3.11) for calcined materials. The present EPR spectra, however, do not appear to be correlated with the formation of such extra-framework manganese oxides. The EPR signal loss observed for the air-calcined sample, then, can be linked to the partial oxidation of Mn^{2+} ion [probably to EPR silent Mn(III) at room temperature] while no loss of the vacuum treated samples represented the absence of such oxidation of manganese metal center.

The non-paramagnetic character of Mg^{2+} ions in the SBE framework is shown in Figure 3.13B for the as-synthesized Mg-SBE. Unexpected observation of the EPR signal from the treated samples should be attributed to the formation of paramagnetic defect sites, which were generated during the heat treatment. The air-treated sample showed a stronger EPR signal as compared to the strength of the vacuum treated Mg-SBE. Oxygen appears to be contributing in the generation of paramagnetic sites. DSC results showed that the most severe exothermic process occurred in the presence of oxygen (see Figure 3.9), which is consistent with the present EPR observation. Incomplete removal of the organic SDA or formation of radical fragments and/or dangling bonds as a consequence could be another source for the EPR signal. At this point it is believed that the role of Mg ions in their formation cannot be addressed here because of lack of a systematic investigation.

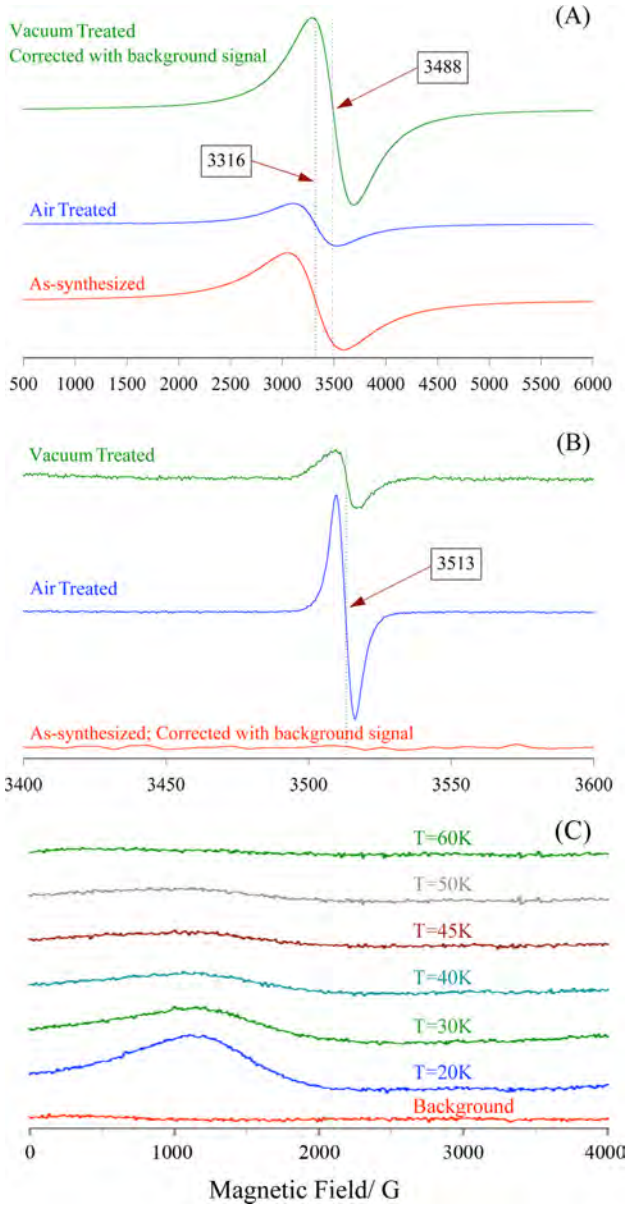

Figure 3.13. EPR spectra for: (A) and (B) as-synthesized and treated Mg- and Mn-SBE samples; (C) at different temperatures for vacuum treated Co-SBE samples.

3.3.10 Solid-State Magic Angle Spinning-Nuclear Magnetic Resonance

Multinuclear MAS-NMR spectroscopy was employed to investigate the structural changes of Me-SBE samples and provide information on Me/Al ordering in the samples in an effort to

detail the detemplation process in the SBE inorganic framework. As presented below, NMR spectroscopy overall revealed complicated features and needs thorough investigation for characterizing the highly paramagnetic samples of Co- and Mn-SBE. Since the spectroscopic details are out of the scope of the present work, NMR results from the paramagnetic systems reported here are limited to an aspect regarding changes aftermath of treatments. The focus will be also made mainly on the diamagnetic Mg-SBE system, which served as a reference, and will be discussed with respect to those of Co- and Mn-SBE.

Figure 3.14 shows the multinuclear MAS-NMR spectra of the diamagnetic Mg-SBE samples at three different conditions: as-synthesized, air-treated and vacuum treated. Both, ^{1}H and ^{13}C NMR spectra of the as-synthesized Mg-SBE sample showed the presence of the organic SDA and the co-solvent intact (see Appendices for ^{13}C assignments) while ^{27}Al and ^{31}P spectra show the framework in good crystallinity (peaks are summarized in Table 3.2). ^{27}Al MAS NMR in particular confirmed that the as-synthesized Mg-SBE sample consists predominantly of tetrahedral Al sites (4P) as indicated by the 45 ppm peak[91] with a small contribution of the octahedral sites at -7 ppm. The Al(4P) environment suggests that almost all of the Mg^{2+} ions substitute onto aluminum tetrahedral sites, with a very small amount octahedrally coordinated. Multiple peaks observed in ^{31}P MAS NMR spectra, on the other hand, reveal the Mg/Al substitution ratio (~ 1.0) and ordering behavior of Mg^{2+} ions around phosphorous atoms: P(nAl, (4-n)Mg) when the strategy used by Barrie and Klinoski was employed.[84]

Table 3.2. Observed NMR peaks for Mg-SBE samples.

Sample	^{1}H (δ, ppm)	^{31}P (δ, ppm)	^{27}Al (δ, ppm)	^{13}C (δ, ppm)
as-synthesized	1.1, 1.8, 3.1, 3.9, 7.5	-26, -20, -15, -10, -3	-7, 45, 131	11, 20, 27, 41, 50
air treated	6	-17, -5	-11, 12, 42	-----
vacuum treated	6	-17	-11, 12, 42	-----

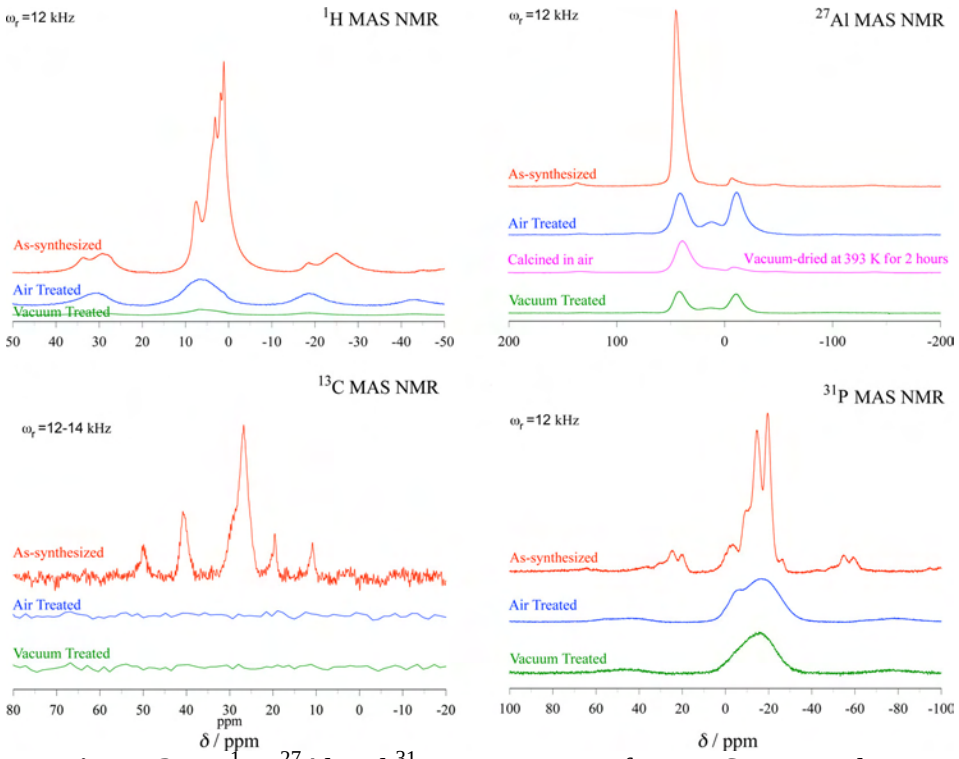

Figure 3.14. ^{1}H, ^{27}Al and ^{31}P NMR spectra for Mg-SBE samples.

The expected changes in NMR spectra are also revealed in Figure 3.14 when the treated samples were examined (middle and bottom spectra for treated in air and vacuum, respectively). While there were some indications by the other methods of possible presence of organic species due to incomplete removal of the organic SDA, in the ^{13}C NMR spectra such species appeared to be nearly absent. Unlike the ^{13}C NMR, sizable ^{1}H MAS NMR

signal is still visible, especially for the air-treated sample. The presence of surface hydroxyl groups and possibly organic fragments could explain the strong ^{1}H NMR spectrum of the air-treated sample. Detemplation in vacuum, on the other hand, showed the hydrogen content significantly reduced compared to that of air-treated sample. Thermal gravimetric analysis in air reported in Chapter 2 indicated that the overall weight loss in SBE samples is considerably less when compared to the one obtained during inert gas treatment.[38] Considering all the experimental data supports the inefficient removal of organic SDA for the air-treated samples, it is highly possible that the ^{1}H NMR signal of air-treated sample revealed the presence of hydrogen rich carbonaceous species, cracked DAN molecules, within the framework. The contradictory finding between ^{13}C and ^{1}H MAS-NMR results should then be associated with a possibility of the responsible organic fragments being paramagnetic radicals, which made the ^{13}C NMR ineffective. The intense EPR signal of air-treated Mg-SBE supports this explanation (Figure 3.13).

The formation of octahedral sites is clearly revealed by the large growth of the -7 ppm peak in ^{27}Al MAS-NMR upon detemplation. The peak at approximately 12 ppm might indicate the presence of penta-coordinated Al sites. The sign of increased aluminum octahedral sites in ^{27}Al NMR might not be interpreted as the formation of extra-framework Al sites, but as the result of coordination with water as confirmed by NMR measurements (see Figure 3.14). ^{27}Al NMR spectrum showed only tetrahedral sites and confirmed the conversion of the octahedral site to the tetrahedral ones after the sample was evacuated at 393 K for 2 hours in order to remove water. Penta-coordinated sites (12 ppm) are present in both air- and vacuum-

treated samples, even though its amount appears to be smaller and broader in the vacuum treated sample. Reduction of the penta-coordinated Al sites after dehydration could be also attributed with loss of water coordination. Upon calcination, the resolution seen in ^{31}P MAS NMR for the as-synthesized material is nearly eliminated as presented in Figure 3.14. Only a broad and featureless peak is reflecting the condition of the phosphorous coordination after treatment either in air or in vacuum. The local structure might be highly amorphous, which might be originated from changes in neighbor atoms like aluminum. Note that the P(0Al, 4Mg) site at -2.9 ppm remained resolved for the air-treated sample only while its significance is not well understood.

For highly paramagnetic Co- and Mn-SBE samples, the influence from unpaired electrons to observing nuclei are strong and the resulting NMR spectra appear to be severely broad and featureless (see Figure 3.15). It is characteristic to see overall a group of spinning sidebands dispersed in a wide spectral range as a result of fast magic angle spinning (~ 12-13 kHz) interfering with the electron-nucleus relaxation behavior. There is no particular resolution that could be interpreted to meaningful structural information for these materials. Changes after heat treatments, however, look relatively distinctive depending on the kind of transition metal and the treatment environment. It is also worthwhile to note that a significant portion of nuclei could be NMR invisible because of stronger influence from paramagnetic electrons. For example, the relative ^{31}P spin concentration of as-synthesized Co-SBE was measured to be less than 10% of that of the as-synthesized Mg-SBE (see Table 3.3). For the case of Mn-SBE, stronger ^{31}P MAS-NMR signal was detected after calcination. The concentration of

unpaired electrons measured by EPR is not just explaining the ^{31}P MAS-NMR spectral changes. This again demonstrates the complicated nature of electron-nuclei interaction, alerting that a great caution needs to be taken for interpretation. Another interesting observation is that the spectral broadening experienced by organic guest molecules, which were mainly probed by ^{1}H and ^{13}C MAS-NMR, indicating tightly bound organic molecules inside of the pores with lack of motional freedom.

Table 3.3. ^{31}P NMR observed signal intensities.

Sample		**Relative Intensities**
Co-SBE	as-synthesized	9.28
	air-calcined	0.00
	vacuum treated	2.35
Mg-SBE	as-synthesized	**100**
	air-calcined	55.0
	vacuum treated	40.0
Mn-SBE	as-synthesized	2.27
	air-calcined	28.1
	vacuum treated	24.6

Reported below, several observations are summarized for behavior of NMR spectra during the heat treatments. For Co-SBE samples, nearly complete removal of ^{1}H NMR signal after treatment is observed both in air and vacuum (see Figure 3.15), which does not necessarily mean SDA-free state. Note that the small dip at 0 ppm in the air and vacuum calcined ^{1}H NMR spectra for Co-SBE is caused by a baseline distortion from a probe background signal. In contrast, there was practically no reduction observed of ^{1}H NMR signal for the Mn-SBE (see Figure 3.15), which is remarkable. This result leads to speculations regarding that the

visible ^{1}H NMR signal might not be directly associated with the detemplating SDA. The observed ^{1}H signal ought to be originated from a source of hydrogen that is not being affected by any heat treatments. Note that ^{13}C MAS NMR for the calcined Mn-SBE was found to be completely undetectable, so was the case of Co-SBE. As stated above, however, the TGA data showed the presence of residual organic molecules to the larger extent for Mn-SBE. Such inconsistency is again not well understood at this point. ^{27}Al NMR spectra of Co-SBE (Figure 3.15) showed broad signals of ^{27}Al of which isotropic chemical shift is in the range of 20 to 40 ppm. The signal can be assigned to a characteristic signal of aluminum nucleus in tetrahedral lattice positions while the broadening of the signals is believed to be the result from the paramagnetic effect of the Co substituted in the framework Al sites.

^{27}Al NMR spectrum of Mn-SBE, on the other hand, showed two types of signals: one is broad and big signals of which isotropic chemical shift is 260 ppm and the other is sharp and small signal at 38 ppm (see Figure 3.15). The latter seems to be a case where ^{27}Al in the tetrahedral sites not having nearby Mn^{2+} substitution. The largely broadened and downshifted 260 ppm peak, then, might result from the tetrahedral Al affected by nearby paramagnetic Mn^{2+} ions. After calcination only sharp peaks were shown at 38 and -8 ppm from tetrahedral and octahedral sites. The sharp peak is in well agreement with the XPS data, which showed binding energies characteristic of the oxidation of paramagnetic Mn^{2+} to non-paramagnetic Mn^{3+} (see Figure 3.12).[92, 93] Mn $2p_{3/2}$ binding energies were 642.25, 642.50 and 643.0 eV for the as-synthesized, air and vacuum treated SBE samples, respectively, showing a ΔE_b of 12 eV for all the samples.

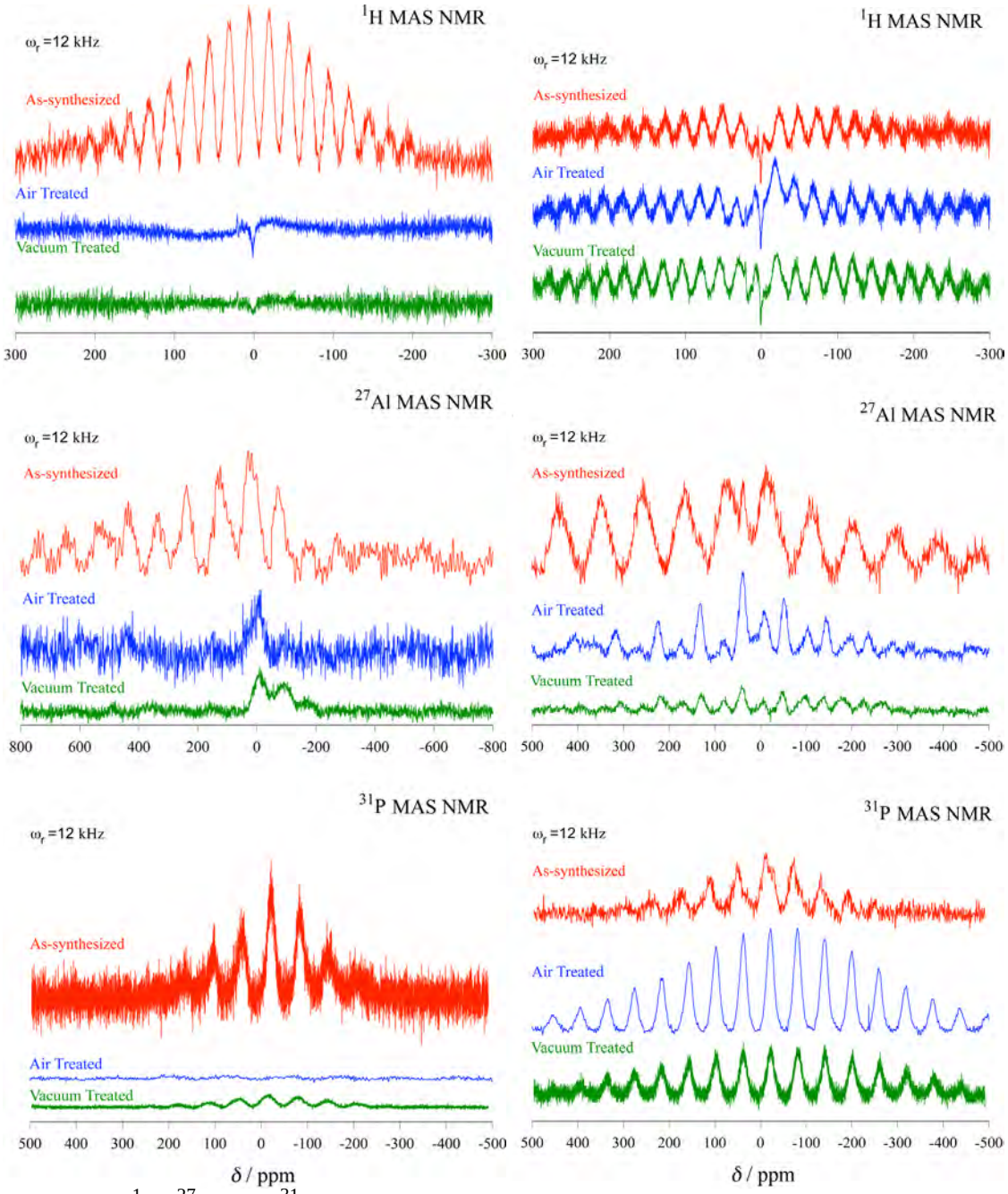

Figure 3.15. ^{1}H, ^{27}Al and ^{31}P NMR spectra for Co-SBE (left) and Mn-SBE (right) samples.

Lastly, the ^{31}P spectrum of as-synthesized Co-SBE and Mn-SBE (see Figure 3.15) presented a strong resonance peak at ca. δ = -25 ppm, characteristic of a tetrahedral phosphorus

coordination sphere [e.g. P(4Al)] surrounded by four aluminum atoms within the framework.[20, 21, 53, 61, 94, 95] For the vacuum treated samples, the observed signal broadening is an indication of the distortion of the PO_4 tetrahedra as was pointed out for the Mg-SBE case. Significant reduction in ^{31}P signal (Table 3.3) compared to the as-synthesized Mg-SBE (I = 100) was the eminent trend, indicating the invisibility of most of ^{31}P signal due to the paramagnetic effect. Therefore, the ^{31}P MAS-NMR signal observed around at -25 ppm is believed to represent P(4Al) sites that are relatively away from the paramagnetic transition metal centers. The rest phosphorous sites appear not to be observed using the conventional single pulse method due to the rapid relaxation of ^{31}P signal.

A Spin-Echo-Mapping (SEMa) technique either in static or MAS has been often selected as a way to recover invisible ^{31}P NMR signal with large shift and broadening. The SEMa method was applied to our Co-SBE and Mn-SBE samples to obtain the invisible ^{31}P signal but it did not show any signal up to 21000 ppm. A report by van Breukelen et al. suggested the existence of clustering of at least five Co atoms to explain the quantity of invisible ^{31}P NMR signal for a range of CoAPO-5 samples.[96] Such effect should be magnified in higher Co/P concentration materials and would explain the results shown here. Unlike the Co-SBE, recovery of ^{31}P NMR signal for Mn-SBE was observed after treatment (see Figure 3.15 and Table 3.3). The extent observed for different treatment environments seems to be consistent with the electron spin concentration (see EPR discussion). Therefore it is possible to correlate the stronger NMR signal with the possibility of losing manganese out of the framework or generating highly oxidized Mn^{3+} or Mn^{4+}, which are not paramagnetic, increasing the visible

phosphorous sites. The recovery of ^{31}P NMR signal of Mn-SBE sample is in agreement with the UV-*vis*, XPS and EPR results, which indicate extra-framework manganese species and multiple oxidation states are formed in both, calcined in air and vacuum treated samples. The smaller recovery of ^{31}P NMR signal in vacuum treated sample than in air treated sample indicated that the oxidation of Mn ions in vacuum calcination occurred less than in air calcination, which is also shown as higher EPR signal intensity in the vacuum treated sample than for the air treated sample.

3.3.11 Water Vapor Adsorption in Mg-SBE

Surface hydrophobicity/hydrophilicity of metal-containing catalysts plays an important role in terms of the catalyst performance and metal leaching.[97-99] Since the Mg-SBE material exhibited the highest surface area upon vacuum detemplation and to support the MAS-NMR results, the water vapor adsorption tests were performed for this SBE variant only. Figure 3.16A shows the water adsorption data for Mg-SBE samples at 298 K where the equilibrium isotherm clearly is of type I according to the IUPAC/BET classification. Type I isotherms are typical of microporous materials, where the saturation value corresponds to an effective pore filling. Equilibrium data indicates that the materials adsorbed water by ca. 27 wt-%, which compares very well with the capacity displayed by commercial sorbents such as natural and synthetic FAU-type zeolites.[100] This capacity translates to about 19 water molecules per super cage while a part of them possibly coordinated to Al octahedral sites as indicated by NMR results. In general, the sorption data evidences that the material is highly hydrophilic.

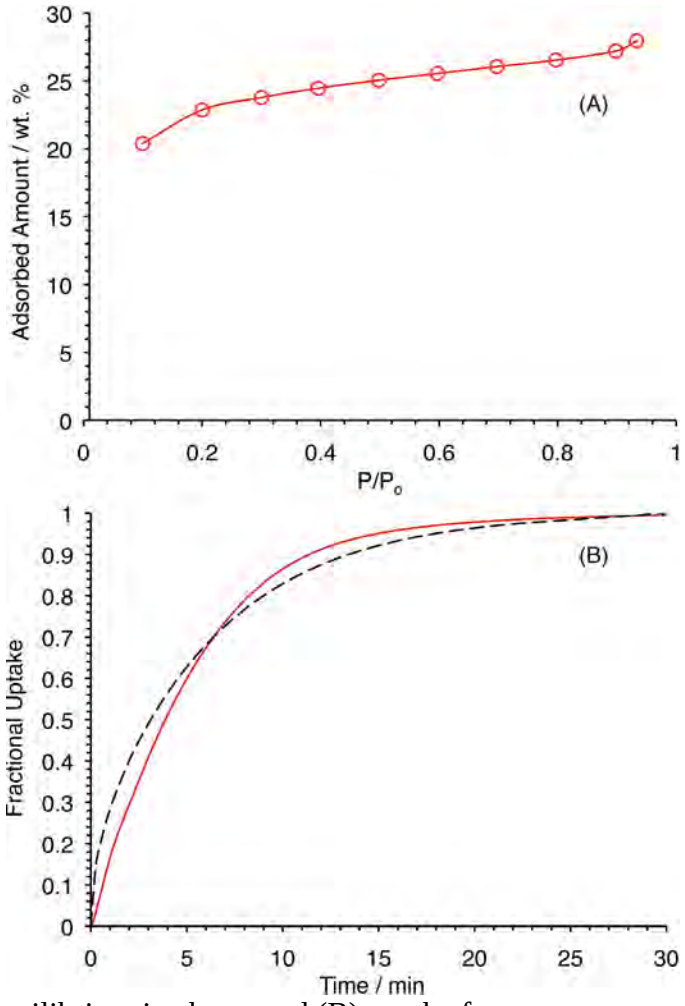

Figure 3.16. (A) Equilibrium isotherm and (B) uptake for water vapor adsorption onto Mg-SBE at 298 K. Kinetic data obtained for a relative pressure step of 0.1. Dashed line corresponds to diffusion in slab type particle phenomenological model.

Figure 3.16B shows kinetic uptake data gathered for a step in relative pressure of 0.1. Equilibrium was reached at ca. 10 minutes (loading: 12 water molecules per unit cell), which is relatively fast as expected. The kinetic or collision diameter of a water molecule is 2.65 Å, sufficiently small to neglect diffusion resistance due any steric effect by the pore channels. Fitting of a slab-shape particle diffusion phenomenological model (Equation 3.2) yields a diffusion time constant of 1.05 x 10^{-3} s^{-1}. Given the observed particles morphology it was

reasonable to assume that such phenomenological model is adequate. However, Figure 3.16B clearly indicates that the model slightly deviates at low and mid times. Deviations like these could be associated to particle size polydispersity[101] and would require further morphological and porosimetry studies for complete understanding.

3.4 Conclusions

Powder forms of Co-, Mg- and Mn-SBE materials were successfully prepared, all containing metal-to-aluminium ratios close to unity. Morphology wise, the Mg- and Mn-SBE materials showcased square plate with truncated corners grown in agglomerates. This differs from Co-SBE materials, which displayed hexagonal plate single particles. Based on this morphology information it seems plausible that the metal sources employed during synthesis played a role in defining the ultimate materials morphology.

Vacuum detemplation using carefully controlled evacuating rates and a temperature of 648 K resulted in SBE materials with surface areas that correlated to microporous structures. The observed surface areas increased as follows: Mn-SBE < Co-SBE < Mg-SBE. It should be mentioned that air detemplation was detrimental to the framework as evidenced by TGA, *in situ* high temperature XRD and XRD-DSC, UV-*vis*, XPS, EPR and MAS-NMR analyses. Although the best detemplation strategy so far consists of employing vacuum or helium atmospheres, the SBE variants still experienced coordination chemistry changes during the course of treatment. ^{27}Al MAS-NMR spectra of Mg-SBE samples, for instance, revealed the reversible formation of aluminium octahedral sites upon water adsorption. The following

summarizes some of the materials features observed during both inert and oxidative detemplation processes:

1. Co- and Mg-SBE frameworks tolerate well detemplation treatment in vacuum or helium. Crystallographic planes associated to the Mn-SBE framework 12-ring channels became considerably displaced during treatment in helium, resulting in a structural distortion and possible encapsulation of the SDA.
2. Mn atoms form extraframework species during detemplation, even in vacuum. This was observed by UV-*vis*, XPS, EPR and MAS-NMR spectroscopic methods.
3. EPR signals for Co-SBE were mainly visible at low temperatures and in the absence of molecular oxygen. Meanwhile, non-paramagnetic Mg-SBE samples still presented EPR signals, possibly attributed to the formation of paramagnetic defect sites generated during the heat treatment.
4. MAS-NMR clearly evidences the high substitution of Al sites by metals during the synthesis. However, the NMR spectra also prove that the SDA interaction with the SBE framework is quite considerable, explaining the observed detemplation challenges. Especially in the case of Mn-SBE samples.

Further effort is still required to completely understand the coordination nature in the SBE samples prior and during detemplation, but the present study clearly demonstrates that successful SDA removal in highly metal substituted AlPOs with multi-dimensional channels is possible.

3.5 Acknowledgements

Funding for the work presented in this chapter was provided by the National Science Foundation (NSF) Awards CBET-0546370 and CBET-0619349. The NMR facility at California Institute of Technology (Pasadena, CA) was supported by the NSF under Grant Number 9724240 and partially supported by the MRSEC Program of the NSF under Award DMR-0520565. Help from Chul Kim and Son-Jong Hwang (California Institute of Technology, Pasadena, CA) for their contribution on EPR and MAS-NMR analyses is appreciatively recognized. The authors wish to gratefully acknowledge help from professors Dr. Carlos Rinaldi and Dr. Carlos Velázquez (UPR-Mayagüez, Chemical Engineering) for providing admittance to FT-IR spectroscopy and SEM/EDX analyses, respectively. Also, our group specially thank to John Bullis and Hiden Analytical Ltd. (Warrington, United Kingdom) for kindly providing the water adsorption analysis. We would also like to acknowledge support from Dr. Raphael Raptis and Dr. Esteban Fachini (UPR-Río Piedras, Chemistry) for their collaboration with UV-*vis* and XPS spectroscopy analyses, respectively. Finally, we recognize Dr. Michael Tsapatsis and co-workers for facilitating HR-TEM analyses [University of Minnesota-Materials Research Science and Engineering Center (UMN-MRSEC)].

LITERATURE CITED

[1] Hartmann, M.; Kevan, L. Transition-Metal Ions in Aluminophosphate and Silicoaluminophosphate Molecular Sieves: Location, Interaction with Adsorbates and Catalytic Properties. *Chem. Rev.* **1999**, *99*(3), 635-663.

[2] Weckhuysen, B. M.; Rao, R. R.; Martens, J. A.; Schoonheydt, R. A. Transition Metal Ions in Microporous Crystalline Aluminophosphates: Isomorphous Substitution. *Eur. J. Inorg. Chem.* **1999**, *1999*(4), 565-577.

[3] Pastore, H. O.; Coluccia, S.; Marchese, L. Porous Aluminophosphates: From Molecular Sieves to Designed Acid Catalysts. *Annu. Rev. Mater. Res.* **2005**, *35*, 351-395.

[4] Gorte, R. J. What Do We Know About the Acidity of Solid Acids? *Catal. Lett.* **1999**, *62*(1), 1-13.

[5] Chen, J.; Thomas, J. M. MAPO-18 (M=Mg, Zn, Co): A New Family of Catalysts for the Conversion of Methanol to Light Olefins. *J. Chem. Soc., Chem. Commun.* **1994** (5), 603-604.

[6] Silva, A. O. S.; Souza, M. J. B.; Araujo, A. S. Hydrothermal Synthesis and Thermal Characterization of Niobium-Aluminophosphate with AEL Structure. *Int. J. Inorg. Mater.* **2001**, *3*(6), 461-466.

[7] Thomas, J. M.; Greaves, G. N.; Sankar, G.; Wright, P. A.; Chen, J. S.; Dent, A. J.; Marchese, L. On the Nature of the Active-Site in a CoAPO-18 Solid Acid Catalyst. *Angew. Chem. Int. Edit.* **1994**, *33*(18), 1871-1873.

[8] Chen, J. S.; Sankar, G.; Thomas, J. M.; Xu, R. R.; Greaves, G. N.; Waller, D. Cobalt-Substituted Aluminophosphate Molecular-Sieves - X-Ray Absorption, Infrared Spectroscopic, and Catalytic Studies. *Chem. Mater.* **1992**, *4*(6), 1373-1379.

[9] Fan, W. B.; Li, R. F.; Dou, T.; Tatsumi, T.; Weckhuysen, B. M. Solvent Effects in the Synthesis of CoAPO-5, -11 and -34 Molecular Sieves. *Micropor. Mesopor. Mater.* **2005**, *84*(1-3), 116-126.

[10] Fan, W. B.; Schoonheydt, R. A.; Weckhuysen, B. M. Synthesis of Co-Rich CoAPO-CHA Molecular Sieves in the Presence of Ethanol and Cesium. *Chem. Commun.* **2000**, (22), 2249-2250.

[11] Batista, J.; Kaučič, V.; Rajić, N.; Stojakovic, D. On the Formation of CoAPSO-44. *Zeolites* **1992**, *12*(8), 925-928.

[12] Hill, S. J.; Williams, C. D.; Duke, C. V. A. The Synthesis of High Cobalt-Containing CoAPO-34. *Zeolites* **1996**, *17*(3), 291-296.

[13] Canesson, L.; Tuel, A. Synthesis and Characterization of CoAPO(4)-39 Molecular Sieves. *Zeolites* **1997**, *18*(4), 260-268.

[14] Yokomori, Y.; Kawachi, Y. Synthesis of Large Single-Crystals of CoAPO-5 Molecular-Sieves. *Zeolites* **1995**, *15*(7), 637-639.

[15] Duke, C. V. A.; Hill, S. J.; Williams, C. D. Synthesis of MnAPO-20 and CoAPO-20 Using Tetrahedral Metal Species. *J. Chem. Soc., Chem. Commun.* **1994**, (22), 2633-2633.

[16] Singh, P. S.; Shaikh, R. A.; Bandyopadhyay, R.; Rao, B. S. Synthesis of CoVPI-5 with Bifunctional Catalytic Activity. *J. Chem. Soc., Chem. Commun.* **1995**, (22), 2255-2256.

[17] Ahn, S.; Chon, H. The Influence of Metal Ions on the Synthesis of MeAPO-5 (Me = Co, Mg) in the Presence of Acetate Ions. *Micropor. Mater.* **1997**, *8*(3-4), 113-121.

[18] Meusinger, J.; Vinek, H.; Lercher, J. A. Cracking of N-Hexane and N-Butane over SAPO-5, MgAPO-5 and CoAPO-5. *J. Mol. Catal.* **1994**, *87*(2-3), 263-274.

[19] Marchese, L.; Chen, J. S.; Thomas, J. M.; Coluccia, S.; Zecchina, A. Bronsted, Lewis, and Redox Centers on CoAPO-18 Catalysts: 1. Vibrational-Modes of Adsorbed Water. *J. Phys. Chem.* **1994**, *98*(50), 13350-13356.

[20] Montes, C.; Davis, M. E.; Murray, B.; Narayana, M. Isolated Redox Centers within Microporous Environments: 1. Cobalt-Containing Aluminophosphate Molecular-Sieve 5. *J. Phys. Chem.* **1990**, *94*(16), 6425-6430.

[21] Prakash, A. M.; Hartmann, M.; Kevan, L. Synthesis, Characterization, and Adsorbate Interactions of CoAPO-41 and CoAPSO-41 Molecular Sieves. *J. Phys. Chem. B* **1997**, *101*(35), 6819-6826.

[22] Akolekar, D. Investigations on the CoAPO-36 Molecular-Sieve. *Catal. Lett.* **1994**, *28*(2-4), 249-262.

[23] Zhang, G. A.; Harris, T. V. X-Ray Absorption Studies of Cobalt Aluminophosphate Zeolites (CoAPO-5). *Physica B* **1995**, *209*(1-4), 697-698.

[24] Perot, G. Hydrotreating Catalysts Containing Zeolites and Related Materials: Mechanistic Aspects Related to Deep Desulfurization. *Catal. Today* **2003**, *86*(1-4), 111-128.

[25] Moden, B.; Oliviero, L.; Dakka, J.; Santiesteban, J. G.; Iglesia, E. Structural and Functional Characterization of Redox Mn and Co Sites in AlPO Materials and Their Role in Alkane Oxidation Catalysis *Journal of Physical Chemistry B* **2004**, *108*(18), 5552-5563.

[26] Concepción, P.; López Nieto, J. M.; Pérez-Pariente, J. Oxidative Dehydrogenation of Ethane on a Magnesium-Vanadium Aluminophosphate (MgVAPO-5) Catalyst. *Catal. Lett.* **1994**, *28*(1), 9-15.

[27] Wan, B. Z.; Huang, K. MnAPO-5 as a Catalyst for Ethane Oxydehydrogenation. *Appl. Catal.* **1991**, *73*(1), 113-124.

[28] Zubowa, H. L.; Richer, M.; Roost, U.; Parlitz, B.; Fricke, R. Synthesis and Catalytic Properties of Substituted AlPO-34 Molecular Sieves. *Catal. Lett.* **1993**, *19*(1), 67-79.

[29] Sotelo, J. L.; Uguina, M. A.; Valverde, J. L.; Serrano, D. P. Kinetics of Toluene Alkylation with Methanol over Mg-Modified ZSM-5. *Ind. Eng. Chem. Res.* **1993**, *32*, 2548-2554.

[30] Akolekar, D.; Kaliaguine, S. Preparation and Characterization of the Magnesium Aluminophosphate MAPO-39. *Zeolites* **1994**, *14*, 620-624.

[31] Akolekar, D. B. Investigations on the Characteristics, Surface, Acidity Acid Strength Distribution and Catalytic Properties of the Zinc-Substituted Aluminophosphate of Type-36 Molecular-Sieve. *Appl. Catal. A-Gen.* **1994**, *112*(2), 125-139.

[32] Akolekar, D. B. Comparison of Thermal-Stability, Acidity, Catalytic Properties and Deactivation Behavior of Novel Aluminophosphate-Based Molecular-Sieves of Type-36. *J. Chem. Soc., Faraday Trans.* **1994**, *90*(7), 1041-1046.

[33] Akolekar, D. B. Acidity and Acid Strength Distribution of the Crystalline Microporous MAPO-36 Molecular-Sieve. *Zeolites* **1994**, *14*(1), 53-57.

[34] Akolekar, D. B. Catalytic Properties and Deactivation Behavior of Crystalline Microporous MAPO-36. *J. Catal.* **1993**, *144*(1), 148-159.

[35] Akolekar, D. B. Crystalline Microporous MAPO-36 Molecular Sieve: Synthesis and Characterization. *J. Catal.* **1993**, *143*(1), 227-238.

[36] Bu, X. H.; Feng, P. Y.; Stucky, G. D. Large-Cage Zeolite Structures with Multidimensional 12-Ring Channels. *Science* **1997**, *278*(5346), 2080-2085.

[37] Feng, P. Y. Synthesis and Characterization of Transition Metal Phosphate-Based Novel Framework Materials. Doctoral Dissertation, University of California, Santa Barbara, 1998.

[38] Belen-Cordero, D. S.; Mendez-Gonzalez, S.; Hernandez-Maldonado, A. J. SBE Type Cobalt Aluminophosphate Nanoporous Materials: Degradation of the Structure-Directing Agent. *Micropor. Mesopor. Mater.* **2008**, *109*(1-3), 287-297.

[39] Alfaro, S.; Rodríguez, C.; Valenzuela, M. A.; Bosch, P. Aging Time Effect on the Synthesis of Small Crystal LTA Zeolites in the Absence of Organic Template. *Mater. Lett.* **2007**, *61*(23-24), 4655-4658.

[40] Bo, W.; Hongzhu, M. Factors Affecting the Synthesis of Microsized NaY Zeolite. *Micropor. Mesopor. Mater.* **1998**, *25*(1-3), 131-136.

[41] Ojha, K.; Pradhan, N. C.; Samanta, A. N. Zeolite From Fly Ash: Synthesis and Characterization. *Bull. Mater. Sci.* **2004**, *27*(6), 555-564.

[42] Szostak, R. *Molecular Sieves: Principles of Synthesis and Identification*. Blackie Academic and Professional, Thomson Science: New York, 1998.

[43] Langmuir, I. The Adsorption of Gases on Plane Surfaces of Glass, Mica and Platinum. *J. Am. Chem. Soc.* **1918**, *40*, 1361-1403.

[44] Parrillo, D. J.; Gorte, R. J. Characterization of Acidity in H-ZSM-5, H-ZSM-12, H-Mordenite, and H-Y Using Microcalorimetry. *J. Phys. Chem.* **1993**, *97*(34), 8786-8792.

[45] Hernandez-Maldonado, A. J.; Yang, R. T.; Chinn, D.; Munson, C. L. Partially Calcined Gismondine Type Silicoaluminophosphate SAPO-43: Isopropylamine Elimination and Separation of Carbon Dioxide, Hydrogen Sulfide, and Water. *Langmuir* **2003**, *19*(6), 2193-2200.

[46] Fesenko, E. A.; Barnes, P. A.; Parkes, G. M. B.; Brown, D. R.; Naderi, M. A New Approach to the Study of the Reactivity of Solid-Acid Catalysts: The Application of Constant Rate Thermal Analysis to the Desorption and Surface Reaction of Isopropylamine from NaY and HY Zeolites. *J. Phys. Chem. B* **2001**, *105*(26), 6178-6185.

[47] Redhead, P. A. Thermal Desorption of Gases. *Vacuum* **1962**, *12*(4), 203-211.

[48] Tomková, E. TDS Spectra Analysis. *Surf. Sci.* **1996**, *351*(1-3), 309-318.

[49] Ruthven, D. M. *Principles of Adsorption and Adsorption Processes*. Wiley: New York, 1984.

[50] Do, D. D. *Adsorption Analysis: Equilibria and Kinetics*. Imperial College Press: London, 1998.

[51] Baerlocher, C.; McCusker, L. B., Database of Zeolite Structures. In International Zeolite Association Synthesis Commission: 2007.

[52] Borges, C.; Ribeiro, M. F.; Henriques, C.; Lourenço, J. P.; Murphy, D. M.; Louati, A.; Gabelica, Z. Structural State and Redox Behavior of Framework Co(II) in CoIST-2: A Novel Cobalt-Substituted Aluminophosphate with AEN Topology. *J. Phys. Chem. B* **2004**, *108*(24), 8344-8354.

[53] Tušar, N. N.; Mali, G.; Arçon, I.; Kaučič, V.; Ghanbari-Siahkali, A.; Dwyer, J. Framework Cobalt and Manganese in MeAPO-31 (Me = Co, Mn) Molecular Sieves. *Micropor. Mesopor. Mater.* **2002**, *55*(2), 203-216.

[54] Thomson, S.; Luca, V.; Howe, R. Framework Co(II) in CoAPO-5. *Phys. Chem. Chem. Phys.* **1999**, *1*(4), 615-619.

[55] Fan, W. B.; Schoonheydt, R. A.; Weckhuysen, B. M. Hydrothermal Synthesis of Co-Rich CoAPO-5 Molecular Sieves. *Phys. Chem. Chem. Phys.* **2001**, *3*(15), 3240-3246.

[56] Szostak, R., Synthesis of Molecular Sieve Phosphates In *Molecular Sieves - Science and Technology*, Springer Berlin / Heidelberg: 1998; Vol. 1, pp 157-185.

[57] Lippens, B. C.; de Boer, J. H. Studies on Pore Systems in Catalysts V. The t-Method. *J. Catal.* **1965**, *4*(3), 319-323.

[58] de Boer, J. H.; Linsen, B. G.; Osinga, T. J. Studies on Pore Systems in Catalysts VI. The Universal t-Curve. *J. Catal.* **1965**, *4*(6), 643-648.

[59] de Boer, J. H.; Linsen, B. G.; van der Plas, T.; Zondervan, G. J. Studies on Pore Systems in Catalysts VII. Description of the Pore Dimensions of Carbon Blacks by the t-Method. *J. Catal.* **1965**, *4*(6), 649-653.

[60] Gualtieri, M. L.; Gualtieri, A. F.; Hedlund, J. The Influence of Heating Rate on Template Removal in Silicalite-1: An In Situ HT-XRPD Study. *Micropor. Mesopor. Mater.* **2006**, *89*(1-3), 1-8.

[61] Akolekar, D. B.; Howe, R. F. NMR Investigation of Substituted-Aluminophosphate AEL, ATS, ATN, AFS, AFY and GIS Molecular Sieves. *J. Chem. Soc., Faraday Trans.* **1997**, *93*(17), 3263-3268.

[62] Smith, J. Topochemistry of Zeolites and Related Materials. 1. Topology and Geometry. *Chem. Rev.* **1988**, *88*, 149-182.

[63] Akolekar, D.; Kaliaguine, S. MAPO-43 Molecular Sieve: Synthesis, Characterization and Thermal Stability. *Micropor. Mater.* **1994**, *2*, 137-144.

[64] Akolekar, D. B.; Bhargava, S. Investigations on the Aqueous Solution and Solid-State Cation Exchanged MAPO-ATS Type Molecular Sieve. *J. Mol. Catal. A-Chem.* **1997**, *122*(1), 81-90.

[65] McCusker, L. B.; Brunner, G. O.; Ojo, A. F. The Synthesis, Structure Determination and Rietveld Refinement of the Magnesium Aluminophosphate MAPO-39. *Acta Crystallogr.* **1990**, *A46*, C59.

[66] Jeong, H. K.; Lai, Z.; Tsapatsis, M.; Hanson, J. C. Strain of MFI Crystals in Membranes: An In Situ Synchrotron X-Ray Study. *Micropor. Mesopor. Mater.* **2005**, *84*, 332-337.

[67] Li, Y. X.; Zhang, H. T.; Li, Y. Z.; Xu, Y. H.; You, X. Z. Hydrothermal Synthesis and Characterization of Magnesium Substituted Aluminophosphate with Unique Intersecting 12-Membered Ring Channels in Three Dimensions. *Micropor. Mesopor. Mater.* **2006**, *97*(1-3), 1-8.

[68] Akolekar, D.; Bhargava, S.; van Bronswijk, W. Fourier Transform Raman Spectroscopy of Novel Aluminophosphate Molecular Sieves. *Appl. Spectrosc.* **1999**, *53*(8), 931-937.

[69] Jacobs, W. P. J. H.; van Wolput, J. H. M. C.; van Santen, R. A. Fourier-Transform Infrared Study of the Protonation of the Zeolitic Lattice Influence of Silicon: Aluminium Ratio and Structure. *J. Chem. Soc., Faraday Trans.* **1993**, *89*(8), 1271-1276.

[70] Chao, K. J.; Sheu, S. P.; Sheut, H. S. Structure and Chemistry of Cobalt in CoAPO-5 Molecular Sieve. *J. Chem. Soc., Faraday Trans.* **1992**, *88*(19), 2949-2954.

[71] Pichat, P.; Beaumont, R.; Barthomeuf, D. Infra-Red Structural Study of Aluminium-Deficient Y Zeolites. *J. Chem. Soc., Faraday Trans.* **1974**, *70*, 1402-1407.

[72] Janchen, J.; Peeters, M. P. J.; van Wolput, J. H. M. C.; Wolthuizen, J. P.; van Hooff, J. H. C.; Lohse, U. CoAPO Molecular Sieve Acidity Investigated by Adsorption Calorimetry and IR Spectroscopy. *J. Chem. Soc., Faraday Trans.* **1994**, *90*(7), 1033-1039.

[73] Miecznikowski, A.; Hanuza, J. Application of the Long Chain Approach to the Structure and Vibrational Spectra of X and Y Zeolites. *Zeolites* **1985**, *5*, 188-193.

[74] Halenius, U.; Westlund, E. Manganese Valency and the Colour of the $Mn_2AsO_4(OH)$ Polymorphs Eveite and Sarkinite. *Miner. Mag.* **1998**, *62*(1), 113-119.

[75] Wu, J.; Chien, S. H.; Wan, B. Z. Characterization of MnAPO-5 for Ethane Oxydehydrogenation. *Ind. Eng. Chem. Res.* **2001**, *40*, 94-100.

[76] Moden, B.; Zhan, B. Z.; Dakka, J.; Santiesteban, J. G.; Iglesia, E. Kinetics and Mechanism of Cyclohexane Oxidation on MnAPO-5 Catalysts. *J. Catal.* **2006**, *239*, 390–401.

[77] Chao, K. J.; Wei, A. C.; Wu, H. C.; Lee, J. F. Characterization of Metal-Incorporated Molecular Sieves. *Catal. Today* **1999**, *49*, 277-284.

[78] Borade, R. B.; Clearfield, A. Acidity of Silicon Modified CoAPO-5 Molecular Sieves. *Appl. Catal. A-Gen.* **1992**, *80*, 59-77.

[79] Akolekar, D.; Kaliaguine, S. Synthesis, Characterization, Termal Stability, Acidity and Catalytic Properties of Large-Pore MAPO-46. *J. Chem. Soc., Faraday Trans.* **1993**, *89*(22), 4141-4147.

[80] Akolekar, D.; Ryoo, R. Titanium Incorporated ATS and AFI Type Aluminophosphate Molecular Sieves. *J. Chem. Soc., Faraday Trans.* **1996**, *92*(22), 4617-4621.

[81] Jiang, J.; Kucernak, A. Electrochemical Supercapacitor Material Based on Manganese Oxide: Preparation and Characterization. *Electrochim. Acta* **2002** *47*, 2381-2386.

[82] Strohmeier, B. R.; Hercules, D. H. Surface Spectroscopic Characterization of Mn/Al_2O_3 Catalysts. *J. Phys. Chem.* **1984**, *88*, 4922-4929.

[83] Kim, J. S.; Kim, Y. K.; Lee, S. R. Thermal and Mn Diffusion Behaviors of CoNbZr-Based Spin Valves With Nano Oxide Layers. *IEEE Trans. Magn.* **2003**, *39*(5), 2824-2826.

[84] Vieira, A.; Tovar, M. A.; Pfaff, C.; Betancourt, P.; Mendez, B.; Lopez, C. M.; Machado, F. J.; Goldwasser, J.; de Agudelo, M. M. R.; Houalla, M. A Study of Manganese-Silicoaluminophosphate Molecular Sieves. *J. Mol. Catal. A-Chem.* **1999**, *144*(1), 101-116.

[85] Kurshev, V.; Kevan, L.; Parillo, D. J.; Pereira, C.; Kokotailo, G. T.; Gorte, R. J. An Investigation of Framework Substitution of Cobalt into Aluminophosphate-5 Using Electron-Spin-Resonance and Temperature-Programmed Desorption Measurements. *J. Phys. Chem.* **1994**, *98*(40), 10160-10166.

[86] Beale, A. M.; Sankar, G.; Catlow, R. A.; Anderson, P. A.; Green, T. L. Towards an Understanding of the Oxidation State of the Cobalt and Manganese Ions in Framework Substituted Microporous Aluminophosphate Redox Catalysts: An Electron Paramagnetic Resonance and X-Ray Absorption Spectroscopy Investigation. *Phys. Chem. Chem. Phys.* **2005**, *7*, 1856-1860.

[87] Wu, C.; Chao, K.; Chang, H.; Lee, L.; Naccache, C. Study of Oxygen-Binding Cobalt Species on CoAPO-11 Molecular Sieve Under Redox Treatment. *J. Chem. Soc., Faraday Trans.* **1999**, *93*(19), 3551-3553.

[88] Verberckmoes, A. A.; Weckhuysen, B. M.; Schoonheydt, R. A. Spectroscopy and Coordination Chemistry of Cobalt in Molecular Sieves. *Micropor. Mesopor. Mater.* **1998**, *22*, 165-178.

[89] Weckhuysen, B. M.; Verberckmoes, A. A.; Uytterhoeven, M. G.; Mabbs, F. E.; Collison, D.; Schoonheydt, R. A. Electron Spin Resonance of High-Spin Cobalt in Microporous Crystalline Cobalt-Containing Aluminophosphates. *J. Phys. Chem. B* **2000**, *104*, 37-42.

[90] Weil, J. A.; Bolton, J. R.; Wertz, J. E. *Electron Paramagnetic Resonance: Elementary Theory and Practical Applications*. 1st edition ed.; Wiley-Interscience: New York, 1994; p 664.

[91] Deng, F.; Yue, Y.; Xiao, T. C.; Du, Y.; Ye, C.; An, L.; Wangs, H. Substitution of Aluminum in Aluminophosphate Molecular Sieve by Magnesium: A Combined NMR and XRD Study. *J. Phys. Chem.* **1995**, *99*, 6029-6035.

[92] Jiang, J.; Kucernak, A. Electrochemical Supercapacitor Material Based on Manganese Oxide: Preparation and Characterization. *Electrochim. Acta* **2002** *47*, 2381-2386.

[93] Strohmeier, B. R.; Hercules, D. H. Surface Spectroscopic Characterization of Mn/Al_2O_3 Catalysts. *J. Phys. Chem.* **1984**, *88*, 4922-4929.

[94] Zahedi-Niaki, M. H.; Xu, G.; Meyer, H.; Fyfe, C. A. Synthesis and Characterization of $AlPO_4$-36: A Novel Aluminophosphate Molecular Sieve with ATS Structure. *Micropor. Mesopor. Mater.* **1999**, *32*, 241–250.

[95] Prakash, A. M.; Chilukuri, S. V. V.; Ashtekar, S.; Chakrabarty, D. K. Synthesis and Characterization of Large-Pore Molecular Sieves CoSAPO-36 and CoSAPO-46. *J. Chem. Soc., Faraday Trans.* **1996**, *92*(7), 1257-1262.

[96] van Breukelen, H. F. W. J.; Kraaijvelda, G. J. C.; van de Ven, L. J. M.; de Haanb, J. W.; van Hooff, J. H. C. Clustering of Cobalt in CoAPO-5 Molecular Sieves. *Micropor. Mater.* **1997**, *12*, 313-322.

[97] Corma, A. State of the Art and Future Challenges of Zeolites as Catalysts. *J. Catal.* **2003**, *216*(1-2), 298-312.

[98] Zhao, X. S.; Lu, G. Q. Aluminophosphate-Based Mesoporous Molecular Sieves: Synthesis and Characterization of TAPOs. *Micropor. Mesopor. Mater.* **2001**, *44*, 185-194.

[99] Logar, N.; Kaučič, V. Nanoporous Materials: From Catalysis and Hydrogen Storage to Waste Water Treatment. *Acta Chim. Slov.* **2006**, *53*, 117-135.

[100] Breck, D. W. *Zeolite Molecular Sieves*. Wiley: New York, 1973.

[101] Ruthven, D. M.; Loughlin, K. F. The Effect of Crystallite Shape and Size Distribution on Diffusion Measurements in Molecular Sieves. *Chem. Eng. Sci.* **1971**, *26*, 577-584.

CHAPTER 4

ALTERNATIVE METHODS FOR THE REMOVAL OF THE STRUCTURE-DIRECTING AGENTS

4.1 Non-Traditional Post-Synthesis Treatments for the Removal of the Structure-Directing Agents

Molecular sieves are inorganic solids mostly prepared by hydrothermal synthesis and in some instances require the presence of an organic template or structure-directing agent surrounded by the inorganic metal atoms to finally adapt to the desired framework topology (i.e., organic–inorganic hybrid). After synthesis, the organic template is usually still confined within the cavities of the solid and it is necessary to remove it from the material to obtain a porous matrix.

Among large-pore molecular sieves, SBE are promising nanoporous materials for adsorption applications as demonstrated by our previous studies (see Chapters 2 and 3).[1] Prior to the use of non-traditional methods of template removal, the SBE samples were tested for detemplation in air and nitrogen atmospheres, respectively (results in Figure 2.5). Moreover, SBE samples were also degassed in vacuum under controlled temperature conditions. As stated before, this dissertation focuses in the complete removal of the structure-directing agent from the thermally unstable SBE-type structure.

Since the oxidative treatment (i.e., calcination) was evidently detrimental to the SBE framework, it was decided to explore other methods such as solvent extraction (SE), ion exchange (IE) techniques and ultra-violet (UV) illumination/ozone (O_3) irradiation for detemplation. Two aspects taken in consideration are (1) the protonation of the organic template and (2) the plausible existence of non-protonated organic moieties within the framework. The use of both techniques, solvent extraction and ion exchange, could help to remove both "free" and protonated SDAs and produce higher surface areas when used in a concurrent fashion.

In this study, the properties of SBE-type materials prior and after post-synthesis treatments are described and compared to vacuum detemplation results. Methods employed to remove the organic template include ion exchange, solvent extraction and ambient temperature UV-O_3 treatment.

4.2 Experimental Section

4.2.1 Ion Exchange and Solvent Extraction

As-synthesized samples of SBE were modified by ion exchange and/or solvent extraction with several exchangeable cations and/or solvents. Solvent extractions (Table 4.1) were performed using a solvent volumetric ratio of 1:1. Approximately 1 g of sample was contacted with 100 mL of aqueous solvent solution (50 v/v% water) and heated in Teflon-lined autoclaves (Parr Instruments Co., Moline, IL) with stirring at 343 K for 24 h. Cation Exchange Capacity (CEC) for SBE was estimated to be 2.81 meq/g. Table 4.2 compiles the

CEC for the salts used in the ion-exchange experiments. Ion exchange experiments were performed in a simple equilibration batch stage and a high solution/zeolite cations equivalent ratio (10:1) with stirring at 343 K for 24 h.

Table 4.1. Solvents used for extraction of Co-SBE samples.

Solvent	Density (g/mL)	Amount equivalent to 50 gram (mL)
methanol	0.791	63.21
acetic acid	1.049	47.66
tert-butyl methyl ether (MTBE)	0.740	67.57
methyl acetate	0.932	53.65
ethanol	0.789	63.37
1-propanol	0.804	62.19
2-propanol	0.785	63.69
tert-butanol	0.775	64.52
ethanolamine	1.012	49.41

Table 4.2. Cation exchange capacity (CEC) of salts used for ion exchange experiments.

Salt	FW (g/mol)	CEC (meq/g)
NaCl	58.44	17.11
KCl	74.65	13.40
LiCl	42.39	23.59
$CaCl_2$	110.98	18.02
$MgCl_2$	95.21	21.01

4.2.2 Vacuum Detemplation and Ion Exchange

Co-, Mg-, and Mn-SBE samples were modified by ion exchange at two different temperatures (i.e., 298 K and 313 K) using lithium chloride (LiCl) as the exchangeable cation salt. SBE samples were ion exchanged after vacuum detemplation at 648 K. Mg-SBE

samples were also vacuum detemplated at 648 K after the ion exchange. Ion exchange experiments here were performed also in a simple equilibration stage using a batch system and a high solution/zeolite cations equivalent ratio (10:1) with stirring for 24 h at the specified temperature. Sodium hydroxide (0.01 M NaOH) or hydrochloric acid (0.01 M HCl) solutions were used in some instances to adjust the pH of the matrix.

4.2.3 Mild Oxidative Template Removal by Ultraviolet Irradiation

Removal of the organic template using ultraviolet (UV) illumination was attempted by forming a thin layer of the Mg-SBE powder over an aluminum foil inside an UV resistant Plexiglas closed chamber equipped with a short/long wavelength UV lamp (6 W, 254/365 nm wavelength, Cole-Parmer®, USA) at 254 nm and exposed to an airflow of 60 mL/min for a period of 12 h. The 1,9-diaminononane (DAN) samples were exposed to short and long wavelength ultraviolet light (i.e., λ = 254 and 365 nm) in either static air or airflow as specified above. Mg-SBE samples were exposed to an ozone-generating short-wavelength ultraviolet light (λ = 254 nm). Samples were placed about 2–3 cm below the light source. Ozone generated in this process is supposed to effectively oxidize the framework template into gaseous products. For comparison purposes, the information regarding samples treated in vacuum (Chapters 2 and 3) for the removal of the SDA (i.e., 6 h at 373 K, followed by 18 h at 648 K) is also included in this chapter.

4.2.4 Materials Characterization: Standard Powder X-Ray Diffraction, Porosimetry Tests and FT-IR Spectroscopy

As-synthesized samples were characterized by X-Ray Powder Diffraction (XRD) and Scanning Electron Microscopy (SEM) for determination of phase purity and morphology, respectively. XRD analyses were performed using a Rigaku ULTIMA III X-ray diffraction unit equipped with cross beam optics and a CuK_{α} target operating at 40 *k*V and 44 *m*A. The diffraction angle *(2θ)* range was set to 2-60°.

A Micromeritics ASAP 2020 instrument was used for activation of as-synthesized samples (i.e., detemplation) and acquisition of porosimetry data. The former was accomplished using the sample activation module while the latter was gathered using the static volumetric adsorption setup of the instrument. Before measurements, the samples were degassed at 423 K at a heating rate of 5 K/min and an evacuation rate of 10 mm Hg/s for 6 h. Porosimetry tests were performed using adsorption of nitrogen at 77 K. The specific surface area was determined according to the Langmuir approach in the relative pressure (P/P_o) range of 0.01–0.20.[2]

Fourier Transformed Infra-Red (FT-IR) spectra were recorded in the spectral range 3500 – 650 cm^{-1} using a Bruker IFS 66V/S spectrophotometer equipped with a Bruker IR Microscope and a liquid N_2-cooled MCT detector.

4.3 Results and Discussion

4.3.1 Ion Exchange and Solvent Extraction

Exchangeable cations within the zeolite structure can be replaced (i.e., exchanged) with other positive ions in solution, without affecting the framework. Therefore, ion exchange allows one to create materials with a wide range of pores sizes and shapes, besides the fact that the composition may also change. Zeolites comprising a large amount of aluminum centers typically have loosely-bound charge balancing extra-framework small cations. Here, the ion exchange method was used to help remove large protonated moieties within the SBE framework. Moreover, solvent extraction was employed as an approach to remove non-protonated species and also coupled to an ion exchange technique. As Figure 4.1 shows, the volume of nitrogen adsorbed at high relative pressures by the SBE that underwent lithium ion exchange was far greater than the quantity adsorbed by either sample that underwent solvent extraction. As shown in Table 4.3, the higher surface areas were obtained when both techniques (i.e., solvent extraction and ion exchange) were coupled.

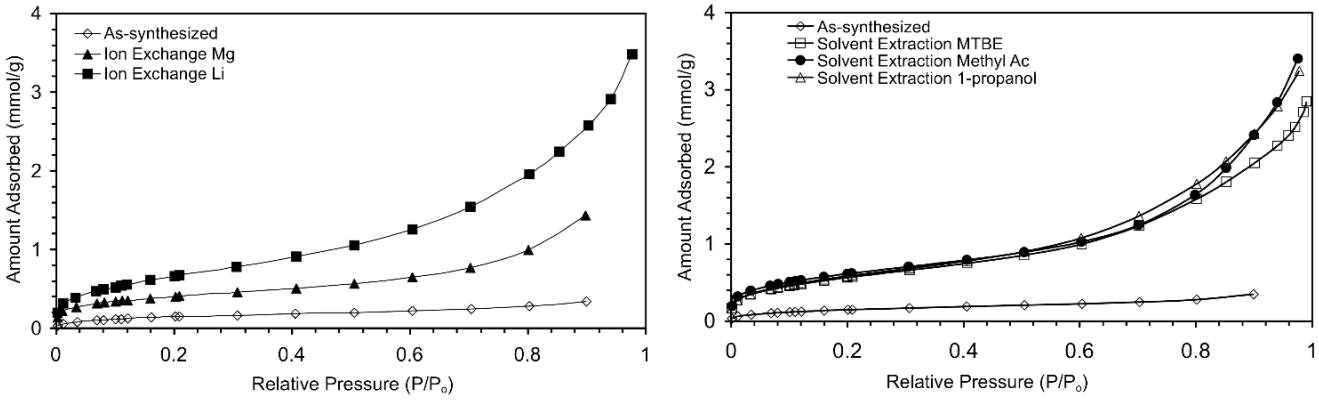

Figure 4.1. Nitrogen adsorption isotherms at 77 K for as-synthesized and treated materials by ion exchange (left) and solvent extraction (right).

Table 4.3. Surface area of as-synthesized and treated Co-SBE materials.

Post-synthesis treatments	Langmuir Surface Area (m^2/g)	pH
Co-SBE as-synthesized	**7**	**7.4**
Co-SBE (IE Mg^{2+})	40	7.5
Co-SBE (IE Na^+)	41	8.8
Co-SBE (IE Li^+)	**66**	**6.1**
Co-SBE (SE MTBE/H_2O)	56	6.3
Co-SBE (SE 1-propanol/H_2O)	58	5.6
Co-SBE (SE methyl acetate/H_2O)	**61**	**6.2**
SE methyl Ac/H_2O and IE Li^+	**85**	-----
SE MeOH/H_2O and IE Li^+	**92**	
SE MTBE/H_2O and IE Li^+	**98**	

Surface areas of Co-SBE samples treated (Table 4.4 and Figure 4.2) with sodium hydroxide (NaOH) and sodium hydroxide/sodium chloride (NaOH/NaCl) solutions measured were 139 m^2/g and 239 m^2/g for the sample treated with NaOH and NaOH/NaCl, respectively. These values are almost ten times the surface area of the as-synthesized samples. Salt solutions and acid-base treatments appeared to influence the structural stability of cobalt-substituted SBE materials. The pH of the sample solutions (Table 4.4) was very alkaline and it is known that aluminophosphates are stable at $2.2 < pH < 11.5$ with no phase transformation but the crystallinity is strongly dependent.[3] Indeed, the range of pH scale used affects the crystallinity of the samples by a drastic reduction of the intensity and disappearance of some characteristic peaks of the Co-SBE crystalline XRD pattern (not shown here) that are associated to the pore windows (i.e., plane 101).

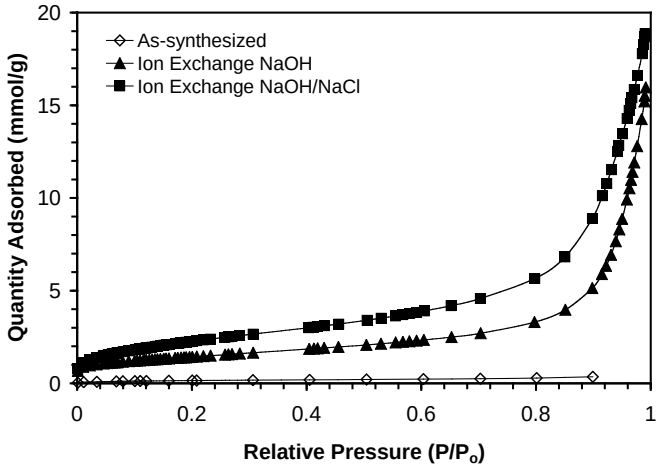

Figure 4.2. Nitrogen adsorption isotherms at 77K (left) for post-synthesis treatments of the Co-SBE samples with NaOH and NaOH/NaCl.

Table 4.4. Surface areas for Co-SBE samples ion exchanged with NaOH and NaOH/NaCl.

Post-synthesis treatments	Surface Area (m^2/g)		pH
	Langmuir	External	
Co-SBE IE NaOH	139	-----	12.4
Co-SBE IE NaOH/NaCl	239	219	12.2

There are many questions that should be answered before concluding that an ideal sorbent was finally developed and can be useful for a particular application. Was the structure-directing agent removed by either of the techniques mentioned before? What happens during the post-synthesis treatments? High surface areas were obtained but the areas measured were almost in the same range of the external surface areas measured (Table 4.4). Micropore areas were very low and most of the sorption capacity was the contribution from the external surface area. Hence, the organic template was not successfully removed. At least not completely.

4.3.2 Vacuum Detemplation and Ion Exchange

The nitrogen adsorption isotherms generated for the ion exchange of Co-SBE samples with LiCl are shown in Figure 4.3. Although the amount of nitrogen adsorbed by the ion exchanged Co- and Mn-SBE samples at 313 K was higher (Table 4.5) neither of the samples displayed a significant increase in surface area when compared to the as-synthesized samples. The same behavior was observed for the Mg-SBE samples as the temperature of the ion exchange was varied and samples were vacuum treated after the ion exchange. Samples showed to be more stable by using this procedure rather than vacuum detemplation followed by ion exchange (Table 16; see samples at pH = 7.1). When the ion exchanged samples were vacuum detemplated at 648 K, the surface area values were reduced by 100 m^2/g as compared to the vacuum detemplated samples alone. However, samples ion exchanged after vacuum treatments showed an insignificant surface area value. XRD of Mg-SBE samples ion exchanged after vacuum detemplation confirmed an amorphous pattern, indication of the loss of the SBE crystalline structure and complete collapse of the framework (Figure 4.4).

Table 4.5. Surface area of ion exchanged SBE samples prior and after vacuum detemplation.

Post-synthesis treatment	Surface Area (m^2/g)		
	Langmuir	Micropore	External
Co-SBE IE 298 K	6.2	0.2	6.0
Co-SBE IE 313 K	19.8	0.7	19.1
Co-SBE IE at 298 K after VT at 648 K	6.9	-----	6.9
Co-SBE IE at 313 K after VT at 648 K	11.1	-----	11.1
Mn-SBE IE 298 K	6.9	0.3	6.5
Mn-SBE IE 313 K	19.6	1.1	18.5
Mn-SBE IE at 298 K after VT at 648 K	2.1	0.5	1.6
Mn-SBE IE at 313 K after VT at 648 K	7.2	1.7	5.5

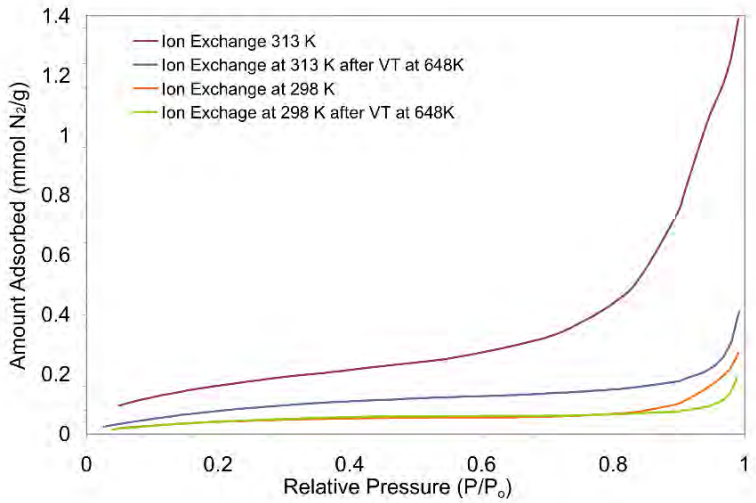

Figure 4.3 Nitrogen adsorption isotherms at 77 K of Co-SBE samples ion exchanged at different temperatures prior and after vacuum detemplation.

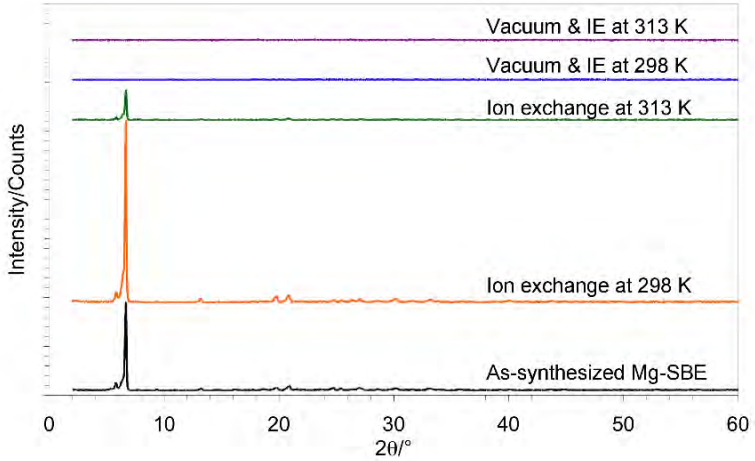

Figure 4.4. Powder XRD pattern of Mg-SBE samples after ion exchange with lithium chloride at different temperatures prior and after treatments in vacuum at 648 K.

Mg-SBE samples were also ion exchanged as a function of pH. The pH of the LiCl solution was varied between 2 and 11 to control the ion exchange ratio. The surface area increased with an increase in pH until it reached a maximum value (Figure 4.5) at a neutral pH. Treatments at low and high pH resulted in the formation of a complete amorphous phase, as

revealed by XRD patterns (Figure 4.6) and low sorption capacity from the nitrogen adsorption measurements (Figure 4.7 and Table 4.6). However, after vacuum treatments all ion exchanged samples showed a decrease in crystallinity (Figure 4.4) and exhibited lower sorption capacity as compared to vacuum detemplated samples alone due to the structure collapse. These findings indicate that as mentioned before, the SBE materials are not stable under ion exchange conditions after template removal in vacuum.

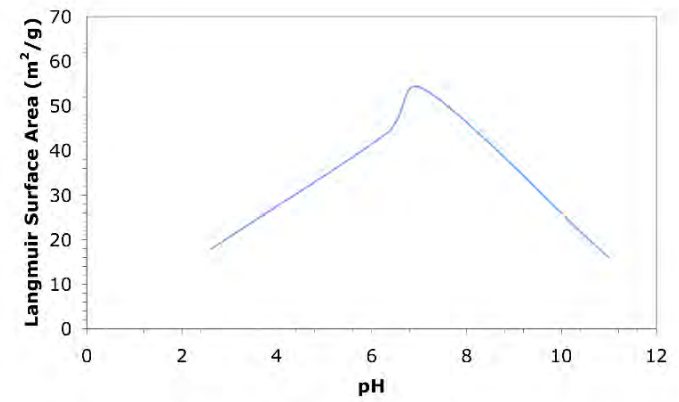

Figure 4.5. Effect of the pH in the surface area of Mg-SBE samples ion exchanged at different pH prior to vacuum detemplation.

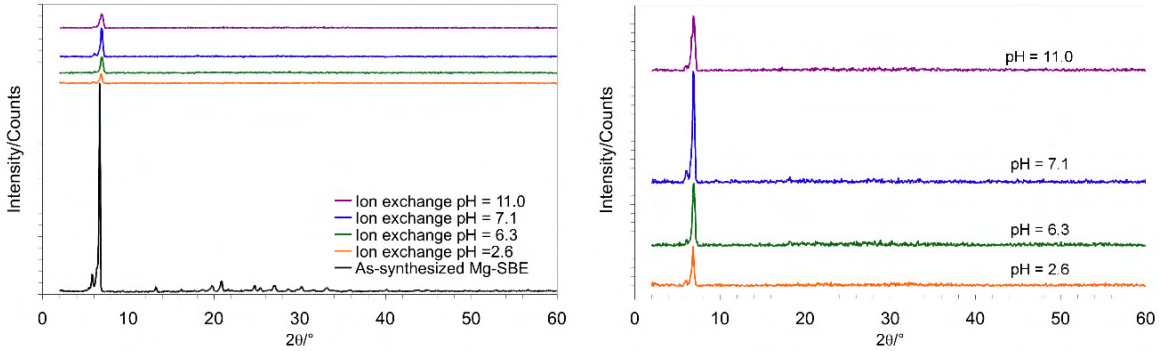

Figure 4.6. Powder XRD pattern of Mg-SBE samples after ion exchange with lithium chloride at different pH.

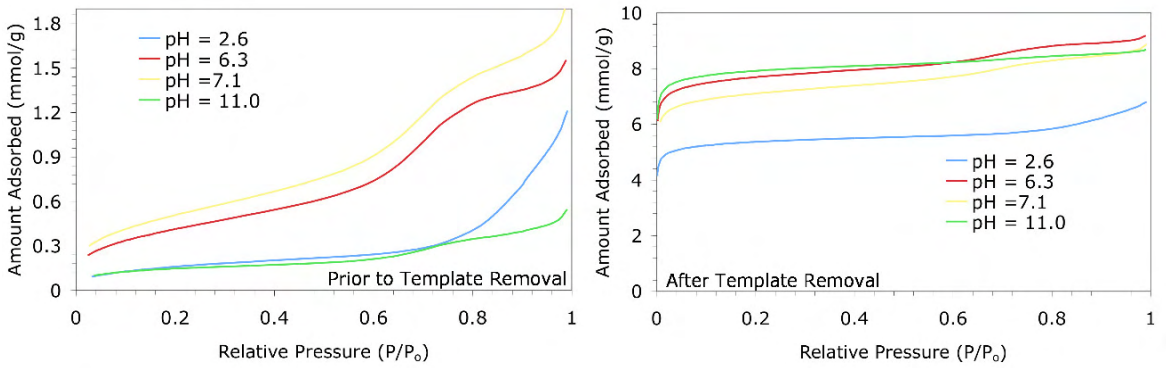

Figure 4.7. Nitrogen adsorption isotherms at 77 K of Mg-SBE samples ion exchanged at different pH prior (left) and after vacuum detemplation (right).

Table 4.6. Surface areas of Mg-SBE samples as a function of pH.

Ion exchange prior to vacuum treatments.				
pH	Langmuir (m^2/g)	Micropore (m^2/g)	External (m^2/g)	H-K (Å)
2.6	17.8	2.1	15.6	19.038
6.3	43.7	5.4	38.3	17.691
7.1	**53.8**	**7.3**	**46.4**	**16.305**
11	15.8	5.6	10.3	19.886
Vacuum detemplation after ion exchange.				
pH	Langmuir (m^2/g)	Micropore (m^2/g)	External (m^2/g)	H-K (Å)
2.6	522.1	459.7	62.4	9.058
6.3	747.8	647.2	100.6	9.485
7.1	**693.0**	**587.3**	**105.7**	**10.86**
11	770.5	688.3	82.2	9.005

4.3.3 Mild Oxidative Template Removal by Ultraviolet Irradiation

In an effort to eliminate the structure-directing agent from zeo-type materials, some researchers have discovered that this could be possible by treating the samples using UV irradiation at room temperature.[4-8] Another method recently discovered uses UV/dilute H_2O_2 to remove organic moieties from mesoporous silica SBA-15[9] by the photochemical oxidation (i.e., degradation) of the surfactant.

Short wavelength UV-light (i.e., 254 nm) used in conjunction with airflow has been identified as a source for generating ozone (O_3), which can in fact oxidize organic SDAs at room temperature. 1,9-diaminononane samples were dissolved in ethanol and exposed to an oxidative environment in static air or airflow and at two different wavelengths. FT-IR spectra (Figure 4.8) did not show any significant changes among samples.

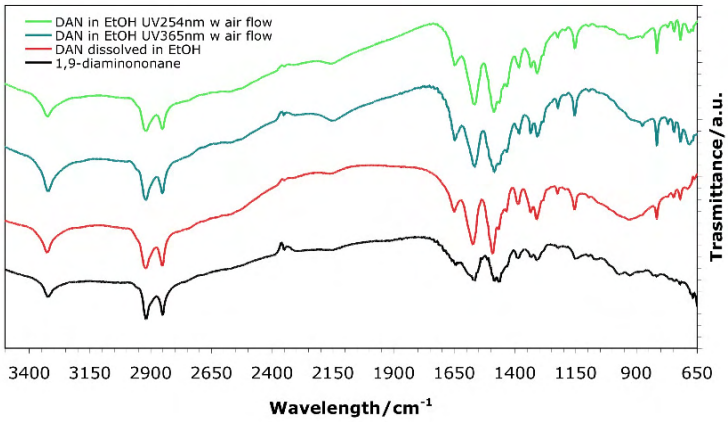

Figure 4.8. FT-IR spectra of 1,9-diaminononane samples irradiated with UV-light at two different wavelengths under static air or airflow conditions.

The XRD patterns shown in Figure 4.9 indicated that the Mg-SBE materials irradiated with UV light were highly crystalline. FT-IR spectra of as-synthesized and UV-treated Mg-SBE samples are shown in Figure 4.10. Although, the FT-IR spectra are not in accordance with the XRD results, both samples showed similar patterns indicative of the loss of an ordered structure as the bands associated to the lattice vibrations (i.e., low frequency region) became broad, with reduced intensity and shifted to higher wavelengths. Studies of surface area in the UV-O_3 treated samples indicated that the method was not capable of removing the

organic template as the surface area were almost in the same range of the as-synthesized samples.

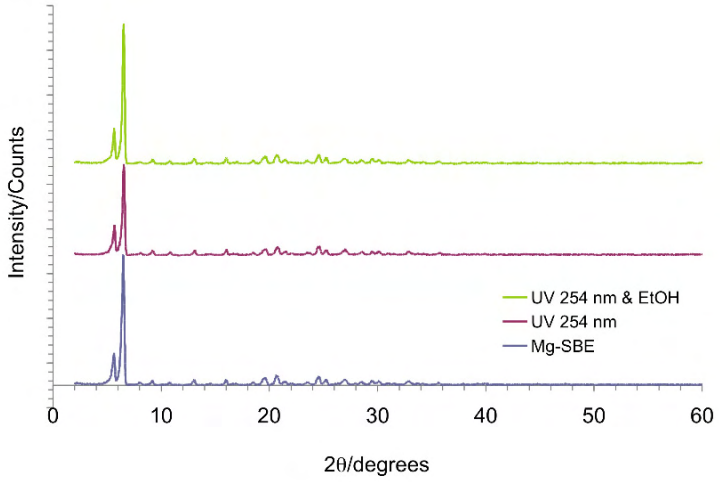

Figure 4.9. XRD patterns for as-synthesized Mg-SBE and UV-light treated samples with at wavelength of 254 nm.

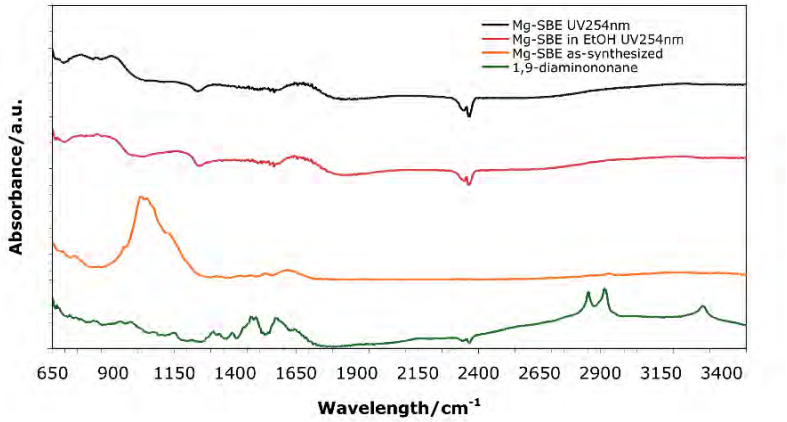

Figure 4.10. FT-IR spectra of as-synthesized samples and UV-illuminated samples using a wavelength of 254 nm.

4.4 Conclusions

In summary, this chapter identifies ion exchange, solvent extraction as well as UV-O_3 treatments as alternative methods to high-temperature thermal calcination method. The

central benefit of coupling the ion exchange and solvent extraction methods as an approach to remove the structure-directing agent was to help to eliminate protonated and non-protonated species and avoid a two-stage process. When subjected to the ion exchange and solvent extraction treatments, the combination of these techniques resulted in higher surface areas as compared to the methods alone. However, this increase in surface area was the consequence of the formation of external area in the crystals and eventual formation of an amorphous phase as evidenced by XRD, not by the emergence of microporosity. This study also demonstrates that UV-light (i.e., ozone) treatments at room temperature were not favorable for the template removal process to produce nanoporous sorbents. Although ozone is more active at lower temperatures, and the treatment was less destructive (i.e., XRD results) than calcination of the template in an oxidative atmosphere, porosimetry tests as well as FT-IR spectroscopy determined that the detemplation of Mg-SBE materials was not accomplished. At least not complete.

4.5 Acknowledgments

This work received support from the National Science Foundation (NSF) Awards CBET-0546370 and CBET-0619349. We thank Dr. Samuel Hernández and co-workers for kindly facilitate access to FT-IR spectroscopy analyses at the Chemistry Department of the UPR-Mayagüez.

LITERATURE CITED

[1] Belen-Cordero, D. S.; Mendez-Gonzalez, S.; Hernandez-Maldonado, A. J. SBE Type Cobalt Aluminophosphate Nanoporous Materials: Degradation of the Structure-Directing Agent. *Micropor. Mesopor. Mater.* **2008**, *109*(1-3), 287-297.

[2] Langmuir, I. The Adsorption of Gases on Plane Surfaces of Glass, Mica and Platinum. *J. Am. Chem. Soc.* **1918**, *40*, 1361-1403.

[3] Choudhary, V. R.; Akolekar, D. B.; Singh, A. P.; Sansare, S. D. lnfluence of Thermal, Hydrothermal, and Acid-Base Treatments on Structural Stability and Surface and Catalytic Properties of $AlPO_4$-5. *J. Catal.* **1988**, *111*, 254-263.

[4] Clark, T.; Ruiz, J. D.; Fan, H.; Brinker, C. J.; Swanson, B. I.; Parikh, A. N. A New Application of UV-Ozone Treatment in the Preparation of Substrate-Supported Mesoporous Thin Films. *Chem. Mater.* **2000**, *12*, 3879-3884.

[5] Parikh, A. N.; Navrotsky, A.; Li, Q.; Yee, C. K.; Amweg, M. L.; Corma, A. Non-Thermal Calcination by Ultraviolet Irradiation in the Synthesis of Microporous Materials. *Micropor. Mesopor. Mater.* **2004**, *76*, 17-22.

[6] Meretei, E.; Halász, J.; Méhn, D.; Kónya, Z.; Korányi, T. I.; Nagy, J. B.; Kiricsi, I. Structural Consequences of Mild Oxidative Template Removal in the Synthesis of Modified MCM-41 Silicates. *J. Mol. Struct.* **2003**, *651-653*, 323-330.

[7] Li, Q.; Amweg, M. L.; Yee, C. K.; Navrotsky, A.; Parikh, A. N. Photochemical Template Removal and Spatial Patterning of Zeolite MFI Thin Films Using UV/Ozone Treatment. *Micropor. Mesopor. Mater.* **2005**, *87*, 45-51.

[8] Navrotsky, A.; Parikh, A. N. Methods for Removing Organic Compounds from Nano-Composite Materials. US6,960,327 B2, November 1,2005, 2005.

[9] Xiao, L.; Li, J.; Jin, H.; Xu, R. Removal of Organic Templates from Mesoporous SBA-15 at Room Temperature Using UV/Dilute H_2O_2. *Micropor. Mesopor. Mater.* **2006**, *96*, 413-418.

CHAPTER 5

TEMPLATED GROWTH OF NANOSTRUCTURES

5.1 Introduction

Carbon nanotubes (CNTs) are unique nanostructures with diverse physical and chemical properties that make them promising candidates for applications in nanotechnology, electronics and optics, among others.[1-5] Some methods used for the synthesis of CNTs include laser ablation, arc discharge, and chemical vapor deposition (CVD).[6-8] The smallest CNTs (i.e., 4 Å) reported were fabricated by Qin et al. in 2000 using the arc discharge technique and confined inside multiwalled carbon nanotubes.[9] A recently developed technique uses molecular sieves (e.g., AlPOs, MeAPOs and M41S) for their templated gowth.[10-43] Depending on nanotube diameter and chiral angle, single-walled carbon nanotube (SWNT) possess also exceptional metallic or semiconductor properties. For a broad range of applications it is requires to use aligned SWNT with uniform properties. High yield and selectivity is also desired. These limitations could be overcome by growing the SWNT within a channel system of uniform pore size like zeolites (i.e., templated growth). Wang and Tang claimed that the smallest single-walled carbon nanotube could be synthesized by the pyrolysis of tetrapropylamine (TPA) in the channels of $AlPO_4$-5.[10, 11]

This study reports the results of our first attempt to achieve templated growth of carbon nanotubes using SBE-type structures as the template. Due to the chemical composition and

the incorporation of transition-metal ions, SBE frameworks (i.e., Co and Mn) can serve as host to confine carbon nanotubes using the uniform pore system of the porous materials. The nanostructured materials were characterized by Raman spectroscopy and Scanning Electron Microscopy (SEM).

5.2 Experimental Section

5.2.1 Preliminary Attempts for the Synthesis of CNTs using the SBE-Type Frameworks

Attempted carbon nanotubes synthesis by pyrolysis (i.e., decomposition) of the organic template within the channels of SBE framework was performed by following the analogue method used by Zhai et al. for the carbonization mechanism of TPA inside the pores of $AlPO_4$-5 and CoAPO-5.[31-35, 40] Synthesis of CNTs within the as-synthesized samples of Co- and Mn-SBE was performed using a Micromeritics ASAP 2020 sample activation module. Samples were degassed *in situ* in a two-stage process. In the first step (i.e., at 373 K) the evacuation stage was run at a heating rate of 3 K/min using a vacuum rate of 10 mm Hg/s and the temperature was kept for 3 h. Similar heating rates were employed for the formal heating stage with final soaking temperatures that ranged from 623 K to 723 K and sustained for 3 h. SBE samples were dissolved in 37 wt-% hydrochloric acid (HCl). The mixture separated into two phases (i.e., one transparent and the other one a black layer). Transparent layer comprised the dissolved SBE framework. Then, the black layer was dispersed into dichloromethane (DCM) and dried.

5.2.2 Raman Spectroscopy

Raman Spectroscopy of SBE matrix was performed using a Renishaw Ramascope Spectrometer (UPR-Mayagüez, Chemistry Department) with global imaging of an area for a selected wavelength configuration operating at an excitation wavelength of 785 nm (red). The beam of a laser was focused upon the sample surface and the resultant Raman scattering was collected and measured with the spectrometer.

5.2.3 Scanning Electron Microscopy

Samples were characterized by scanning electron microscopy (SEM) for determination of phase morphology. SEM images were obtained using a JEOL JSM-6390 instrument. The morphologies of SBE samples were captured using a SEI detector and an accelerating voltage of 10.0 *k*V. Samples were sputter-coated with gold using a Denton Vacuum Desk IV (Denton Vacuum, LLC) unit to improve secondary electron emission and prevent charging.

5.3 Results and Discussion

5.3.1 Raman Spectroscopy

The process for the production of CNTs was carefully analyzed by Raman spectroscopy. Figure 5.1 shows the Raman spectra of Co- and Mn-SBE samples were exposed to an excitation wavelength of 785 nm to determine the presence of nanostructures within the zeolite framework. Organic molecules such as 1,9-diaminononane, which is the structure-directing agent show Raman bands in the 2600-3100 cm^{-1}, ca. 1400 cm^{-1} and 950-1200 cm^{-1}

regions attributed to CH_2 symmetric and anti-symmetric stretching, anti-symmetric deformation bands and C-N stretching modes, respectively. As the organic template starts to decompose such bands should decrease and eventually disappear. *G*-band (i.e., ~1600 cm^{-1}), radial breathing modes (RBM, i.e., 510 and 550 cm^{-1}) and *D* lines are typical features of Raman active modes for the formation of the CNTs.[24, 40, 44] Our Raman spectra for Co- and Mn-SBE samples show two weak bands in the 1100 to 1650 cm^{-1} region, commonly associated to *D*-line and *G*-line, respectively. However, RBM bands in the low frequency region were not observed.

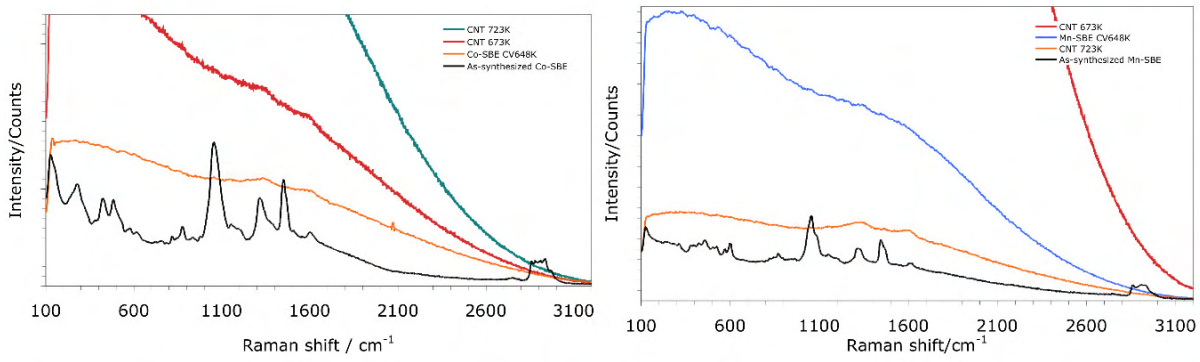

Figure 5.1. Raman spectra of Co- and Mn-SBE samples for attempted templated growth of nanostructures.

5.3.2 Scanning Electron Microscopy

Figures 5.2 and 5.3 illustrate the SEM image of the black layer formed after the Mn- and Co-SBE samples were dissolved in 37-wt% HCl and dichloromethane. SEM images show the formation of bundles of wires of ca. 20 nm (200 Å), quite large if compared to the SWNT synthesized by Tang et al.[10, 11] In addition, no orientation of the structures formed can be

observed (i.e., multi-dimensional growth). The results presented here confirm the viability of using SBE framework, as a direct approach to the templated growth of carbon nanotubes but it is still a challenge to control and assemble the formation of small CNTs.

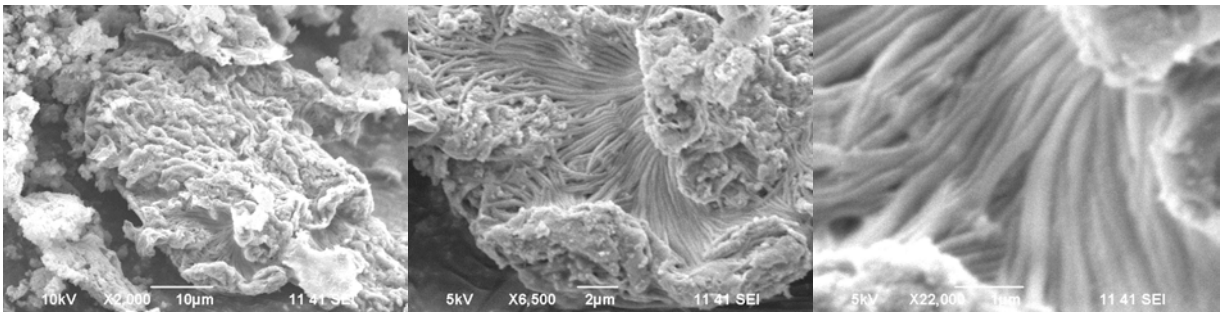

Figure 49. SEM image of the black layer formed after Mn-SBE samples were dissolved in 37-wt% HCl and dichloromethane.

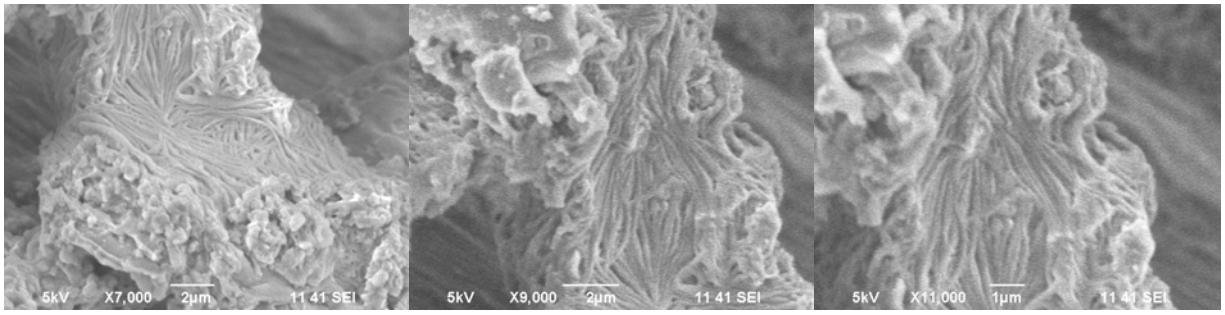

Figure 50. SEM image of black layer formed after Co-SBE samples were dissolved in 37-wt% HCl and dichloromethane.

5.4 Preliminary Conclusions

Bands associated to CNTs growth were observed in Raman spectra. It is important to mention that these analyses were performed to the matrix containing the SBE frameworks and perhaps that is the reason for the lower intensity of the bands. The isolation of the black layer formed after the dissolution of the SBE samples displayed SEM images that showed the

growth of agglomerated nanostructures larger in size as compared to the 4 Å SWNT reported in literature.[10, 11] The data supports the hypothesis for the formation of the nanotubes but other analyses, such as Transmission Electron Microscopy (TEM), FT-IR and X-Ray Photoelectron spectroscopy (XPS) are necessary in order to characterize and determine the formation of CNTs. Evolved gas analysis (i.e., EGA) may give a better insight of the carbonization mechanism by identification of the volatile species. However, the process itself appears to be very dependent on the exact experimental conditions.

5.5 Acknowledgements

This work received support from the National Science Foundation (NSF) Awards CBET-0546370 and CBET-0619349. We thank Dr. Carlos Velázquez (UPR-Mayagüez, Chemical Engineering), Dr. Samuel Hernández and co-workers (UPR-Mayagüez, Chemistry) for providing access to SEM and Raman spectroscopy analyses, respectively.

LITERATURE CITED

[1] Dalton, A. B.; Collins, S.; Munoz, E.; Razal, J. M.; Ebron, V. H.; Ferraris, J. P.; Coleman, J. N.; Kim, B. G.; Baughman, R. H. Super-Tough Carbon-Nanotube Fibres - These Extraordinary Composite Fibres Can Be Woven into Electronic Textiles. *Nature* **2003**, *423*(6941), 703-703.

[2] Collins, P. C.; Arnold, M. S.; Avouris, P. Engineering Carbon Nanotubes and Nanotube Circuits Using Electrical Breakdown. *Science* **2001**, *292*(5517), 706-709.

[3] Zandonella, C. Is It All Just a Pipe Dream? *Nature* **2001**, *410*(6830), 734-735.

[4] De Heer, W. A.; Chatelain, A.; Ugarte, D. A Carbon Nanotube Field-Emission Electron Source. *Science* **1995**, *270*(5239), 1179-1180.

[5] Baughman, R. H.; Cui, C. X.; Zakhidov, A. A.; Iqbal, Z.; Barisci, J. N.; Spinks, G. M.; Wallace, G. G.; Mazzoldi, A.; De Rossi, D.; Rinzler, A. G.; Jaschinski, O.; Roth, S.; Kertesz, M. Carbon Nanotube Actuators. *Science* **1999**, *284*(5418), 1340-1344.

[6] Iijima, S. Helical Microtubules of Graphitic Carbon. *Nature* **1991**, *354*(6348), 56-58.

[7] Journet, C.; Maser, W. K.; Bernier, P.; Loiseau, A.; delaChapelle, M. L.; Lefrant, S.; Deniard, P.; Lee, R.; Fischer, J. E. Large-Scale Production of Single-Walled Carbon Nanotubes by the Electric-Arc Technique. *Nature* **1997**, *388*(6644), 756-758.

[8] Thess, A.; Lee, R.; Nikolaev, P.; Dai, H. J.; Petit, P.; Robert, J.; Xu, C. H.; Lee, Y. H.; Kim, S. G.; Rinzler, A. G.; Colbert, D. T.; Scuseria, G. E.; Tomanek, D.; Fischer, J. E.; Smalley, R. E. Crystalline Ropes of Metallic Carbon Nanotubes. *Science* **1996**, *273*(5274), 483-487.

[9] Qin, L.; Zhao, X.; Hirahara, K.; Miyamoto, Y.; Ando, Y.; Iijima, S. The Smallest Carbon Nanotube. *Nature* **2000**, *408*, 50.

[10] Tang, Z. K.; Sun, H. D.; Wang, J.; Chen, J.; Li, G. Mono-sized single-wall carbon nanotubes formed in channels of AlPO4-5 single crystal. *Appl. Phys. Lett.* **1998**, *73*(16), 2287-2289.

[11] Wang, N.; Tang, Z. K.; Li, G. D.; Chen, J. S. Single-Walled 4 Å Carbon Nanotube Arrays. *Nature* **2000**, *408*, 50-51.

[12] Sun, H. D.; Tang, Z. K.; Wang, J. N. Conductance of mono-sized carbon nanotubes in channels of zeolite crystal. *J. Magn. Magn. Mater.* **1999**, *199*, 255-257.

[13] Sun, H. D.; Tang, Z. K.; Chen, J.; Li, G. Polarized Raman spectra of single-wall carbon nanotubes mono-dispersed in channels of AlPO4-5 single crystals. *Solid State Commun.* **1999**, *109*(6), 365-369.

[14] Sun, H. D.; Tang, Z. K.; Chen, J.; Li, G. Synthesis and Raman characterization of mono-sized single-wall carbon nanotubes in one-dimensional channels of AlPO4-5 crystals. *Appl. Phys. A-Mater.* **1999**, *69*(4), 381-384.

[15] Tang, Z. K.; Sun, H. D.; Wang, J. Electrical transport properties of mono-dispersed single-wall carbon nanotubes formed in channels of zeolite crystal. *Physica B* **2000**, *279*(1-3), 200-203.

[16] Launois, P.; Moret, R.; Le Bolloc'h, D.; Albouy, P. A.; Tang, Z. K.; Li, G.; Chen, J. Carbon nanotubes synthesised in channels of AlPO4-5 single crystals: first X-ray scattering investigations. *Solid State Commun.* **2000**, *116*(2), 99-103.

[17] Li, Z. M.; Tang, Z. K.; Liu, H. J.; Wang, N.; Chan, C. T.; Saito, R.; Okada, S.; Li, G. D.; Chen, J. S.; Nagasawa, N.; Tsuda, S. Polarized absorption spectra of single-walled 4 angstrom carbon nanotubes aligned in channels of an AlPO4-5 single crystal. *Phys. Rev. Lett.* **2001**, *8712*(12).

[18] Nagasawa, N.; Sugiyama, H.; Naka, N.; Kudryashov, I.; Watanabe, M.; Hayashi, T.; Bozovic, I.; Bozovic, N.; Li, G.; Li, Z.; Tang, Z. K. Visible emission of single-wall carbon nanotubes formed in micro-channels of zeolite crystals. *J. Lumin.* **2002**, *97*(3-4), 161-167.

[19] Li, G. D.; Tang, Z. K.; Wang, N.; Chen, J. S. Structural study of the 0.4-nm single-walled carbon nanotubes aligned in channels of AlPO4-5 crystal. *Carbon* **2002**, *40*(6), 917-921.

[20] Tang, Z. K.; Zhang, L. Y.; Wang, N.; Zhang, X. X.; Wang, J. N.; Li, G. D.; Li, Z. M.; Wen, G. H.; Chan, C. T.; Sheng, P. Ultra-small single-walled carbon nanotubes and their superconductivity properties. *Synthetic Met.* **2003**, *133*, 689-693.

[21] Tang, Z. K.; Wang, N.; Zhang, X. X.; Wang, J. N.; Chan, C. T.; Sheng, P. Novel properties of 0.4 nm single-walled carbon nanotubes templated in the channels of AlPO4-5 single crystals. *New J. Phys.* **2003**, *5*.

[22] Tang, Z. K.; Li, Z. M.; Li, I. L.; Zhang, X. X.; Wang, N.; Wang, H. N.; Sheng, P. Electrical and optical properties of ultra-small carbon nanotubes arrayed in channels of zeolite single crystals. *Mater. Trans.* **2003**, *44*(10), 2066-2069.

[23] Hulman, M.; Kuzmany, H.; Dubay, O.; Kresse, G.; Li, L.; Tang, Z. K. Raman spectroscopy of template grown single wall carbon nanotubes in zeolite crystals. *J. Chem. Phys.* **2003**, *119*(6), 3384-3390.

[24] Li, Z. M.; Zhai, J. P.; Liu, H. J.; Li, I. L.; Chan, C. T.; Sheng, P.; Tang, Z. K. Synthesis of 4 angstrom single-walled carbon nanotubes in catalytic Si-substituted AlPO4-5 molecular sieves. *Appl. Phys. Lett.* **2004**, *85*(7), 1253-1255.

[25] Li, Z. M.; Liu, H. J.; Ye, J. T.; Chan, C. T.; Tang, Z. K. Optical properties of 0.4-nm single-wall carbon nanotubes aligned in channels of AlPO4-5 single crystals. *Appl. Phys. A-Mater.* **2004**, *78*(8), 1121-1128.

[26] Li, I. L.; Tang, Z. K. Curvature effect in ultra-small single-walled carbon nanotubes. *Appl. Surf. Sci.* **2004**, *226*(1-3), 72-77.

[27] Li, I. L.; Launois, P.; Tang, Z. K. Synthesis and characterization of Se nano-structures inside porous zeolite crystals. *Appl. Surf. Sci.* **2004**, *226*(1-3), 36-40.

[28] Hulman, M.; Kuzmany, H.; Dubay, O.; Kresse, G.; Li, L.; Tang, Z. K.; Knoll, P.; Kaindl, R. Raman spectroscopy of single wall carbon nanotubes grown in zeolite crystals. *Carbon* **2004**, *42*(5-6), 1071-1075.

[29] Ye, J. T.; Tang, Z. K. Raman spectra and thermal stability analysis of 0.4 nm freestanding single-walled carbon nanotubes. *Phys. Rev. B* **2005**, *72*(4).

[30] Mei, Y. F.; Siu, G. G.; Fu, R. K. Y.; Chu, P. K.; Li, Z. M.; Zhai, J. P.; Liu, H. J.; Tang, Z. K.; Lai, C. W.; Ong, H. C. Visible cathodoluminescence of 4 A angstrom single-walled carbon nanotubes. *Appl. Phys. Lett.* **2005**, *87*(21).

[31] Zhai, J. P.; Tang, Z. K.; Li, Z. M.; Li, I. L.; Jiang, F. Y.; Sheng, P.; Hu, X. J. Carbonization mechanism of tetrapropylammonium-hydroxide in channels of AlPO4-5 single crystals. *Chem. Mater.* **2006**, *18*(6), 1505-1511.

[32] Zhai, J. P.; Tang, Z. K.; Lam, F. L. Y.; Hu, X. J. Thermal decomposition of carbon precursors in decorated AFI zeolite crystals. *J. Phys. Chem. B* **2006**, *110*(39), 19285-19290.

[33] Zhai, J. P.; Tang, Z. K.; Hu, X. J.; Zhang, X. X.; Sheng, P. Catalytic growth of 0.4 nm single-walled carbon nanotubes aligned inside porous zeolite crystals. *Phys. Status Solidi B* **2006**, *243*(13), 3082-3086.

[34] Zhai, J. P.; Li, Z. M.; Liu, H. J.; Li, I. L.; Sheng, P.; Hu, X. J.; Tang, Z. K. Catalytic effect of metal cations on the formation of carbon nanotubes inside the channels of AlPO4-5 crystal. *Carbon* **2006**, *44*(7), 1151-1157.

[35] Zhai, J. P.; Li, Z. M.; Li, I. L.; Liu, H. J.; Sheng, P.; Tang, Z. K. Catalyst effect of metal cations on pyrolysis of hydrocarbon molecules and formation of carbon nanotubes in the channels of AIPO(4)-5 crystals. *J. Porous Mat.* **2006**, *13*(3-4), 291-295.

[36] Ye, J. T.; Tang, Z. K.; Siu, G. G. Optical characterizations of iodine molecular wires formed inside the one-dimensional channels of an AlPO4-5 single crystal. *Appl. Phys. Lett.* **2006**, *88*(7).

[37] Jiang, F. Y.; Tang, Z. K.; Zhai, J. P.; Ye, J. T.; Han, J. R. Synthesis of AlPO4-5 crystals using TBAOH as template. *Micropor. Mesopor. Mater.* **2006**, *92*(1-3), 129-133.

[38] Tang, K.; Wang, Y. G.; Song, L. J.; Duan, L. H.; Zhang, X. T.; Sun, Z. L. Carbon Nanotube Templated Growth of Nano-crystalline ZSM-5 and NaY Zeolites. *Mater. Lett.* **2006**, *60*(17-18), 2158- 2160.

[39] Ye, J. T.; Zhai, J. P.; Tang, Z. K. Raman characterization of 0.4 nm single-walled carbon nanotubes formed in the channels of ALPO(4)-5 zeolite single crystals. *J. Phys.-Condens. Mat.* **2007**, *19*(44).

[40] Zhai, J. P.; Li, I. L.; Li, Z. M.; Ye, J. T.; Tang, Z. K., Formation Mechanism of 0.4,nm Single-Walled Carbon Nanotubes in CoAPO-5 Single Crystals. In *Nanoscale Phenomena*, Springer: New York, USA, 2008; Vol. 2, pp 49-59.

[41] Dai, L.; Patil, A.; Gong, X.; Guo, Z.; Liu, L.; Liu, Y.; Zhu, D. Aligned Nanotubes. *Chem. Phys. Chem.* **2004**, *4*, 1150-1169.

[42] Lim, S.; Ciuparu, D.; Pak, C.; Dobek, F.; Chen, Y.; Harding, D.; Pfefferle, L.; Haller, G. Synthesis and Characterization of Highly Ordered Co-MCM-41 for Production of Aligned Single Walled Carbon Nanotubes (SWNT). *J. Phys. Chem. B* **2003**, *107*, 11048-11056.

[43] Wu, C. G.; Bein, T. Conducting Carbon Wires in Ordered, Nanometer-Sized Channels. *Science* **1994**, *266*, 1013-1015.

[44] Belin, T.; Epron, F. Characterization Methods of Carbon Nanotubes: A Review. *Mater. Sci. Eng. B-Solid* **2005**, *119*(2), 105-118.

CHAPTER 6

CONCLUDING REMARKS

The aim of this dissertation was to contribute to the further development of SBE nanoporous sorbents by the removal of the structure-directing agent. An approach, using non-traditional methods was used for the detemplation process as the conventional calcination method resulted in "*non-porous*" frameworks. Powder forms of Co-, Mg- and Mn-SBE materials were successfully prepared, all containing metal-to-aluminium ratios close to unity (Me/Al = 1.0). Mg- and Mn-SBE materials displayed square-plate morphology with truncated corners grown in aggregate fashion. This differs from Co-SBE materials, which displayed hexagonal-plate single particles. Based on this morphology information, it seems plausible that the metal sources employed during synthesis played a role in defining the ultimate materials morphology. TGA measurements and a Redhead's type analysis corroborated that 1,9-diaminononane SDA is not just a space-filler (non-dissociated ion pair). The template experiences a strong interaction with the host framework and this, together with the metal tetrahedra metastability, introduces a high degree of complexity when trying the SDA removal. In terms of detemplation methods, calcination in an oxidative atmosphere greatly influences the structural stability of the SBE-type materials. Air detemplation was detrimental to the framework as evidenced by TGA, *in situ* high temperature XRD, *in situ* XRD-DSC, UV-*vis*, XPS, EPR and MAS-NMR analyses. Meanwhile, vacuum detemplation using carefully controlled evacuating rates and a temperature of 648 K resulted in SBE materials with surface areas that correlated to microporous structures. The observed surface

areas increased as follows: Mn-SBE < Co-SBE < Mg-SBE. Although the best detemplation strategy so far consists of employing vacuum or helium atmospheres, the SBE variants still experienced coordination chemistry changes during the course of treatment. Table 6.1 summarizes some of the materials features observed during both inert and oxidative detemplation processes.

Table 6.1. Summary of SBE-type materials characteristics upon detemplation process.

Technique	**Co-SBE**	**Mg-SBE**	**Mn-SBE**
FT-IR	Confirmed the removal of the SDA.		Increase in the intensity of C-H and N-H stretching.
***In situ* High Temperature XRD**	Tolerate well detemplation treatment in vacuum or helium.		Crystallographic planes associated 12-ring channels became considerably displaced during treatment in helium, resulting in a structural distortion and possible encapsulation of the SDA.
XRD-DSC	Two endothermic peaks: First endotherm - desorption of water. Second - start of the decomposition of the template.		Oxidative: Exo/Endo Mn-SBE sample in air showed the lowest onset temperature.
UV-*vis*	Co in a tetrahedral environment: • Prominent bands at 598 and 629 nm in UV-*vis* assigned to the Co(II) *d-d* transition band. • EPR *g*-tensors of Co^{2+} ions after substitution in tetrahedral positions.	UV-*vis* (Not available) Exhibited various coordination states. • Non-paramagnetic Mg-SBE samples still presented EPR signals, possibly attributed to the formation of paramagnetic defect sites generated during the heat treatment. • ^{27}Al MAS-NMR spectra revealed the reversible formation of aluminium octahedral sites upon water adsorption.	Exhibited various coordination states. Mn atoms form extra-framework species during detemplation, even in vacuum. This was observed by UV-*vis*, XPS, EPR and MAS-NMR spectroscopic methods.
XPS			
EPR			
MAS-NMR			

Further effort is still required to completely understand the coordination nature in the SBE samples prior and during detemplation, but the present study clearly demonstrates that successful SDA removal in highly metal-substituted AlPOs with multi-dimensional channels is possible. Unlike, the inability to successfully remove the template from SBE using alternate methods such as solvent extraction and/or ion exchange, among others does not imply the template cannot be removed. However, it does indicate that the template interacts with the framework in a unique physical or chemical configuration that precludes the use of conventional template removal methods (i.e., calcination).

APPENDICES FOR DISSERTATION

SYNTHESIS, CHARACTERIZATION AND DETEMPLATION OF THERMALLY UNSTABLE METAL-SUBSTITUTED ALUMINOPHOSPHATES

Daphne S. Belén-Cordero
Department of Chemical Engineering
University of Puerto Rico
Mayagüez, PR 00680, USA.

Contents

^{13}C MAS NMR for as-synthesized and treated Mg-SBE samples

The spectrum of ^{13}C for as-synthesized Mg-SBE exhibited peaks with chemical shifts showed in Table 3.2. The chemical shift of ^{13}C NMR of 1,9-diaminononane (Figure A.1) was estimated using ChemDraw®. Five different carbon peaks were resolved with the same intensity except the center carbon of the alkyl chain that displayed half of the intensity. The ^{13}C NMR spectrum of Mg-SBE (Figure A.2) appears to be deviated from the expectation, especially the signal intensity around 27 ppm, which is unusually large. Assuming that the 50 ppm peak counts as one carbon, the intensity ratio reveals the relative carbon content as 1:2:7:1:1 for 50, 41, 27, 20, and 11 ppm peaks, respectively, summing up to 12 carbons. It is possible for ^{13}C NMR to show solvent peaks, and/or fragmented organic molecules. The peaks at 50, 20, and 11 ppm in ^{13}C NMR for as-synthesized Mg-SBE might be from DPA, the co-solvent, and the peaks at 41 and at around 27 ppm might be from the SDA. If the broad peak at 27 ppm is considered as one overlapped peak of the four types of carbons in SDA and the peak at 41 ppm as one from the carbon directly bonded to nitrogen, then the measured integral ratio of 2:7 between two peaks is consistent to the predicted spectrum. The measured integral ratio (1:1:1) of the peaks at 50, 20, and 11 ppm is also consistent to the predicted spectrum of DPA estimated using ChemDraw®. From the integral values of all the peaks the amount of unreacted DPA in as-synthesized Mg-SBE sample results in half of the amount of SDA. However, we could not detect any carbon NMR peak from the treated samples. However, ^{1}H spectra showed that there were still organic molecules within the framework. The absence of ^{13}C peak can be explained as two possible situations: the

remained organic molecules might be ammonium radicals or free radicals in the organic molecule might suppress the ^{13}C NMR signal.

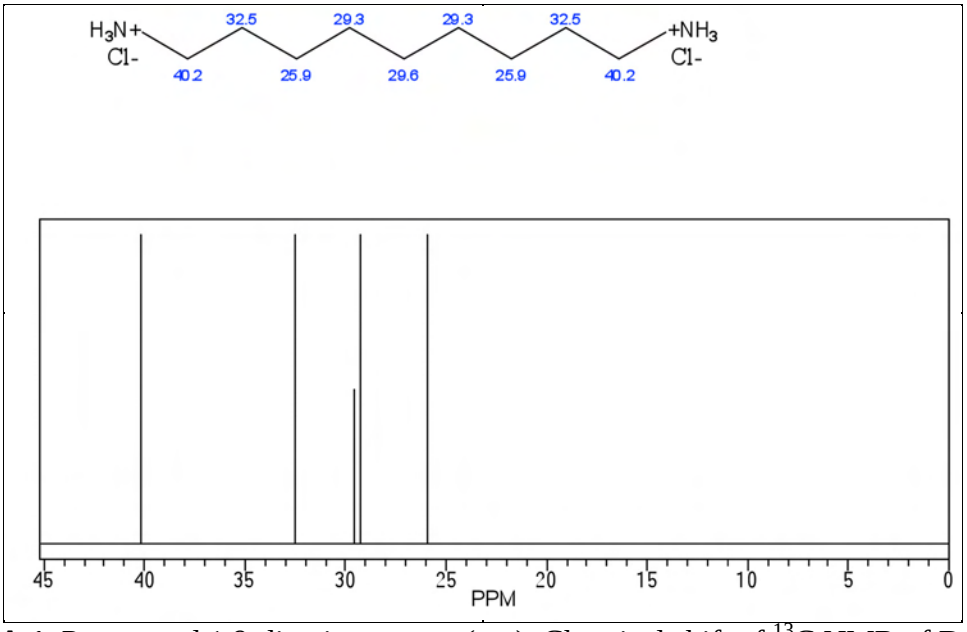

Figure A.1. Protonated 1,9-diaminononane (top). Chemical shift of ^{13}C NMR of DAN was estimated using ChemDraw® (bottom).

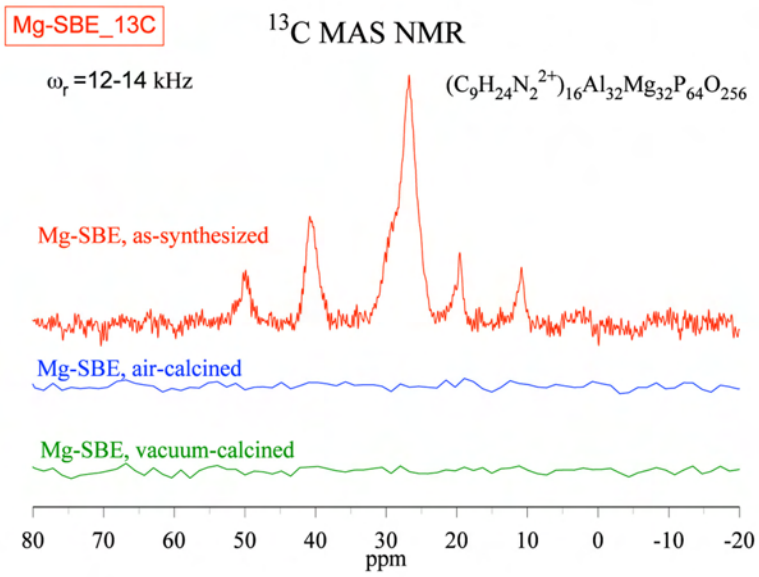

Figure A.2. ^{13}C NMR spectra for Mg-SBE samples.

^{31}P MAS NMR for as-synthesized Mg-SBE

Shifts in the ^{31}P signal are associated to structural differences due to its susceptibility to the chemical environment. A SBE-type framework consists of 4 different T sites,[1] but there are no appropriate references in the literature to help to elucidate the exact ^{31}P NMR information. Therefore, ignoring the detail site resolution, and resembling Barrie and Klinowski,[2] the observed ^{31}P NMR shifts of as-synthesized Mg-SBE sample could be assigned to P(nAl, (4-n)Mg) sites as -26, -20, -15, -10, and -3 ppm to P(4Al), P(3Al, Mg), P(2Al, 2Mg), P(Al, 3Mg), and P(4Mg), respectively. Following this analogy, signal intensities of phosphorous sites were obtained by deconvolution of the ^{31}P NMR spectrum. Assignments of the chemical shifts and the distribution percentages of each site using this approach to analyze the ^{31}P spectra are summarized in Table 4. The P(nAl, (4-n)Mg) site distribution is not in agreement with the random model which gives 6.25%, 25%, 37.5%, 25%, 6.25% for P(4Al), P(3Al, Mg), P(2Al, 2Mg), P(Al, 3Mg), and P(4Mg), respectively, when calculated using the Mg/Al ratio of 1 as predicted from the synthesis gel formulation. This may indicate the presence of ordering behavior when Mg substituted Al. The ^{31}P resolution seen for the as-synthesized Mg-SBE disappears to render only broad peak after calcinations either in air or in the vacuum. The P(0Al, 4Mg) site at -2.9 ppm appears to be resolved when calcination in air occurred.

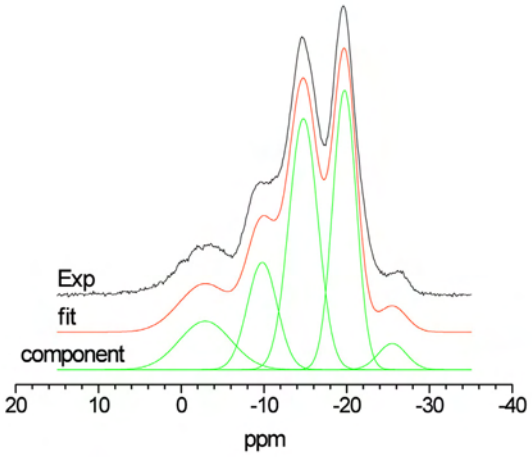

Figure A.3. Deconvolution of the ^{31}P NMR spectrum.

Table A1. ^{31}P NMR peaks of Mg-SBE.

Phosphorus sites	Chemical shift	Intensity	Wt %
P(0Al, 4Mg)	-2.9	25286.9	12.4
P(1Al, 3Mg)	-9.8	32059.5	15.7
P(2Al, 2Mg)	-14.8	73037.6	35.8
P(3Al, Mg)	-19.7	66274.1	32.5
P(4Al, 0Mg)	-25.5	7384.3	3.6

LITERATURE CITED

[1] Baerlocher, C.; McCusker, L. B., Database of Zeolite Structures. In International Zeolite Association Synthesis Commission: 2007.

[2] Barrie, P. J.; Klinowski, J. Ordering in the Framework of a Magnesium Aluminophosphate Molecular-Sieve. *J. Phys. Chem.* **1989**, *93*(16), 5972-5974.